CASL-U-2015-0319-000

Power uprates
and plant life extension

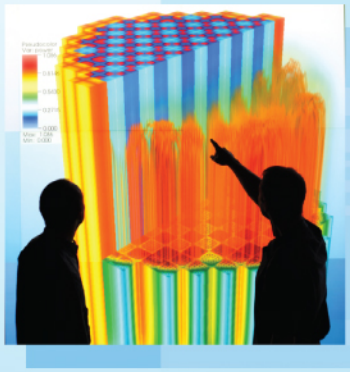

Engineering design
and analysis

Science-enabling
high performance
computing

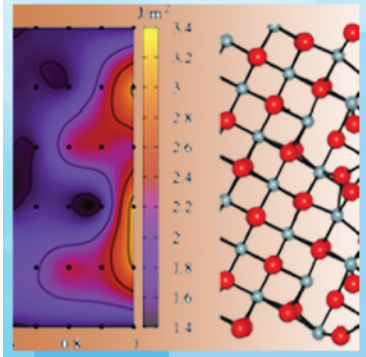

Fundamental science

Plant operational data

Consortium for Advanced Simulation of LWRs

Synthesis of CRUD and its Effects on Pool and Subcooled Flow Boiling L2.THM.P11.02

Carolyn Coyle
Bren Phillips
Sean Lowder
Jacopo Buongiorno
Thomas McKrell
Massachusetts Institute of Technology

U.S. DEPARTMENT OF ENERGY | Nuclear Energy

CASL-U-2015-0319-000

Revision Log

Revision	*Date*	*Affected Pages*	*Revision Description*
0	9/30/2015	All	Initial Issuance

Document pages that are:
Export Controlled: _____
IP/Proprietary/NDA Controlled: _____
Sensitive Controlled: _____

Requested Distribution:
To:
CASL Senior Leader Team (SLT)
Extended Leadership Team (ELT)

Copy:

CASL-U-2015-0319-000

Executive Summary

This milestone is dedicated to studying the effects of synthetic CRUD (Chalk River Unidentified Deposits) on pool and subcooled flow boiling boiling parameters. Previous pool boiling studies have demonstrated the potential of porous, hydrophilic surfaces to lead to more efficient boiling. CRUD is a naturally occurring porous, hydrophilic layer that forms on fuel rods during reactor operation. As such, CRUD deposition may have large effects on critical heat flux (CHF) and heat transfer coefficient (HTC). An investigation of such effects is being conducted as part of this CASL project by preparing synthetic CRUD on indium tin oxide-sapphire heaters. The data generated here may inform advanced models of boiling heat transfer in VERA-THM and/or validate existing models.
Specifically, the milestone work has focused on:

1. Creating well-defined and characterized, synthetic CRUD with parameters representative of reactor CRUD on MIT test heaters.

2. Experimentally studying the effects of synthetic CRUD on boiling heat transfer, especially heat transfer coefficient (HTC), critical heat flux (CHF), bubble nucleation density, bubble departure frequency, and bubble departure diameter in pool and subcooled flow boiling.

These heaters are being tested in pool and flow boiling facilities in MIT's Reactor Hydraulics Laboratory. Synthetic CRUD was created using layer-by-layer deposition of 100 nm silica nanoparticles to form porous, hydrophilic thick films. Photolithography was used to manufacture posts that were then dissolved to create characteristic boiling chimneys. Features such as CRUD thickness, wettability, pore size, and chimney diameter and pitch were verified to be representative of reactor CRUD. Silica nanoparticles were used as a surrogate for reactor CRUD nanoparticle materials (iron and nickel oxides) since they create more stable films. To ensure accurate modeling, independent of material, 10 nm silica nanoparticle and 10 nm iron oxide nanoparticle boiling tests were conducted and found to be similiar. During testing, IR thermography and high-speed video (HSV) are used to obtain two dimensional temperature profiles of the active heater area to quantify properties such as HTC, nucleation site density, bubble departure frequency, and bubble departure diameter. The bubble parameters follow expected trends with mass flux and heat flux. From the data obtained to date, the IR/HSV flow data (Chapter 6) has shown that HTC increases with increasing thickness and increasing chimney diameter. However the HTC is relatively

unaffected by the presence of the base case chimneys and the chimney pitch. These trends are supported by the combination of basic bubble parameters according to the heat flux partitioning model. The statistical significance of these trends varies with mass flux.

Contents

1 Milestone Description **17**
1.1 Motivation . . . 17
1.2 Objectives . . . 18

2 Relevant Theory **19**
2.1 Boiling Heat Transfer . . . 19
2.1.1 Boiling Fundamentals . . . 19
2.1.2 Pool Boiling . . . 23
2.1.3 Subcooled Flow Boiling . . . 24
2.1.4 Boiling Heat Transfer Models . . . 25
2.2 Surface Characteristics . . . 28
2.2.1 Wettability . . . 28
2.2.2 Roughness . . . 29
2.2.3 Porosity . . . 30
2.3 Surface Engineering . . . 30
2.4 CRUD . . . 32
2.4.1 Morphology . . . 32
2.4.2 Heat Transfer Mechanisms . . . 33
2.4.3 Models . . . 34

3 Test Matrix **39**
3.1 Synthetic CRUD Test Matrix . . . 39
3.2 Flow Boiling Test Matrix . . . 40
3.3 Rationale and Limitations . . . 41
3.3.1 Material Selection . . . 41
3.3.2 Thickness . . . 42
3.3.3 Porosity and Pore Size . . . 42

4 Experimental Methods **45**
4.1 ITO-Sapphire Heaters . . . 45
4.1.1 Pool Boiling Design . . . 46
4.1.2 Flow Boiling Design . . . 46
4.2 Synthetic CRUD Fabrication . . . 47
4.2.1 Heater Preparation . . . 47
4.2.2 Photolithography . . . 47

4.2.3 Layer-by-Layer Deposition . . . 50
4.2.4 Post Removal . . . 53
4.2.5 Autoclaving . . . 53
4.3 Feature Verification . . . 54
4.3.1 Stylus Contact Profilometer . . . 55
4.3.2 Contact Angle Measurement . . . 56
4.3.3 Duel Beam Focused Ion Beam/Scanning Electron Microscope (FIB/SEM) . . . 56
4.3.4 Spectroscopic Ellipsometer . . . 57
4.4 Heater Testing and Facilities . . . 57
4.4.1 Heater Preparation . . . 57
4.4.2 Pool Boiling Facility . . . 58
4.4.3 Flow Boiling Loop . . . 60
4.5 Data Reduction . . . 62
4.5.1 Calibration . . . 62
4.5.2 IR Imaging Analysis . . . 63
4.5.3 HSV Imaging Analysis . . . 64
4.5.4 Uncertainty Analysis . . . 64
4.5.5 Repeatability . . . 65

5 Pool and Flow Boiling IR/HSV Results 67
5.1 SEM/FIB Images . . . 67
5.2 Pool Boiling . . . 69
5.2.1 Surface Analysis . . . 69
5.2.2 IR Results . . . 69
5.2.3 Discussion . . . 69
5.3 Flow Boiling Test Matrix . . . 71
5.4 Case 0: Uncoated Heater . . . 71
5.4.1 Surface Analysis . . . 71
5.4.2 IR/HSV Results . . . 71
5.5 Case 1: 2μm Thick, No Chimneys . . . 74
5.5.1 Surface Analysis . . . 74
5.5.2 IR/HSV Results . . . 74
5.6 Case 2: 2μm Thick, 10μm Diameter Chimneys on 25μm Pitch . . . 76
5.6.1 Surface Analysis . . . 76
5.6.2 IR/HSV Results . . . 76
5.7 Case 3: 4μm Thick, 10μm Diameter Chimneys on 25μm Pitch . . . 78
5.7.1 Surface Analysis . . . 78
5.7.2 IR/HSV Results . . . 78
5.8 Case 6: 2μm Thick, 10μm Diameter Chimneys on 45μm Pitch . . . 80
5.8.1 Surface Analysis . . . 80
5.8.2 IR/HSV Results . . . 80
5.9 Case 7: 2μm Thick, 12.5μm Diameter Chimneys on 27.5μm Pitch . . . 82
5.9.1 Surface Analysis . . . 82
5.9.2 IR/HSV Results . . . 82

6 Discussion: Effects of Layer Thickness and Chimney Pitch and Diameter **85**
6.1 Effect of Synthetic CRUD 85
6.2 Effect of Chimneys 88
6.3 Effect of Layer Thickness 90
6.4 Effect of Chimney Pitch 92
6.5 Effect of Chimney Diameter 94
6.6 Future Work 96

7 Conclusions **97**

List of Figures

2-1 Example of a nucleation site before and after bubble growth. Adopted from Phillips [10]. 19
2-2 The contact angle of a (a) hydrophilic (well wetting) (b) hydrophobic (water repellent) surface. 20
2-3 Sugrue et al. force balance model for bubble departure diameter. Adopted from Sugrue [20]. 23
2-4 Characteristic pool boiling curve. 24
2-5 Regions of heat transfer in convective flow boiling with uniform wall heat flux. Adopted from Collier [21]. 25
2-6 Wettability regimes (a) Wenzel (b) Cassie. 29
2-7 R_a: Arithmetic average roughness. Adopted from O'Hanley [7]. . . . 29
2-8 Spherical Packing with (a) low porosity (b) high porosity. 30
2-9 Pore Reynolds number variation with pressure and pore diameter [5]. 31
2-10 (a) CRUD from a PWR fuel assembly. Adopted from EPRI [44]. (b) CRUD Schematic. Courtesy of M. Short, MIT. 33
2-11 Wick boiling diagram showing the locations of interest for capillary wicking, viscous forces, and vapor escape. 34
2-12 Pan and Jones (1985) CRUD model results. Adopted from Pan and Jones (1985) [48]. 36
2-13 Distribution of heat flux from the CRUD. Adopted from Haq et al. [54]. 37

3-1 Thermal resistance vs. layer thickness for different materials. 43

4-1 Pool Boiling ITO-Sapphire Heater. 46
4-2 Flow Boiling ITO-Sapphire Heater. 47
4-3 Glow Research AutoGlow Plasma System. 48
4-4 AZ 4620 Photolithography Process. 49
4-5 Photolithography Manufacturing Equipment. 50
4-6 10μm chimney on 25μm pitch mask pattern. 50
4-7 Layer-by-Layer (LbL) Deposition of Bilayers. 51
4-8 Zeiss HMS Programmable Slide Stainer. 52
4-9 Layer-by-Layer Deposition Process. 53
4-10 Tuttnauer-Brinkmann 2340M Autoclave. 54
4-11 100nm SiO_2 LbL Films Before and After Autoclaving. 54
4-12 Dektak 150 Surface Profilometer. 55

4-13 KSV Instruments CAM 101 Goniometer. 56
4-14 Helios Nanolab 600 Dual Beam Focused Ion Beam Milling System. . . 57
4-15 J.A. Woollam Co., INC model XLS-100 Spectroscopic Ellipsometer [6]. 58
4-16 UVOCS T10X10/OES. 59
4-17 Pool Boiling Facility Schematic. 60
4-18 Flow Boiling Loop Schematic [10]. 61
4-19 Images of flow boiling loop test section components [10]. 62
4-20 Test Section and Camera Setup Schematic [10]. 62
4-21 Wet and Dry Calibration Curves. 63

5-1 10nm Fe_3O_4 coating with chimneys (low and high magnification). . . 67
5-2 100nm SiO_2 coating (low and high magnification). 68
5-3 100nm SiO_2 coating with 10μm chimneys on a 25μm pitch (low and high magnification). 68
5-4 Pool boiling for uncoated [7] and 10nm, 2μm Fe_3O_4 and SiO_2 coatings with 10μm chimneys on a 25μm pitch and without chimneys. Maximum uncertainties are T= 2°C, q" = 2% , and HTC = 11%. 70
5-5 Flow boiling data for uncoated heater at 10° subcooling. 72
5-6 Flow boiling data for uncoated heater at 10° subcooling. 73
5-7 Flow boiling data for 2μm thick, no chimneys heater at 10° subcooling. 74
5-8 Flow boiling data for 2μm thick, no chimneys heater at 10° subcooling. 75
5-9 Flow boiling data for 2μm thick, 10μm diameter chimneys on 25μm pitch heater at 10° subcooling. 76
5-10 Flow boiling data for 2μm thick, 10μm diameter chimneys on 25μm pitch heater at 10° subcooling. 77
5-11 Flow boiling data for 4μm thick, 10μm diameter chimneys on 25μm pitch heater at 10° subcooling. 78
5-12 Flow boiling data for 4μm thick, 10μm diameter chimneys on 25μm pitch heater at 10° subcooling. 79
5-13 Flow boiling data for 2μm thick, 10μm diameter chimneys on 45μm pitch heater at 10° subcooling. 80
5-14 Flow boiling data for 2μm thick, 10μm diameter chimneys on 45μm pitch heater at 10° subcooling. 81
5-15 Flow boiling data for 2μm thick, 12.5μm diameter chimneys on 27.5μm pitch heater at 10° subcooling. 82
5-16 Flow boiling data for 2μm thick, 12.5μm diameter chimneys on 27.5μm pitch heater at 10° subcooling. 83

6-1 Flow boiling data for CRUD presence comparison. 86
6-2 Flow boiling data for CRUD presence comparison. 87
6-3 Flow boiling data for chimney presence comparison. 88
6-4 Flow boiling data for chimney presence comparison. 89
6-5 Flow boiling data for thickness comparison. 90
6-6 Flow boiling data for thickness comparison. 91
6-7 Flow boiling data for chimney pitch comparison. 92

6-8 Flow boiling data for chimney pitch comparison. 93
6-9 Flow boiling data for chimney diameter comparison. 94
6-10 Flow boiling data for chimney diameter comparison. 95

List of Tables

3.1 Reactor CRUD vs. synthetic CRUD morphology comparison [5]. . . . 39
3.2 Synthetic CRUD test matrix. 40
3.3 Flow boiling heat flux and mass flux test conditions. 40
3.4 Material property comparison for particle selection [55–59]. 41
3.5 Pool boiling test matrix. 41
3.6 Comparison quantities for CRUD thickness study and parameter ranges for matching synthetic CRUD to reactor CRUD. 42

4.1 Anion Solution for Layer-by-Layer Assembly: 0.03wt% SiO_2 nanoparticles at pH 9.0. 52
4.2 Cation Solution for Layer-by-Layer Assembly: 10^{-2}M PAH at pH 7.5. 52
4.3 Anion Solution for Layer-by-Layer Assembly: 0.03wt% Fe_3O_4 nanoparticles at pH 4.0. 53

5.1 Pool boiling heaters surface analysis data. Standard deviation values are in parentheses. 69
5.2 Pool boiling heaters CHF values. *Data from *O'Hanley et al.* [7]. . . 70
5.3 Flow boiling synthetic CRUD test matrix. 71
5.4 Uncoated heater surface analysis data. 71
5.5 2μm thick, no chimneys surface analysis data. 74
5.6 2μm thick, 10μm diameter chimneys on 25μm pitch surface analysis data. 76
5.7 4μm thick, 10μm diameter chimneys on 25μm pitch surface analysis data. 78
5.8 2μm thick, 10μm diameter chimneys on 45μm pitch surface analysis data. 80
5.9 2μm thick, 12.5μm diameter chimneys on 27.5μm pitch surface data. 82

1 Milestone Description

1.1 Motivation

CRUD, named for Chalk River Unidentified Deposits, is a layer of corrosion products deposited on fuel rods in nuclear reactor cores. These layers grow by the advection and boiling deposition of metallic ions from corrosion of primary system components and alter the surface properties of the rods. Although CRUD's effects on corrosion (CRUD induced localized corrosion) and reactivity (CRUD induced power shift) have been studied extensively, its effects on reactor thermal-hydraulic performance have received less attention. Conducted research has been aimed primarily at understanding CRUD's composition, morphology, and deposition mechanisms, but CRUD's thermal properties and effects on fuel heat transfer and the boiling crisis are not well understood. Typically, CRUD buildup is considered to be a purely negative by-product of harsh nuclear environments that increases fuel's effective thermal resistance and temperatures. However, CRUD is a naturally occurring hydrophilic porous layer that, in surface characteristics studies, has been found to enhance CHF and increase the Leidenfrost temperature [1–4]. Therefore, in thin layers, CRUD has the potential to enhance heat transfer in the core during normal operation, postpone the boiling crisis in loss of flow accidents (LOFAs) or transient overpower, and accelerate quenching heat transfer following a loss of coolant accidents (LOCA) [5].

Recently, the number of studies on the effects of surface characteristics during boiling heat transfer have increased [3, 6, 7]. With the emergence of nano- to micro-scale fabrication techniques, the ability to create and test new heater surfaces with well-defined thickness, wettability, porosity, roughness, and pore size has allowed for a greater understanding of boiling heat transfer phenomenon. Two particular boiling quantities of interest are the heat transfer coefficient (HTC) and the critical heat flux (CHF). The HTC captures the ability of the fluid to transfer heat efficiently (i.e. with a small temperature difference), while the CHF marks the transition from the nucleate boiling regime to the film boiling regime causing a large reduction in the HTC [8]. This can be considered the upper limit of efficient boiling heat transfer. By manufacturing surfaces with specifically selected properties, it is possible to enhance these properties and create a larger, more efficient nucleate boiling regime.

Due to the complex nature of these phenomena, the prediction of HTC and CHF currently rely heavily on experimental data. However, the cost of these experiments has pushed the engineering community to develop predictive models of reactor performance. Programs, such as the Consortium for Advanced Simulation of Light Wa-

ter Reactors (CASL), have been working towards creating a complete core model, with coupled neutronics, thermal hydraulics, and materials information that captures CRUD's evolution during operation [9]. Models that simulate CRUD's effects on core thermal-hydraulics are essential to the prediction of thermal margins that relate to both reactor safety and economic performance. These models will also increase the understanding of possible positive and negative consequences that could push the nuclear industry to not only model CRUD, but also control its thickness and morphology for optimized thermal performance throughout the irradiation cycle. However, there is currently insufficient experimental information required for accurate model validation.

1.2 Objectives

This work seeks to better understand the effects of CRUD buildup and morphology on heat transfer coefficient and other boiling quantities of interest. This objective is accomplished by:

1. Creating well-defined and characterized, synthetic CRUD with parameters representative of reactor CRUD on MIT test heaters.

2. Experimentally studying the effects of synthetic CRUD on boiling heat transfer, especially heat transfer coefficient (HTC), critical heat flux (CHF), bubble nucleation density, bubble departure frequency, and bubble departure diameter in pool and subcooled flow boiling.

2 Relevant Theory

It is important to study the mechanisms of boiling as well as the characteristics of CRUD to better understand how they relate. First, the integral parameters of boiling heat transfer in both pool and subcooled flow boiling are explained. Next, surface characteristics, such as wettability, roughness, and porosity are defined and previous research adjusting these properties is reviewed. Finally, CRUD morphology is discussed in terms of these surface parameters and its potential effects on boiling are explored through developed models using boiling fundamentals and heat transfer mechanisms. The correlations presented here are believed to be representative of observed trends, although many other correlations exist. Variables are defined at their first use.

2.1 Boiling Heat Transfer

2.1.1 Boiling Fundamentals

Nucleation

The nucleation of vapor bubbles indicates the beginning of the nucleate boiling regime. Bubble nucleation occurs by heterogenous nucleation, or nucleation from a cavity on the heater surface. Homogenous nucleation can occur in the bulk fluid, but requires very large superheat values and a cavity-free surface, whereas heterogeneous nucleation occurs at low superheats [8]. At wall temperatures enough above the liquid saturation temperature, heat is conducted from the surface to the liquid and nucleation occurs at the cavities, as shown in Figure 2-1.

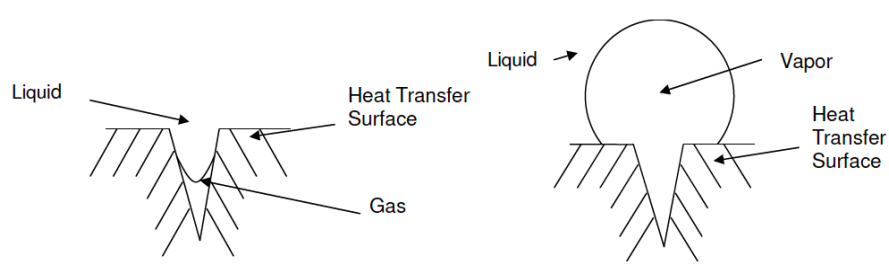

Figure 2-1: Example of a nucleation site before and after bubble growth. Adopted from Phillips [10].

To form a nucleation site, the cavity must have the ability to retain some gases when in contact with water [8]. This ability is determined by the contact angle of the liquid on the heater surface compared to the angle of the cavity. The contact angle of the liquid is defined as the angle between the liquid-vapor interface and the solid surfaced measured at liquid, as shown in Figure 2-2. A conical cavity is able to trap vapor if the advancing contact angle of the liquid is greater than the cavity angle [8].

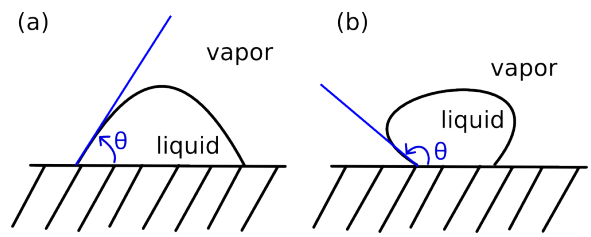

Figure 2-2: The contact angle of a (a) hydrophilic (well wetting) (b) hydrophobic (water repellent) surface.

Bubble growth is dictated by the cavity size and begins when the required superheat has been reached. Typical nucleation sites have a radius on the order of 0.1-10μm. The minimum liquid superheat for bubble growth is given by equation 2.1 [11]:

$$(\Delta T_{sat})_{nucleation} > \frac{2\sigma T_{sat}(p_l)\nu_g}{h_{fg}R} \tag{2.1}$$

where σ is the surface tension, ν_g is the specific volume of vapor, h_{fg} is the enthalpy of vaporization, R is the cavity mouth radius, and T_{sat} and ΔT_{sat} are the saturation and wall superheat temperatures, respectively. The mechanical equilibrium state of a bubble is given by the Young-Laplace equation [8]:

$$P_v - P_l = \frac{2\sigma}{r} \tag{2.2}$$

where P_v and P_l are the vapor and liquid pressures, σ is the surface tension, and r is the equilibrium radius size.

Nucleation Site Density

The nucleation site density (N'') refers to the number of nucleation sites on the surface per unit area. Bubbles will form and depart from the surface at these sites, although not all sites will be active for a given heat flux.

Many of the models used to predict nucleation site density were developed for pool boiling and therefore cannot be directly applied to flow boiling. However, they still provide insight into the effects of different flow parameters on nucleation site density. A widely used correlation is the *Lemmert-Chawla* correlation, shown in equation 2.3 [12].

$$N'' = (m\Delta T_{sup})^p \tag{2.3}$$

where N'' is the nucleation site density, ΔT_{sup} is the wall superheat, and m and p are 185.0 and 1.805, respectively.

In 2003, *Hibiki and Ishii* created a nucleation site density model validated by pool and flow boiling systems that accounts for critical cavity size and contact angle, shown in equations 2.4 - 2.7 [13]. These variables are important to determining whether a site contains trapped gases and, therefore, if it is active.

$$N_n = \bar{N}_n \left\{1 - exp\left(-\frac{\theta^2}{8\mu^2}\right)\right\}\left[exp\left\{f(p^+)\frac{\lambda'}{R_c}\right\} - 1\right] \tag{2.4}$$

where $\bar{N}_n$ is the reference nucleation site density equal to 4.72×10^5 sites/m^2, μ is the characteristic cone angle scale equal to 0.722 rad, λ' is the cavity length scale equal to 2.50×10^{-6}m, θ is the contact angle, and R_c is the minimum cavity size.

$$R_c = \frac{2\sigma\left\{1 + (\rho_g/\rho_f)\right\}/P_f}{exp\left\{h_{fg}(\Delta T_{sup})/(RT_wT_{sat})\right\} - 1} \tag{2.5}$$

$$f(\rho^+) = -0.01064 + 0.48246\rho^+ - 0.22712\rho^{+2} + 0.05468\rho^{+3} \tag{2.6}$$

$$\rho^+ = log\left(\frac{\rho_f - \rho_g}{\rho_g}\right) \tag{2.7}$$

Here, R is the gas constant, ρ_f and ρ_g are the vapor and liquid densities, σ is the surface tension of the fluid, P_f is the liquid pressure, and T_w, T_{sat}, and ΔT_{sup} are the wall, saturation, and superheat temperatures, respectively.

In 2002, *Basu et al.* proposed an empirical correlation accounting for contact angle during forced convective boiling on a vertical surface based on experimental data [14]. This correlation is given in equations 2.8 and 2.9.

$$N_{nc} = 0.34(1 - cos\theta)\Delta T_{sup}^2, \qquad \Delta T_{ONB} < \Delta T_{sup} < 15K \tag{2.8}$$

$$N_{nc} = 3.4 \times 10^{-5}(1 - cos\theta)\Delta T_{sup}^{5.3}, \qquad 15K \leq \Delta T_{sup} \tag{2.9}$$

Bubble Departure Frequency

The bubble departure frequency is often measured with the nucleation site density. For a given nucleation site at quasi-steady state, bubbles will depart from the surface with a frequency defined by the bubble growth time (t_g) and wait time (t_w), as shown in equation 2.10.

$$f = \frac{1}{t_g + t_w} \tag{2.10}$$

The growth time describes the time for a bubble to form and depart from the surface, while the wait time describes the time it takes until the next bubble begins to form. *Yeoh and Tu* developed a mechanistic frequency model based on a model by *Han and Griffith* [15] that corrected for contact angle [16]. This model is shown in

equations 2.11 - 2.14,

$$t_w = \frac{1}{\pi\alpha}\left[\frac{(T_w - T_b)C_1 r_c}{\Delta T_{sup} + 2\sigma T_{sat}/C_2\rho_g h_{fg} r_c}\right] \tag{2.11}$$

$$C_1 = \frac{1 + cos\theta}{sin\theta} \tag{2.12}$$

$$C_2 = \frac{1}{sin\theta} \tag{2.13}$$

$$t_g = \frac{1}{16}\frac{\pi}{\alpha}\frac{D_{sl}^2}{b^2 Ja^2} \tag{2.14}$$

where α is the thermal diffusivity, θ is the contact angle, r_c is the cavity radius, D_{sl} is the bubble sliding diameter, b is a constant equal to 0.21, and Ja is the Jakob number, defined in equation 2.15.

$$Ja = \frac{\rho_f C_{pf}\Delta T_{sat}}{\rho_g h_{fg}} \tag{2.15}$$

Basu developed a simple empirical model for the bubble departure frequency [17, 18]. This model is shown in equations 2.16 - 2.18.

$$t_w = 139.1(\Delta T_{sup}^{-4.1}) \tag{2.16}$$

$$\frac{D_d^2}{\alpha t_g} = 45Ja \cdot exp(-0.02Ja_{sub}) \tag{2.17}$$

$$Ja_{sub} = \frac{\rho_f C_{pf}\Delta T_{sub}}{\rho_g h_{fg}} \tag{2.18}$$

In this model, D_d is the bubble departure diameter. All other variables are as previously defined.

Bubble Departure Diameter

Bubbles depart from the surface, either by liftoff or sliding, when the forces holding the bubble at its nucleation site are overcome by forces moving the bubble from the surface. The diameter of the bubble when it detaches is called the bubble departure diameter. The model explored below was proposed by *Klausner et al.* [19] and modified by *Sugrue et al.* [20]. The model defines the forces that act on the bubble, as shown in equations 2.19 and 2.20. A diagram showing the forces and their directions can be seen in Figure 2-3.

$$\sum F_x = F_{sx} + F_{qs} - F_b sin\vartheta + F_{du} sin\phi \tag{2.19}$$

$$\sum F_y = F_{sy} + F_{sL} - F_b cos\vartheta + F_{du} cos\phi - F_h + F_{cp} \tag{2.20}$$

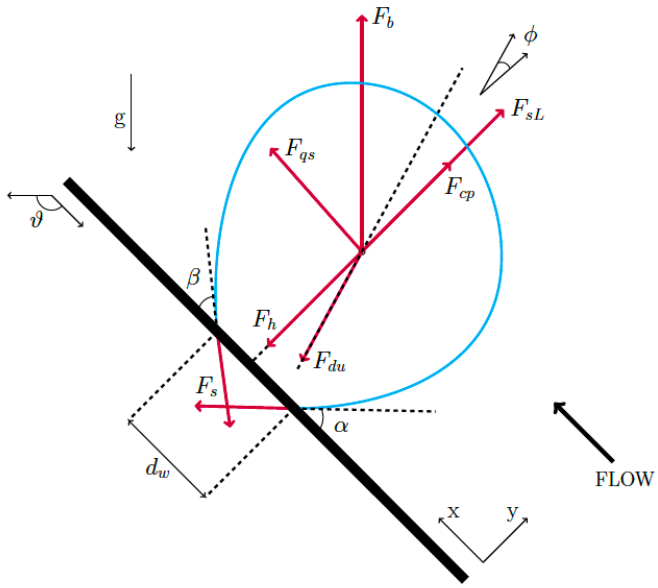

Figure 2-3: Sugrue et al. force balance model for bubble departure diameter. Adopted from Sugrue [20].

F_s is the surface tension force, F_{qs} is the quasi-steady drag force, the F_b is the buoyancy force, F_{du} is the unsteady drag force, F_{sL} is the shear lift force, F_h is the hydrodynamic pressure force, and F_{cp} is the contact pressure force. When the force balance is broken in either the x or y direction, the bubble will detach from the surface. The surface tension force holds the bubble to the surface while the shear lift force, caused by velocity distributions, pulls the bubbles away from the wall. The quasi-steady drag force is caused by drag on the bubble while the unsteady drag is created from the asymmetry of the bubble growth. More information about this model and its formulation can be found in Sugrue et al. [20].

2.1.2 Pool Boiling

In pool boiling, heat transferred from a surface to a stationary fluid. Pool boiling is best described through the characteristic boiling curve, shown in Figure 2-4.

The pool boiling curve is defined by multiple heat transfer regions [8]. The first region (I) occurs at very low heat fluxes, between Points A and B, and is dominated by natural convection. The temperature of liquid near the surface increases and rises because of its lower density and is replaced by colder water. As the heat flux increases, the surface reaches Point B where the wall superheat becomes large enough to allow nucleation from surface cavities. This is defined as the onset of nucleate boiling (ONB). This point indicates the beginning of the nucleate boiling region (II). Nucleation is efficient at removing heat from a surface due to the large latent heat required for evaporation. Therefore, the temperature increases more slowly with heat flux in this region than in the natural convection region.

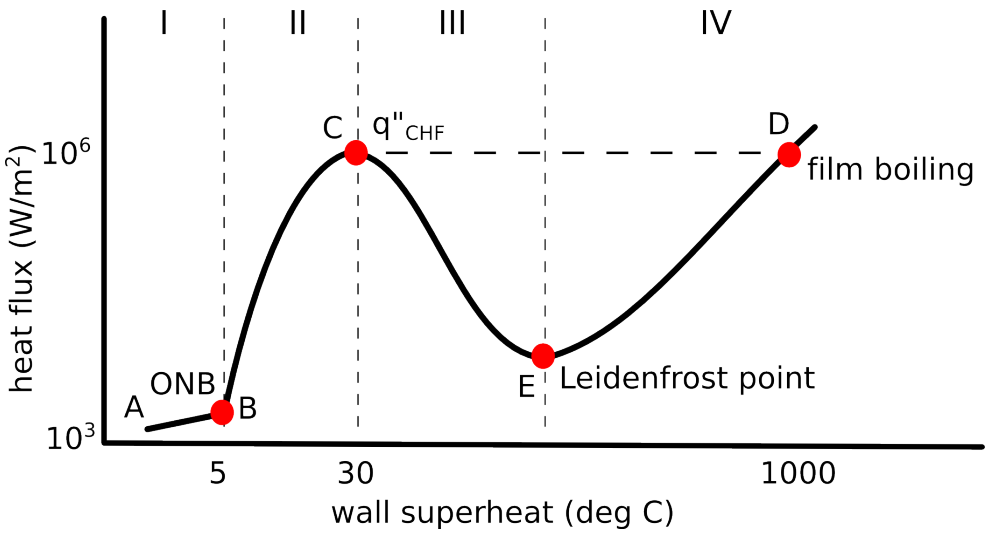

Figure 2-4: Characteristic pool boiling curve.

The nucleate boiling region continues until the surface is no longer able to efficiently remove the energy. At point C, the heat transfer coefficient of the surface significantly decreases. This is defined as the critical heat flux (CHF) or departure from nucleate boiling (DNB). In an experiment with an imposed heat flux, the surface will instantaneously transition to point D in the film boiling region (IV) and experience a very large temperature increase. In film boiling, heat must be transferred through a thin, continuous vapor film covering the surface before it can be removed by the liquid. Decreased efficiency of heat transfer by the vapor film is responsible for the rise in temperature. Once film boiling is established, it can be maintained at lower heat fluxes from point D to point E. Point E is known as the Leidenfrost point and is defined as the minimum stable film boiling temperature. Most heat transfer applications occurs in regions I and II where the boiling heat transfer coefficient is highest.

2.1.3 Subcooled Flow Boiling

Subcooled flow boiling may occur in a channel where heat is transferred to a moving liquid at a temperature below the saturation point. The boiling curve is similar to that shown in Figure 2-4; however, region I is dominated by forced convection rather than natural circulation. Figure 2-5 shows the flow patterns and heat transfer regions as they change with increasing steam quality, or mass of vapor in the channel, and wall temperature [21].

When the liquid enters the channel, it is subcooled. Once the wall reaches a superheat sufficient for bubble formation, heat is removed by subcooled boiling. The bulk fluid temperature rises and, once it reaches saturation, flow enters the saturated nucleate boiling region. As the quality increases, the flow pattern transitions from bubbly flow to slug flow and then annular flow, characterized by a vapor column through the center of the channel with a thin liquid film in contact with the walls

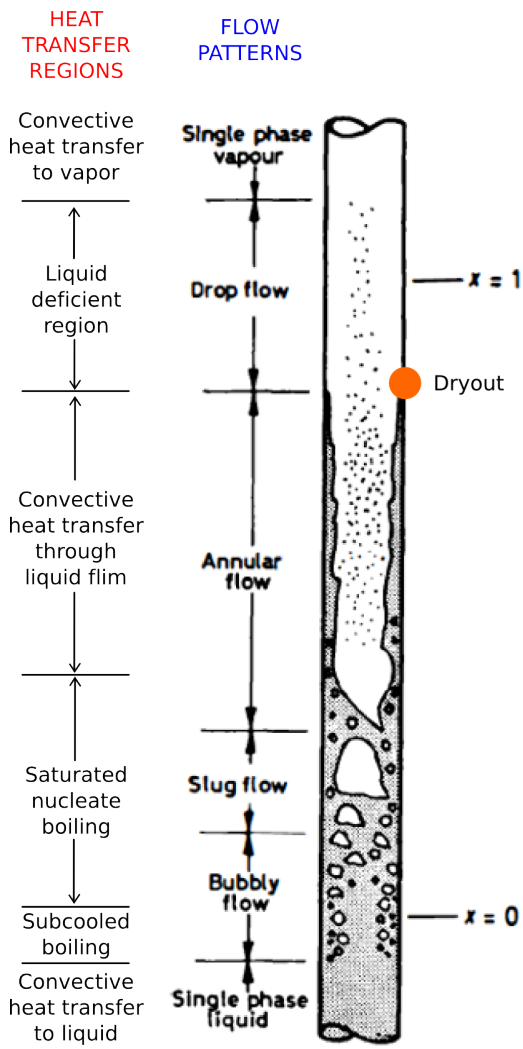

Figure 2-5: Regions of heat transfer in convective flow boiling with uniform wall heat flux. Adopted from Collier [21].

and droplets entrained by the vapor. When the fluid reaches annular flow, the heat removal becomes dominated by convective heat transfer through the thin liquid film and then evaporation at the surface of the liquid film. When the thin liquid film is completely evaporated, the channel has reached dryout, where, similar to DNB, the wall temperature quickly increases and the HTC significantly decreases.

2.1.4 Boiling Heat Transfer Models

In many applications, it is necessary to describe the efficiency of heat removal from a surface. This quantity is known as the heat transfer coefficient, h, defined in equation 4.4,

$$h = \frac{q''}{T_w - T_b} \tag{2.21}$$

where q'' is the heat flux. Using this formula, the HTC of a surface can be directly measured. Given the difficultly in predicting boiling parameters discussed above, such as the nucleation site density, bubble departure frequency, and bubble departure diameter, there are no complete HTC correlations. *Rohsenow (1952)* proposed that the single-phase convective heat transfer correlation could be modified for boiling, as shown in equation 2.22 [22].

$$Nu = \frac{1}{C_{sf}} Re^{1-n} Pr^{-m} \tag{2.22}$$

The Nusselt number, Nu, defined as hL/k, is the ratio of convective to conductive heat transfer for a characteristic length, L, and thermal conductivity, k. C_{sf} is a constant dependent on the surface-fluid combination, while n and m are constants equal to 0.33 and 0.7, respectively. Due to variations in C_{sf}, it is often necessary to conduct experiments for a given setup.

Jens and Lottes (1951) developed a simple correlation for subcooled and saturated nucleate boiling of water at pressures between 3.45 and 6.89 MPa, shown in equation 2.23 [23],

$$T_w - T_{sat} = 25 q''^{0.25} exp(-P/6.2) \tag{2.23}$$

where q'' is in MW/m^2, P is in MPa, and T is in °C.

Chen (1963) developed an HTC correlation applicable to the saturated boiling region up to DNB that accounts for both forced convection and nucleate boiling contributions [24]. This correlation takes for form of equation 2.24.

$$h_{2\phi} = h_c + h_{NB} \tag{2.24}$$

The convection heat transfer coefficient, h_c, is a modified version of the *Dittus-Boelter* correlation:

$$h_c = 0.023 \left(\frac{G(1-x)D_e}{\mu_f} \right)^{0.8} (Pr_f)^{0.4} \frac{k_f}{D_e} F \tag{2.25}$$

where G is the mass flux, x is the vapor quality, D_e is the hydraulic diameter and F accounts for the greater turbulence caused by vapor in the channel. The nucleation heat transfer coefficient, h_{NB} is based on the *Forster-Zuber* equation [25] and is shown in equation 2.26.

$$h_{NB} = S(0.00122) \left[\frac{(k^{0.79} c_p^{0.45} \rho^{0.49})_f}{\sigma^{0.5} \mu_f^{0.29} h_{fg}^{0.24} \rho_g^{0.24}} \right] (T_w - T_{sat})^{0.24} (P(T_w) - P(T_{sat}))^{0.75} \tag{2.26}$$

S is defined as the suppression factor, or ratio of mean superheat to the wall superheat, and is a function of the total Reynolds number of the flow. Correlations for F and S can be found in Chen [24].

Collier and Thome (1994) extended the Chen correlation to the subcooled boiling region by setting F equal to 1 (no vapor) and calculating S using the single-phase Reynolds number (x=0) [21].

Klimenko (1990) studied the effects of tube diameter and orientation on two-phase flow and developed two heat transfer coefficient correlations, one for the nucleate boiling dominated region (bubbly flow) and one for the forced evaporation dominated region (annular flow). These correlations are shown in equations 2.27 and 2.28, respectively [26].

$$Nu_{NB} = \frac{h_{NB}b}{k_f} = 4.9 \times 10^{-3} Pe_m^{0.6} Pr_f^{-0.33} \left(\frac{Pb}{\sigma}\right)^{0.54} K_\lambda^{0.12} \tag{2.27}$$

$$Nu_c = \frac{h_c b}{k_f} = 0.087 Pe_m^{0.6} Pr_f^{1/6} \left(\frac{\rho_g}{\rho_f}\right)^{0.2} K_\lambda^{0.09} \tag{2.28}$$

In the above equations, Pr_f is the liquid Prandtl number, Pe_m is the modified Peclet number, Re_m is the modified Reynolds number, b is the Laplace constant, and K_λ is the ratio of the wall thermal conductivity to the liquid thermal conductivity. Similar to *Rosenhow*, this correlation attempts to capture specific surface/fluid combination effects. *Klimenko* also defined a convective boiling number, shown in equation 2.29.

$$N_{CB} = \frac{Gh_{fg}}{q''} \left[1 + x\left(\frac{\rho_f}{\rho_g} - 1\right)\right] \left(\frac{\rho_g}{\rho_f}\right)^{1/3} \tag{2.29}$$

When $N_{CB}<1.6\times10^4$, the flow is dominated by nucleate boiling and equation 2.27 should be used. When $N_{CB}>1.6\times10^4$, the flow is dominated by forced evaporation and equation 2.28 should be used.

Kurul and Podowski (1990) proposed a heat flux partitioning model, called the RPI model, that is used extensively in the numerical simulation and CFD modeling of flow boiling [27]. The RPI model divides the total heat flux from the wall into three components, according to equation 2.30,

$$q''_{total} = q''_{fc} + q''_e + q''_q \tag{2.30}$$

where q''_{fc} is the forced convection heat flux, q''_e is the evaporative heat flux, and q''_q is the quenching heat flux. The individual heat flux components are defined in equations 2.31 - 2.33.

$$q''_{fc} = A_c St \rho_l c_{p,l} u_l (T_w - T_b) \tag{2.31}$$

$$q''_e = \frac{\pi}{6} d^3 \rho_v f N'' h_{fg} \tag{2.32}$$

$$q''_q = \frac{2}{\sqrt{\pi}} f N'' A_q \sqrt{t_w k_l \rho_l c_{p,l}} (T_w - T_b) \tag{2.33}$$

A_c and A_q are the areas affected by forced convection and quenching, St is the Stanton number, d is the bubble departure diameter, f is the bubble departure frequency, N'' is the nucleation site density, and t_w is the bubble wait time. This model has also been modified by *Gilman* to include a sliding bubble conduction component, q''_{sc} [28].

CHF is another significant parameter to study in boiling heat transfer applications. CHF can cause catastrophic material failures from temperature increases of

thousands of degrees C. While CHF is not fully understood, there are several proposed theories about the mechanisms responsible for decreased HTC. *Zuber (1959)* developed a model to predict CHF based on hydrodynamic instabilities, shown in equation 2.34 [8],

$$q''_{CHF} = K\rho_g h_{fg}\left[\frac{g\sigma(\rho_f - \rho_g)}{\rho_g^2}\right]^{1/4} \tag{2.34}$$

where q''_{CHF} is the critical heat flux, K is a dimensionless number that describes surface geometry and g is the gravitational constant. In this model, increased vapor velocity leads to instability in vapor jets, causing them to breakdown and inhibit vapor removal from the surface. Other models suggests that bubbles crowding or vapor pockets formed at hot spots on the heater surface will coalesce and form a continuous film, preventing rewetting and initiating CHF [29].

However, Zuber's model, like many others following it, fails to take into account the characteristics of the boiling surface. More recent and advanced models such as *Kandlikar (2001), Polezhaev and Kovalez (1990)*, and *Ramilison (1992)* attempt to predict the pool boiling CHF accounting for factors such as wettability, porosity, and roughness [30–32]. While each of these models contributes to the understanding of these parameters on CHF, studies such as those conducted by *O'Hanley* [3] have demonstrated the coupled natured of these parameters. Therefore, experimental results are still required while moving towards a complete surface characteristics correlation.

2.2 Surface Characteristics

It has been observed many times that the nano- to micro-scale characteristics of a boiling surface can have substantial effects on boiling heat transfer. Specifically, the effects of wettability, roughness, and porosity are able to modify the boiling behavior. As these parameters are ingrained in the definition and manufacturing of synthetic CRUD, they are described in the following section.

2.2.1 Wettability

The wettability of a surface is measured by the contact angle of a droplet at the liquid-vapor interface, as discussed in section 2.1.1. Surfaces are considered neutrally wetting with a contact angle of 90°. Surfaces with contact angles less than 90° are considered hydrophilic, or well wetting, while surfaces with contact angles greater than 90° are defined as hydrophobic, or water repellent. Hydrophilicity attracts water to the surface and increases rewetting; however, this wetting tends to decrease nucleation. Hydrophobic surfaces have the opposite effect. Hydrophobic layers are less able to rewet the surface; however, they promote increased nucleation.

Roughness can also affect the wettability of the surface. Figure 2-6 demonstrates the Wenzel regime, where the liquid penetrates the roughness, and Cassie regime, where the liquid remains outside the roughness. Roughness tends to magnify pre-

existing hydrophilicity or hydrophobicity. Therefore, rough hydrophilicity tends to result in the Wenzel regime, while rough hydrophobicity behaves in the Cassie regime.

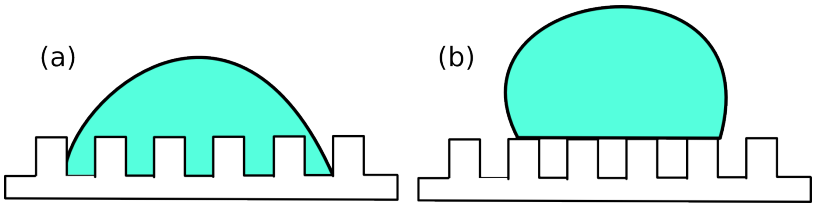

Figure 2-6: Wettability regimes (a) Wenzel (b) Cassie.

2.2.2 Roughness

Roughness is used to measure the texture of a surface. It is a measure of the vertical deviation from a perfectly smooth surface. Roughness has also been documented, most famously by *Berenson* [33], to have large effects on pool boiling HTC due to the increase in active nucleation sites. There are several parameters that can be used to quantify linear roughness. R_a is defined as arithmetic average of the absolute values of surface features, as shown in equation 2.35 and illustrated in Figure 2-7.

$$R_a = \frac{1}{L}\int_0^L |z(x)|\, dx \tag{2.35}$$

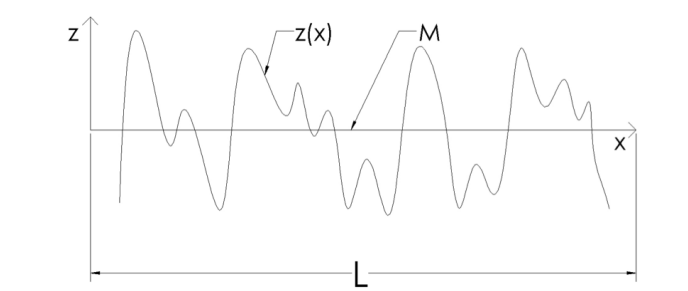

Figure 2-7: R_a: Arithmetic average roughness. Adopted from O'Hanley [7].

$z(x)$ is the vertical distance from the mean surface height, M, over a length, L. R_{RMS} gives the root mean square of the arithmetic average of surface features. R_t is the maximum height difference between the highest peak and lowest valley over a length, L. r is defined as the roughness ratio, or the total surface area of the rough surface over the projected surface area, or the area if the surface were perfectly smooth. Of these roughness parameters, R_a is the most widely used and will be reported in this study.

2.2.3 Porosity

Porosity is a measurement of the empty space in a material defined as the fraction of the volume of voids over the total volume. The porosity of spherical particle assemblies is determined by the packing arrangement. Spheres can be densely packed, resulting in low porosity (minimum theoretical = 26%), or loosely packed, resulting in higher porosity, as shown in Figure 4.1. In the case of loosely packed particles (50-60% packing fraction), the porosity may vary slightly between individual particles, but will be constant when averaged over a large area [6].

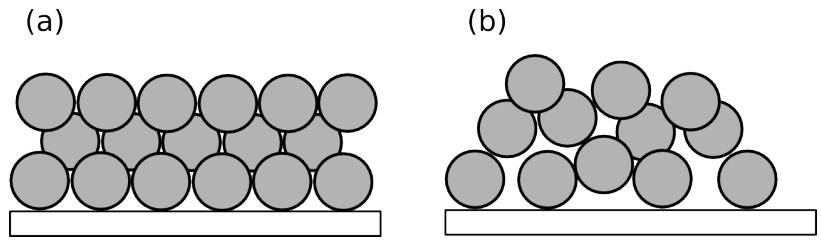

Figure 2-8: Spherical Packing with (a) low porosity (b) high porosity.

Porosity has been proven to greatly enhance CHF on heated surfaces [1–3, 6]. This increase has been attributed to greater bubble nucleation and liquid flux to the surface [34,35]. Porosity introduces cavities able to trap vapor and enhance nucleation on the surface. Interconnected pores also create micro-scale channels dominated by capillary wicking. The capillary forces generate a large liquid flow rate for heat removal while minimizing vapor counter flow resistance and the formation of dry spots that cause CHF. Further discussion of this phenomenon can be found in Section 2.4.2.

O'Hanley et al. developed a set of π-groups governing the capillary wicking driven flow through the porous matrix [3]. The groups are porosity, ε, contact angle, β, the effective pore diameter to effective pore length ratio, D_p/L, and the pore Reynolds number, Re_{pore}, found in equation 2.36 that describes the ratio of inertial to viscous forces through the interconnected passages.

$$Re_{pore} = \frac{\rho_f \sigma D_p}{\mu_f^2} \tag{2.36}$$

μ_f is defined as the is the fluid viscosity. Figure 2-9 shows the dependence of the pore Reynolds number on coolant pressure and pore diameter, D_p. It should be noted that the pore Reynolds numbers at atmospheric and PWR reactor pressures are very similar. This is significant because the experiments in this study are conducted at atmospheric pressure, but will be representative of flows at higher pressure.

2.3 Surface Engineering

Many studies have investigated potential enhancements in boiling heat transfer through the creation of engineered surfaces. As discussed in Section 2.2, surface characteristics such as wettability, roughness, and porosity have the ability to increase the efficiency

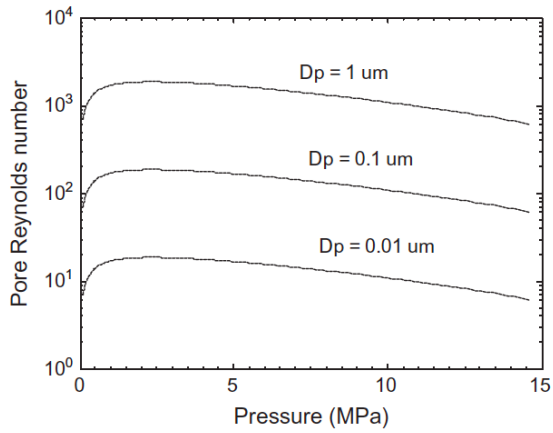

Figure 2-9: Pore Reynolds number variation with pressure and pore diameter [5].

of nucleate boiling. As early as 1962, *Berenson* found that by roughing surfaces with sandpaper of different grits, it was possible to increase the HTC of the surface by up on 600% [33].

More recently, studies have shifted towards nano- to micro-engineered surfaces with finely controlled features. *Wang and Dhir (1993)* concluded that increased wettability resulted in a higher CHF in pool boiling at atmospheric pressure [36]. The wettability of smooth cooper substrates was controlled by changing the degree of oxidation on the surface. However, the HTC of the surface decreased with wettability due to a reduction in nucleation site density. In 2010, *Betz et al.* studied the effects of hydrophilic and hydrophobic spot patterning [37]. It was found that hydrophilic spots on a hydrophobic base had the largest HTC enhancement, but could also decrease CHF. Hydrophobic spots on a hydrophilic base exhibited a lower HTC enhancement, but greatly enhanced CHF. Overall, the greatest HTC and CHF enhancements were 100% and 65%, respectively over purely hydrophilic surfaces.

Chu et al. (2012) experimentally investigated surface roughness with increased wettability [38]. Deep reactive ion etching (DRIE) was used to etch micropillar arrays of varying pitch and diameters into undoped silicon with roughness ratios, r, ranging from 1.79 to 5.94. An oxide layer was then grown to enhance surface wettability. For the roughness surface, an enhancement in CHF of 160% was observed due to the magnified effects of capillary forces. *Dhillon et al. (2015)* explored the effects of varying silicon micropillar arrays with and without nanograss (nano-texture with roughly 100nm length scale) coatings on CHF [39]. Through experiments and models, they found that CHF was again increased by greater liquid flow rate into surface textures and decreased dry spot rewetting time.

Kim et al. (2006) studied the effects of wettability and porosity on boiling heat transfer in nanofluids [1]. Al_2O_3, ZrO_2, and SiO_2 nanoparticles were used to create nanofluids at 0.1%, 0.01%, and 0.001% volume concentrations. Under pool boiling conditions, nanoparticles were deposited onto the heater surface, creating a hydrophilic porous surface that resulted in CHF enhancements of up to 50%. *Forrest et al.* tested PAH/SiO_2 nanoparticle thin films in pool boiling on nickel wires and found

that CHF was enhanced by up to 100% [2]. They also reported that HTC for porous hydrophobic surfaces was enhanced by more than 100% over bare wires while HTC was decreased for porous, hydrophilic coatings. This is consistent with the findings from *Wang and Dhir (1993)*. A further study of hydrophilic porosity was conducted by *Tetreault-Friend (2014)*, also with PAH/SiO_2 nanoparticle surfaces [6]. This investigation explored the effects of porosity from 20% to 60%, pore size from 6nm to 100nm, and layer thickness from 0.5μm to 4μm. The largest CHF enhancement was measured for a coating with a 20nm pore size, 2μm thick. Porosity did not greatly affect the CHF value in the experimental range.

McCarthy (2014) created hydrophilic porous nanostructures with varying size, morphology, and roughness using the Tobacco mosaic virus [40]. This study defined a dimensionless wicking number for each surface as the ratio of liquid flow rate wicked into the structures over the critical mass flow rate of vapor leaving the surface. It was found that for 7 unique hydrophilic porous surfaces, the CHF value was directly proportional to the wicking number.

In 2013, *O'Hanley et al.* conducted a separate effects study where the wettability, roughness, and porosity were independently varied in order to better understand both the individual and coupled effects of these surface parameters [3]. This study reports that altering roughness and non-porous wettability have minimal effects on CHF. However, by coupling wettability with porosity, *O'Hanley* found that hydrophobic porosity decreased CHF by over 90% while hydrophilic porosity increased CHF by 60%.

Mori et al. (2015) studied the effects of porous honeycomb structures [41]. The structures were composed of $CaOAl_2O_3$, SiO_2, and TiO_2 particles. The structure porosity, vapor escape channel width, grid wall thickness, and height of the honeycomb porous plate were 24.8%, 1.4mm, 0.45mm, and 1 mm, respectively. The presence of the honeycomb structure enhanced CHF by up at 2 MW/m^2.

2.4 CRUD

The objective of this study is to manufacture and test synthetic CRUD's effects on boiling heat transfer. Therefore, the structure and heat transfer mechanisms of reactor CRUD must be explored. This section will discuss CRUD morphology and give insight into prior modeling and experimental investigations.

2.4.1 Morphology

CRUD (Chalk River Unidentified Deposits) is a porous layer that collects on the surface of fuel rods during reactor operation. It is composed primarily of nickel oxide (NiO), iron oxide (Fe_3O_4), and trevorite ($NiFe_2O_4$), although relative quantities are unknown and depend greatly on individual reactor chemistry [5, 42]. These oxides are corrosion products of the reactor coolant system piping and components and are transported as particles throughout the reactor coolant system. As nucleate boiling occurs (either subcooled boiling in a PWR or saturated boiling in a BWR), the oxide

particles precipitate onto the fuel pins [43]. CRUD can grow to 10-100μm thick with average pore size, porosity, and roughness values between 0.1-1μm, 40-50%, and 0.5-3.0μm respectively [5]. CRUD also contains characteristic boiling chimneys, which are formed as water is pulled into the porous layer through capillary wicking, evaporates and escapes through the chimneys back into the coolant flow. Boiling chimneys are typically in the 2-10μm range in diameter and have a 5-20μm pitch. This morphology can be seen in Figure 2-10.

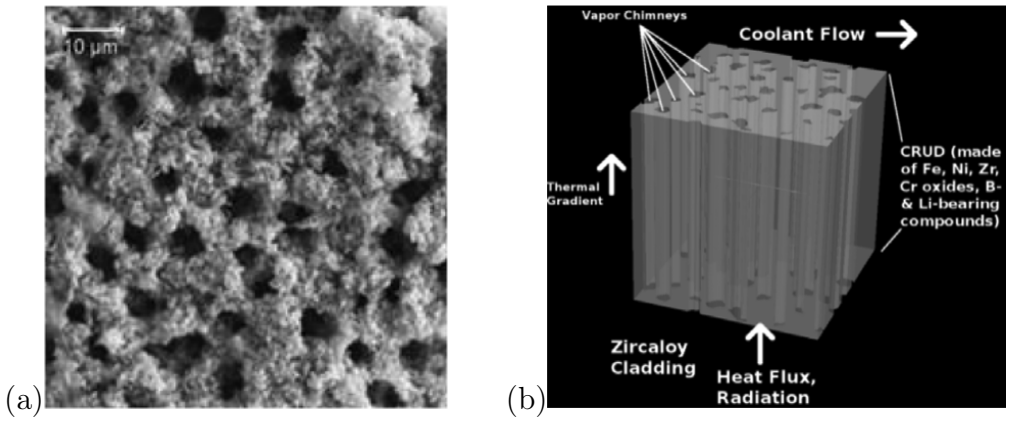

(a) (b)

Figure 2-10: (a) CRUD from a PWR fuel assembly. Adopted from EPRI [44]. (b) CRUD Schematic. Courtesy of M. Short, MIT.

Although corrosion products make up the majority of CRUD, species added to the reactor coolant, such as boron, also contribute to build up on fuel rods, leading to operational problems. Boron added to control reactivity can concentrate in the CRUD and change the neutron flux distribution in subcooled boiling regions, leading to CRUD induced power shifts (CIPS) [45]. Buildup of boric acid (H_3BO_3) and lithium hydroxide (LiOH) in thick CRUD can cause induced localized corrosion (CILC) of the zirconium cladding [5, 46]. However, this study will focus on CRUD deposition's effect on the thermal hydraulics and heat transfer of fuel rods and will neglect those phenomena. As a result, mechanisms of boiling heat transfer, specifically in porous media, must be well defined.

2.4.2 Heat Transfer Mechanisms

In the forced convection region, before boiling occurs, heat is transfer to the fluid mainly by conduction through the CRUD layer. The thermal conductivity of the water-filled CRUD can be estimated using the thermal conductivities of the fluid, k_{fluid}, and solid, k_{solid}, and the porosity, ε, by the Maxwell formula, shown in equation 2.37 [47].

$$k_{CRUD} = k_{fluid}\left[\frac{1-(1-ak_{solid}/k_{fluid})(1-\varepsilon)}{1+(a-1)(1-\varepsilon)}\right] \tag{2.37}$$

where

$$a = \left(\frac{3k_{fluid}}{2k_{fluid}+k_{solid}}\right) \tag{2.38}$$

This formula gives CRUD a thermal conductivity on the order of 1 W/m-K, which leads to temperature gradients of 1°C per μm thickness of CRUD at a heat flux of 1 MW/m^2 [48, 49]. Therefore, at reactor CRUD thickness, the cladding surface temperature can increase by as much as 100°C at a heat flux of 1 MW/m^2.

In nuclear reactors, a larger number of fuel failures are expected than are observed when only accounting for conduction heat transfer through the CRUD [50]. This suggests that the presence of CRUD introduces another boiling mechanism that increases the heat transfer efficiency. This phenomenon is known as wick boiling. In wick boiling, interconnected passages pull water into the porous structure through capillary forces, opposed by viscous forces, and increase rewetting of the boiling surface [50]. This increased coolant flow delays CHF. However, in a purely nano-porous, hydrophilic layer, the heat transfer at high heat fluxes is limited mainly by the vapor's ability to escape the surface [49]. CRUD's formation of boiling chimneys naturally creates an outlet for vapor to quickly leave the porous structure and decrease the boiling surface temperature, increasing the HTC and delaying CHF, as shown in Figure 2-11. The next section discusses models that have been developed to understand this process.

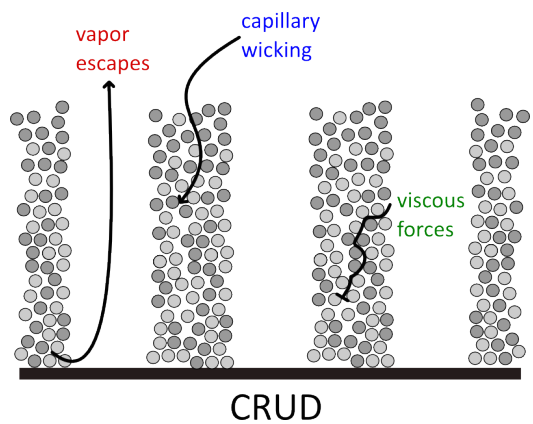

Figure 2-11: Wick boiling diagram showing the locations of interest for capillary wicking, viscous forces, and vapor escape.

2.4.3 Models

Wick boiling was originally proposed by *Macbeth et al. (1971)* who developed a one-dimensional hydraulic model of coolant flow in CRUD and determined the effect of chimney density on maximum allowable heat flux [49]. This model uses liquid and vapor capillary pressure drop equations, shown in equations 2.39 and 2.40, to balance increased pressure at the evaporation front with capillary, laminar friction, and form loss forces.

$$\frac{4\sigma}{D_L} = (P_2 - P_1) + 32h\left(\frac{\mu V}{D^2}\right)_L + (\rho V^2)_L \tag{2.39}$$

$$(P_2 - P_1) = \frac{4\sigma}{D_v} + 32h\left(\frac{\mu V}{D^2}\right)_v + (\rho V^2)_v \tag{2.40}$$

P_1 is the coolant pressure, P_2 is the pressure at the base of the CRUD, D is the capillary diameter, h is thickness of the layer, μ is viscosity, V is velocity and ρ is the density, with respective liquid (L) and vapor (v) subscripts. By eliminating $(P_2 - P_1)$, the liquid velocity and mass flux can be solved for which, when multiplied by the latent heat, gives a theoretical CHF value. *Macbeth* also ran experiments at 69 bar in forced convection flow boiling and found that the presence of CRUD did increase fuel surface temperature, but not by as much as a purely conduction based model would predict [51].

In 1974, *Cohen* presented a one-dimensional model that accounts for heat and mass transfer through the CRUD [52]. An estimate of the wall temperature was obtained by writing an energy equation that balances heat conducted from the surface with liquid evaporation at the chimney surface and heating of the flow in the porous matrix, as shown in equation 2.41.

$$k_{crud}A\frac{\partial^2 T_{sup}(z)}{\partial z^2} = hP[p(T_{sup}, C) - p_0] + \rho_L c_p A\frac{\partial}{\partial z}(V_L T_{sup}(z)) \tag{2.41}$$

A is the porous matrix conduction cross section, $T_{sup}(z)$ is the wall superheat temperature profile through the CRUD, h is the HTC for vaporization, P is the perimeter of the chimney, C is the concentration of solutes, and p and p_0 are the saturation partial pressures in the CRUD and bulk fluid, respectively. From the evaporative losses, the mass flow rate required to replace the liquid inventory and resulting solute concentration gradients were also calculated. Using Cohen's model, an increase in surface temperature was observed with increasing CRUD thickness.

Pan and Jones (1985) developed the first two-dimensional heat and momentum transfer model where temperature distributions are computed as functions of vertical depth in the the CRUD and radial distance from the chimney [48]. This model is derived using Darcy's equation of motion and continuity relations to solve the momentum transport in the porous shell. This is then coupled to the steady-state energy equation defined using the Laplace equation for conduction and corresponding boundary conditions including continuity of heat flux at the chimney wall and zero net heat flux at the cell boundary. Figure 2-12 gives results obtained from this study. θ is defined as the normalized temperature, $(T - T_{sat})/\Delta T_w$ where ΔT_w is the temperature drop due to pure conduction through the layer. ξ is the normalized axial coordinate z/δ where δ is the crud thickness and η is the normalized radial coordinate r/r_v where r_v is the chimney radius. η=1 occurs at the chimney wall where as η=H gives the temperature profile at edge of the unit cell.

As expected, the temperature in the CRUD increases close to the boiling surface (z=0) as well as further from the chimney, but is always less than the pure conduction temperature prediction. Additionally, because the highest temperatures occur far from the chimneys, the need for a two-dimensional model becomes apparent.

Henshaw et al. (2006) built upon Cohen's work to create a one-dimensional model

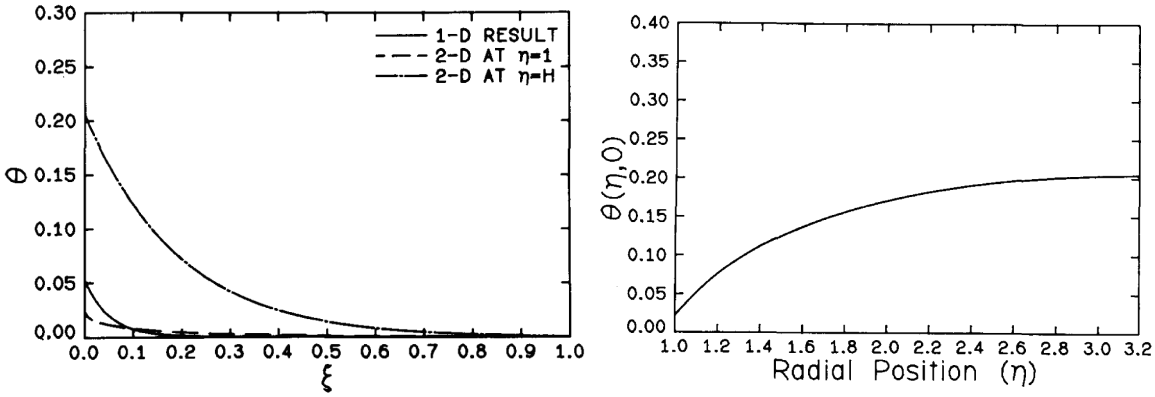

(a) Axial temperature distribution. 1D results are from Cohen's model [52].

(b) Radial temperature distribution.

Figure 2-12: Pan and Jones (1985) CRUD model results. Adopted from Pan and Jones (1985) [48].

that couples thermal hydraulics with water chemistry [53]. The main contribution of this model is the increased understanding of transport and chemistry of dissolved species such as $LiBO_2$ in the CRUD. Due to the temperature dependence of chemical reactions in the porous matrix, the coupling to thermal hydraulics is able to better explain observed CIPS trends due to CRUD growth.

Most recently, *Haq et al. (2011)* created a two-dimensional model that couples heat conduction, flow and boiling of water, and advection of dissolved species [54]. Heat transfer is modeled by the Laplace equation, $\bigtriangledown^2 T = 0$, flow of water is modeled as diffusive flow with velocities related to pressure gradients according to Darcy's law, $u = -k \bigtriangledown p$, and the advection of species is modeled in terms of net current and concentrations, $J = -D \bigtriangledown C + uC$. The above equations are solved using a central-differencing, finite-volume approach. Boundary conditions can be found in *Haq et al.* [54].

This model calculates temperature and species concentration distributions in the CRUD and again confirms that the majority of heat is removed from the surface radially through the chimneys rather than by conduction through the porous structure, as shown in Figure 2-13.

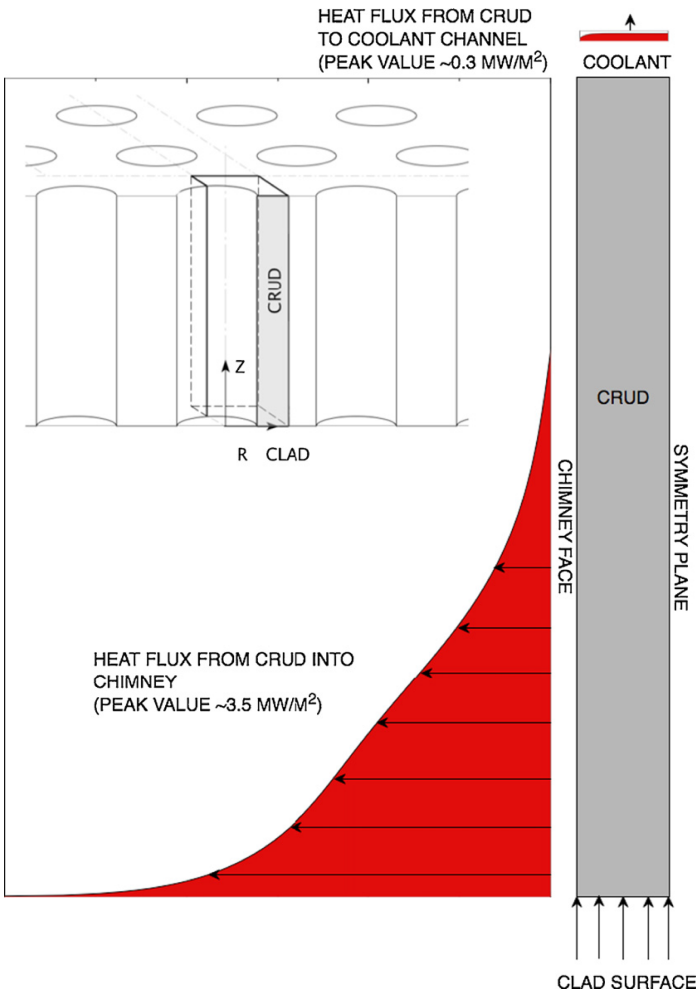

Figure 2-13: Distribution of heat flux from the CRUD. Adopted from Haq et al. [54].

3 Test Matrix

CRUD deposits can vary widely in terms of thickness and chimney pitch and diameter. However, the effects of these differences on boiling efficiency is not well understood. In this investigation, these parameters are varied individually to isolate the separate effects of each on HTC, nucleation site density, bubble departure frequency, and bubble departure diameter. Other parameters such as roughness, wettability, porosity and pore size are kept constant within the range of reactor CRUD.

3.1 Synthetic CRUD Test Matrix

Synthetic CRUD is designed and manufactured to closely match significant parameters of reactor CRUD. These parameters of both reactor and synthetic CRUD are

Table 3.1: Reactor CRUD vs. synthetic CRUD morphology comparison [5].

Parameter	*Reactor CRUD*	*Synthetic CRUD*
Composition	Fe_3O_4, NiO, $NiFe_2O_4$, ZrO_2	SiO_2
Thickness	10-100μm	2-6μm
Thermal Resistance	1-20 $\frac{\mu m-m-K}{W}$	3.5-11 $\frac{\mu m-m-K}{W}$
Roughness	R_a ~0.5-3.0μm	R_a ~0.1-1.0μm
Wettability (contact angle)	10-30°	15-20°
Porosity	40-50%	60-65%
Pore Size	0.1-1μm	~0.1μm
Chimney Diameter	2-10μm	10-15μm
Chimney Pitch	5-20μm	25-45μm

listed in Table 3.1. To investigate the effects of thickness and chimney pitch and diameter, a base synthetic CRUD case of 2μm thickness with 10μm chimney diameter on 25μm chimney pitch was selected. From this case, the parameters were varied individually to create different cases. Three heater patterns were used to study each individual effect (thickness, pitch, diameter). The full test matrix in defined in Table 3.2.

Table 3.2: Synthetic CRUD test matrix.

	Case	*Thickness(μm)*	*Chimney diameter(μm)*	*Chimney pitch(μm)*
Effect of chimneys	1	2	no chimneys	no chimneys
	2	2	10	25
Effect of thickness	2	2	10	25
	3	4	10	25
	4	6	10	25
Effect of pitch	2	2	10	25
	5	2	10	35
	6	2	10	45
Effect of diameter	2	2	10	25
	7	2	12.5	27.5
	8	2	15	30

3.2 Flow Boiling Test Matrix

The flow boiling conditions were adopted from *Phillips (2014)* [10] to ensure synthetic CRUD results are directly comparable to those of uncoated heaters. Heat flux and mass flux values explored are given in Table 3.3 and represent the full range available with the experimental setup. Data was collected for all test conditions on each heater pattern at 10°C constant subcooling. For more information about the rationale behind heat flux, mass flux, and subcooling selections, please refer to *Phillips (2014)* [10].

Table 3.3: Flow boiling heat flux and mass flux test conditions.

	Mass Flux (kg/m^2 - s)				
Heat Flux (kW/m^2)	250	500	750	1000	1250
100	x	x	x	x	x
200	x	x	x	x	x
300	x	x	x	x	x
400	x	x	x	x	x
500	x	x	x	x	x
600	x	x	x	x	x
700	x	x	x	x	x
800	x	x	x	x	x
1000	x	x	x	x	x
1200	x	x	x	x	x
1400		x	x	x	x
1600				x	x

3.3 Rationale and Limitations

As can be seen from Table 3.1, not every parameter of synthetic CRUD directly matches that of reactor CRUD. The purpose of this investigation is not to exactly replicate reactor CRUD, but to create a surface coating with similar morphology that is directly comparable under boiling conditions. Those differences are explained here.

3.3.1 Material Selection

Reactor CRUD is composed primarily of iron oxide, nickel oxide, zirconium oxide, and trevorite, as discussed in Section 2.4.1. Several methods to deposit Fe_3O_4 nanoparticles of both 80nm and 200nm diameters were attempted, but were unsuccessful. Previous studies in MIT's Reactor Thermal Hydraulics Laboratory had been conducted with silica nanoparticles [6, 7], so SiO_2 was selected as a material substitute due to its stability in solution and large negative zeta potential, which makes it easier to deposit on our custom-made heaters. Despite its different chemical makeup, the properties of SiO_2 suggest that it would be an acceptable alternative to manufacturing CRUD with Fe_3O_4 or NiO, as shown in Table 3.4. To ensure results will be representative of reactor CRUD, comparative 10 nm particle tests have been run with both SiO_2 and Fe_3O_4 nanoparticles, as shown in Table 3.5. Other properties such as wettability, porosity, and pore size were kept constant. These tests have also been used to quantify the enhancement in HTC and CHF (which is not tested in flow boiling) due to the porous matrix with and without chimney features in pool boiling.

Table 3.4: Material property comparison for particle selection [55–59].

Properties at 298 K	*Fe_3O_4*	*NiO*	*SiO_2*	*TiO_2*	*ZnO*
Density, ρ (g/cm^3)	5.17	5.72	2.20	4.17	5.60
Thermal Cond., k (W/mK)	7.0	20.2	1.34	8.40	29
Specific Heat, c_p (J/kgK)	0.62	0.53	0.74	0.71	0.50
Thermal Diff., α (m^2/s)	2.2×10^{-6}	6.7×10^{-6}	8.2×10^{-7}	2.8×10^{-6}	1.0×10^{-5}
Surface Energy, E (J/m^2)	0.79	2.4	1.0	1.29	1.31

Table 3.5: Pool boiling test matrix.

Case	*Material*	*Thickness(μm)*	*Chimney diameter(μm)*	*Chimney pitch(μm)*
1	Fe_3O_4	2	no chimneys	no chimneys
2	Fe_3O_4	2	10	25
3	SiO_2	2	no chimneys	no chimneys
4	SiO_2	2	10	25

3.3.2 Thickness

From Table 3.4, it is shown that the thermal conductivities of iron oxide and nickel oxide differ from silica by a factor of five to fifteen. Therefore, the temperature of the wall in the case of silica nanoparticle CRUD will be higher than that of reactor CRUD of the same thickness and porosity. In order to have a consistent temperature increase across the CRUD layer, the thermal resistance must be equivalent in both cases. Additionally, the relevant dimensionless number D_p/L and capillary wicking to viscous force ratio defined by pore size must also be considered. Therefore, in the thickness analysis, thermal resistance, D_p/L, and pore size are all compared between reactor and synthetic CRUD. The thermal conductivity of each material was adjusted, accounting for 50% spherical porosity according to Equation 3.1, where P is the porosity and k_{TD} is the zero porosity thermal conductivity [8].

$$k = \frac{1-P}{1+0.5P} k_{TD} \tag{3.1}$$

The minimum and maximum values of the above quantities were calculated for reactor CRUD, using in values in Table 3.4 and nickel to iron ratios of 0.6 to 2.2 as boundaries. Required thickness, L, and pore size, D_p, were then found to match those ranges. The results are given in Table 3.6.

Table 3.6: Comparison quantities for CRUD thickness study and parameter ranges for matching synthetic CRUD to reactor CRUD.

Parameter	*Metric*	*Quantity to Match*	*Range*
Thermal resistance	$\frac{L}{k}$ for a flat plate	L (μm)	0.83-11.21
Dimensionless number	$\frac{D_p}{L}$	D_p (μm)	0.011-0.083
Force ratios	D_p	D_p (μm)	0.1-1

Any combination of the above values will give thermal resistance, D_p/L, and pore size values in the range of reactor CRUD. While the particle size required to match the D_p/L is lower than the required pore size range, the maximum D_p increases to 0.2μm with a minimum thickness, L, of 2μm. This places 100nm particles in the range for both dimensionless number and pore size. Using silica nanoparticles allows the experimental test matrix to explore a greater range of actual CRUD thickness without the same manufacturing constraints. Figure 3-1 gives a thermal resistance vs. thickness comparison of different materials. From this, a range of 2-6μm silica CRUD will represent reactor CRUD thickness of 20-70μm.

3.3.3 Porosity and Pore Size

The porosity of synthetic CRUD is slightly higher than the porosity of reactor CRUD. *Tetreault-Friend (2014)* [6] measured the porosity of this 100nm SiO_2 LbL coating as 65%. Smaller particles were found to assemble in slightly lower porosity (40-60%), however larger particles were required for this study. *Tetreault-Friend (2014)* also

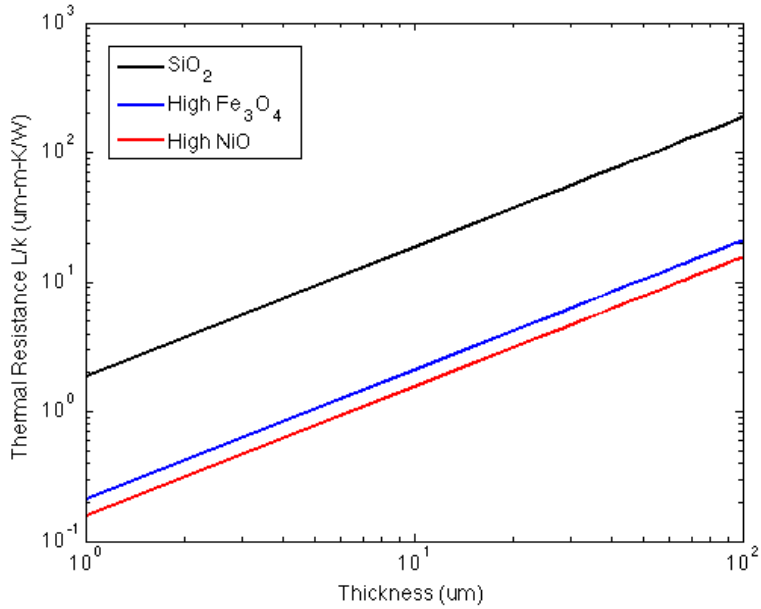

Figure 3-1: Thermal resistance vs. layer thickness for different materials.

presented methods of decreasing porosity by LbL assembly of polymers, but this was outside the scope of this investigation.

4 Experimental Methods

This research aims to provide experimental results regarding the effects of CRUD on boiling heat transfer, used to better understand underlying boiling mechanisms. This objective is accomplished by creating synthetic CRUD on specially-designed indium-tin oxide (ITO) sapphire heaters through micro and nano fabrication techniques. These surfaces undergo detailed feature verification to ensure the surface parameter criteria outlined in Table 3.1 (thickness, roughness, wettability, porosity, pore size, and chimney features) are met. Due to the extreme sensitivity to small variations of these manufacturing processes, each modification on every heater is checked before continuing. Finally, the synthetic CRUD surfaces are tested in pool and flow boiling facilities. The surface manufacturing, testing, and data analysis processes are described in detail in the following chapter.

4.1 ITO-Sapphire Heaters

Indium-tin oxide (ITO) sapphire heaters act as the base for the synthetic CRUD experiments. These heaters, manufactured by Diamond Coatings, have been used extensively in MIT's Reactor Thermal Hydraulics Laboratory. The ITO sapphire surface provides a nano-smooth platform important for surface characteristic studies and has proven robust to necessary manufacturing. The heater is composed of a highly optically transparent sapphire substrate with a scratch-dig rating of 40-20. Deposited on the sapphire is a conductive ITO thin film that is used as a resistive heating element. The ITO film is also infrared (IR) opaque and therefore provides a spatial temperature signal of the heater surface. Two 800nm thick gold pads are sputtered onto the ends of the ITO in MIT's Microsystem Technology Laboratory: Exploratory Materials Laboratory (MTL:EML) to provide attachment points for electrodes. These electrodes are attached to the gold pads with highly conductive silver epoxy to reduce any contact resistance at the pads.

This work focuses on the effects of synthetic CRUD in flow boiling heat transfer. However, pool boiling tests are also conducted for material composition comparisons as well as to isolate the effects of chimneys on HTC and CHF. Therefore, due to the differences in the testing facilities, slightly different sizings and configurations of heaters are used for pool and flow boiling, although the materials and functionality is the same.

CASL-U-2015-0319-000

4.1.1 Pool Boiling Design

Pool boiling heater substrates are made of 50.8mm square sapphire, 0.25mm thick. A 700nm thick, 20mm wide layer of ITO was deposited across the length of the heater. Gold pads were sputtered 20.4mm wide on each end of the ITO, leaving an active heater area of 10mm × 20mm with a resistivity of $<10\frac{\Omega}{cm^2}$. A pool boiling heater diagram with dimensions can be found in Figure 4-1. This heater is tested in an inverted configuration where the sapphire substrate is used as the nano-engineered surface and is in contact with water. This arrangement eliminates corrosion of the electrodes that would occur if they were in contact with water. An IR camera is used to image the ITO and gather two dimensional temperature profiles during testing. The temperature at the boiling surface is then calculated using the heat conduction equation.

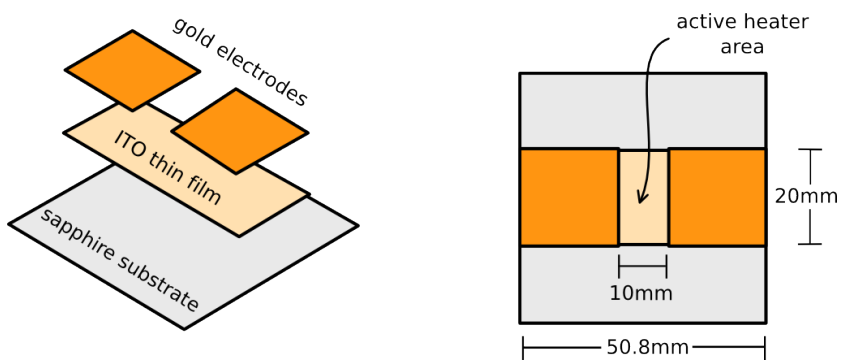

Figure 4-1: Pool Boiling ITO-Sapphire Heater.

4.1.2 Flow Boiling Design

Heaters tested in flow boiling experiments use a 20mm square sapphire substrate 1mm thick. A $<1\mu$m thick, 10mm wide layer of ITO was deposited across the length of the heater and wrapped around the filleted edge of the sapphire 2.5mm onto the back. Gold pads were sputtered onto 2.5mm wide sections of ITO to provide a location for electrical attachment. This created an ITO active heater area 10mm × 20mm with a resistivity of $2.5\frac{\Omega}{cm^2}$. A flow boiling heater diagram with dimensions can be found in Figure 4-2. With the electrodes located on the back of the heater, the ITO can be used as the nano-engineered boiling surface in contact with water. Therefore, the direct signal from the IR camera can be used for data analysis. This configuration also prevents any smearing of the thermal data used to calculate boiling parameters such as nucleation site density and bubble departure frequency. More details on this heater design can be found in the work of Phillips (2014) and Su (2015) [10, 60].

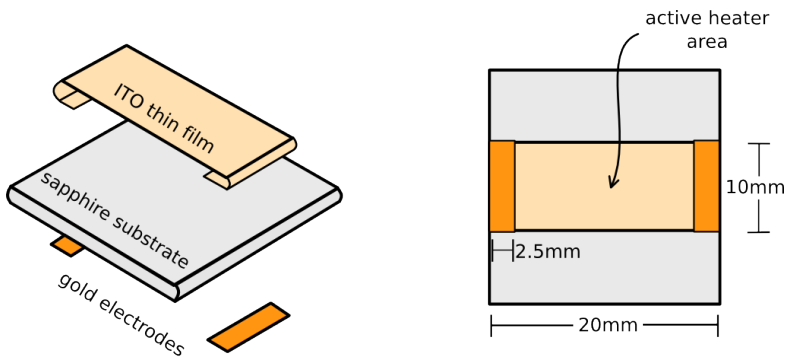

Figure 4-2: Flow Boiling ITO-Sapphire Heater.

4.2 Synthetic CRUD Fabrication

The relevant structures of reactor CRUD to replicate are the porous matrix and chimneys, as described in Section 2.4.1. Several manufacturing methods are combined in series to create this nano-engineered synthetic CRUD with surface parameters matching those of reactor CRUD. Although many fabrication methods were explored, the techniques described below were chosen based on their successful coupling and high reliability in creating desired surface morphology.

4.2.1 Heater Preparation

All heaters are cleaned before any manufacturing begins to ensure better deposition of materials to the substrate as well as increase the repeatability of engineered features. This procedure is especially important given the sapphire is rarely used as a substrate in this methods and can be more difficult to adhere to. First, the heater is rinsed with isopropyl alcohol and deionized (DI) water and dried with compressed air. Next, the heater is cleaned by an oxygen plasma for 2 minutes at 200W under a 500mTorr vacuum. During this process, surface contaminants that affect the contact angle or adhesion properties such as organics are broken down by the ionized oxygen plasma, recombine with oxygen particles, and are removed from the surface. This leaves a clean surface on which to begin manufacturing. In this case, a Glow Research AutoGlow Plasma System in MTL:EML was used, as shown in Figure 4-3.

4.2.2 Photolithography

After the heater surface is cleaned, post features are created on the heater using photolithography. Photolithography is a technique where ultraviolet light is passed through a patterned mask onto a photosensitive resist, creating a three dimensional extrusion of a two dimensional pattern [61]. These cylindrical posts act as place-holders for what will become chimney sites. Photolithography is a well documented method for micro fabrication of molds for lift-off processes [62]. For this procedure, AZ Electronic Material's AZ 4620 photoresist was selected due to its relatively low cross linking, exceptional transparency, high resolution, and large range of applicable

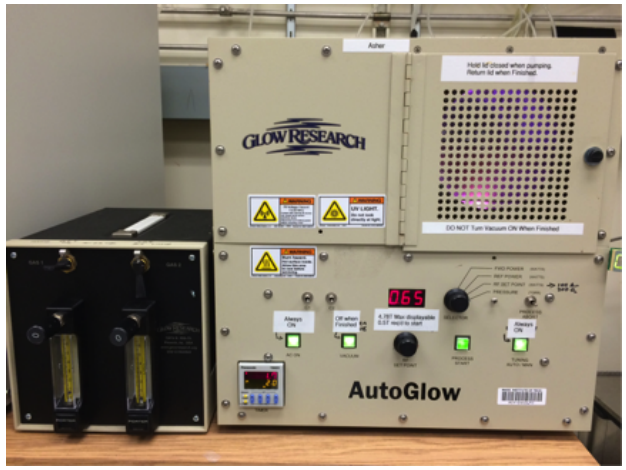

Figure 4-3: Glow Research AutoGlow Plasma System.

thicknesses [63]. These properties create well defined post features that require low temperatures and bake times, making them ideal for later removal to create chimneys. Figure 4-4 illustrates the process flow for AZ 4620 post fabrication and is described in detail below.

First, the substrate is dehydrated and vapor primed with hexamethyldisilazane (HMDS) in a desiccator for ten minutes. The use of HMDS promotes adhesion of the photoresist to the substrate by creating a non-polar, hydrophobic surface [64]. This prevents delamination of the photoresist. Next, the photoresist is deposited onto the substrate by a Solitec Spin Coater (Figure 4-5). During spin coating, photoresist is applied the center of the substrate which sits on a vacuum chuck. Once there is sufficient resist to cover the heater surface, the heater is spun at 500 RPM for five seconds to coat the substrate and then at 5000 RPM for thirty seconds to achieve the desired photoresist thickness. This will also become the post height. The spin speed is selected from data curves where resist thickness is given as a function of spin speed for resists of different viscosities. In this case, the desired thickness is 6μm to accommodate the largest synthetic CRUD thickness in the test matrix.

Next, the substrate is soft baked at 110°C for six minutes in an oven. Due to the relatively large thickness of the sapphire substrate, the oven bake provides more uniform heating to the resist layer. The substrates are placed in the oven on small fins made from aluminum weigh boats as to minimize any conduction heat transfer. Following the oven bake, the photoresist is more highly cross-linked, but most of the water in the photoresist has been evaporated. Water is necessary to break down the photoresist during patterning, so the heater is left in a humidor overnight to rehydrate.

Following rehydration, the heater is placed in contact with a patterned mask and exposed to ultraviolet light. This step transfers the two dimensional mask pattern onto the photoresist. The soda lime glass mask contains circles with the diameter and pitch of the desired chimney features. Figure 4-6 shows the base chimney pattern used in this study, as defined in Table 3.2. AZ 4620 is a positive photoresist, meaning that

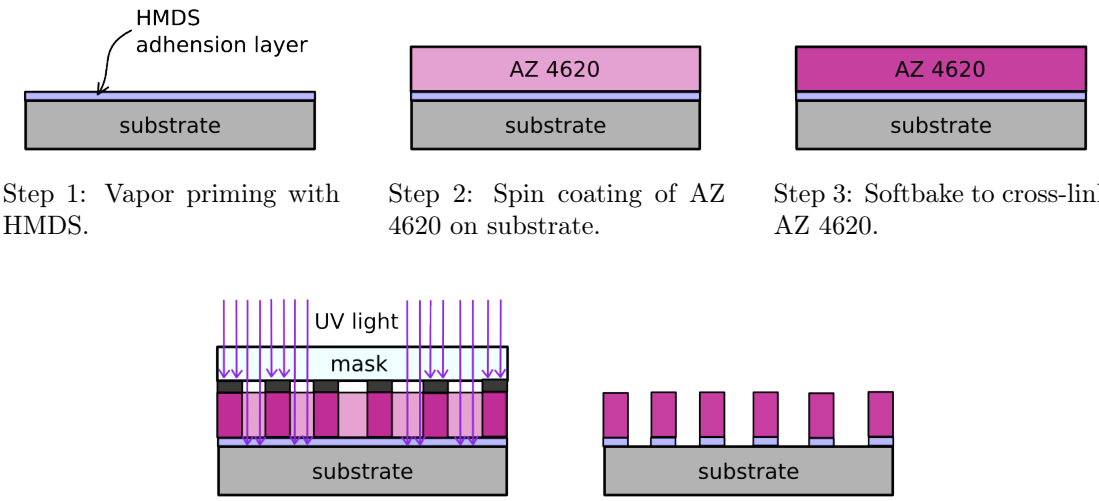

Step 1: Vapor priming with HMDS.

Step 2: Spin coating of AZ 4620 on substrate.

Step 3: Softbake to cross-link AZ 4620.

Step 4: Patterning using chrome mask with UV exposure.

Step 5: Removal of exposed AZ4620.

Figure 4-4: AZ 4620 Photolithography Process.

resist exposed to UV light in the 300nm to 400nm range will be degraded. Therefore, the circles are made of a chrome coating opaque to UV light. The chrome side of the mask is placed in hard contact with the photoresist to reduce any shadowing effects of the exposure. A Karl Suss MA4 mask aligner (Figure 4-5) is used for this process and exposes the substrate at a rate of $10\frac{mW}{cm^2}$. For resist thickness greater than 4μm, an exposure energy of $50\frac{mJ}{cm^2}$ per micron is suggested [63]. Therefore, the substrate is exposed for 30 seconds to achieved the desired $300\frac{mJ}{cm^2}$.

The final step is to remove the exposed resist from the substrate. This is accomplished by submerging the substrate in a beaker of AZ 400K Developer 1:4 under gentle agitation for two to three minutes until all unlinked resist is removed. The remaining posts have the thickness of the initial spin coating and the diameter and pitch of the chrome mask.

The steps described above to manufacture photoresist posts are summarized here:

1. Vapor prime heater with HMDS in desiccator for ten minutes.
2. Deposit AZ 4620 on center of heater.
3. Spin coat heater at 500 RPM for five seconds, then increase to 5000 RPM for thirty seconds.
4. Soft bake heater in oven for six minutes at 110°C.
5. Let heater rehydrate overnight in humidor.

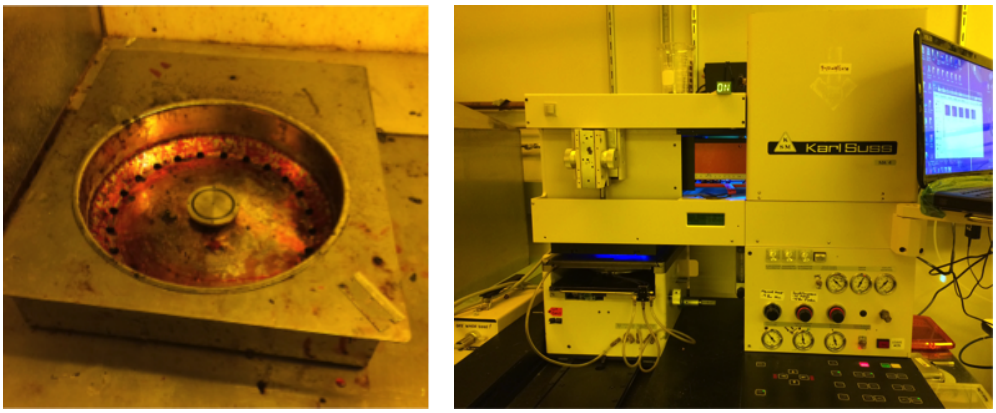

(a) Solitec spin coater. (b) Karl Suss MA4 mask aligner.

Figure 4-5: Photolithography Manufacturing Equipment.

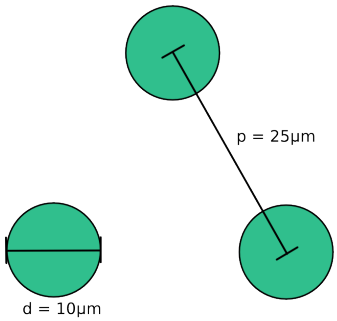

Figure 4-6: 10μm chimney on 25μm pitch mask pattern.

6. Expose heater in mask aligner using hard contact for thirty seconds to achieve exposure energy of $300\frac{mJ}{cm^2}$.

7. Develop heater using AZ 400K Developer 1:4 in beaker under mild agitation for 2-3 minutes

4.2.3 Layer-by-Layer Deposition

The porous matrix is created using a technique called layer-by-layer (LbL) deposition. In this method, thin films are created by alternatingly dipping the substrate in positively (cation) and negatively (anion) charged aqueous solutions [65, 66]. Adhension of the charged particles to the surface is caused by a difference in zeta potential, resulting in diffusion by electrostatic forces. This adhesion of a single layer of positively and negative charged particles creates what is called a bilayer, as shown in Figure 4-7. A coating developed by Professors Michael Rubner in Materials Science and Engineering Department and Robert Cohen in the Chemical Engineering Department at MIT is used in this investigation [67]. While such coatings were developed for anti-fogging, anti-reflection, and self-cleaning applications, they are also able to

survive boiling and can be used for studying the effects of surface characteristics on boiling heat transfer [6, 7, 68].

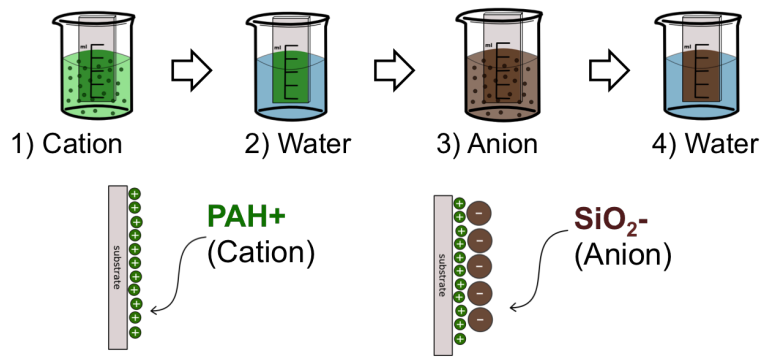

Figure 4-7: Layer-by-Layer (LbL) Deposition of Bilayers.

Intrinsically hydrophilic silica (SiO_2) nanoparticles (Polysciences Silica Microspheres) are used to prepare the anion solution. As discussed in Section 3.1, 100nm SiO_2 nanoparticles were selected to match the porosity and pore size of reactor CRUD. The negatively charged nanoparticles generally arrive in a 5.8wt% concentration, although the exact concentration can vary by lot. These nanoparticles are diluted to 0.03wt% in a one liter pH 9.0 buffer solution. 0.1M NaCl is also added to the solution to promote adhesion of the SiO_2. This buffer solution keeps the pH stable and maintains constant particle zeta potential through the assembly process. While the buffer solution can be made several weeks in advance, the nanoparticles begin to agglomerate and fall out of solution within several days. Therefore, the nanoparticles should be added to the solution the day of use and the solution should not be used for more than two days. The anion solution recipe can be Table 4.1.

Poly(allylamine hydrochloride) (PAH) 120,000-200,000M (40% aqueous solution) (Polysciences) polymer is used to prepare the cation solution. The PAH is diluted to 10^{-2}M in one liter pH 7.5 solution. 1M NaOH is added slowly to the solution until it stabilizes at a pH of 7.5. Due to high polymer stability in solution, PAH solutions are made up to several weeks in advance, though the pH is always confirmed the day of use.

All solutions are mixed for a minimum of one hour before any pH adjustment and then allowed to stabilize for at least a second hour before use. The dipping process is done by a Zeiss HMS Programmable Slide Stainer, as seen in Figure 4-8. The cation and anion solutions are placed in 1.5L bins on the slide stainer with six DI water rinse baths. First, the substrates are dipped in the cation/PAH bath for ten minutes. Then the substrates are rinsed in three DI water baths for two, one, and one minutes. Next, the substrates are submerged in the anion/SiO_2 bath for ten minutes and again rinsed with the same procedure. The substrates are immersed in the cation and anion baths for longer times to ensure complete diffusion of charged particles onto the surface. The rinsing process ensures the monolayer adhesion by each bilayer and prevents contamination between the cation and anion baths. This process is illustrated in

Table 4.1: Anion Solution for Layer-by-Layer Assembly: 0.03wt% SiO_2 nanoparticles at pH 9.0.

Component	*Quantity*	*Purpose*
DI H_20	1L	Dilution
SiO_2 nanoparticles	Quantity required for 0.03wt%	Source of nanoparticles
Boric acid	3.1 g/L	pH 9.0 buffer
KCl	3.7 g/L	pH 9.0 buffer
NaOH	0.86 g/L	pH 9.0 buffer
NaCl	5.845 g/L	Aids absorption

Table 4.2: Cation Solution for Layer-by-Layer Assembly: 10^{-2}M PAH at pH 7.5.

Component	*Quantity*	*Purpose*
DI H_20	1L	Dilution
PAH polymer	2.3425 g/L	Source of polymer
1M NaOH	Quantity required for pH of 7.5	pH adjustment

Figure 4-9. Immediately after dipping, the surface is superhydrophilic (contact angle <5°).

Figure 4-8: Zeiss HMS Programmable Slide Stainer.

Thicker films are achieved by the deposition of more bilayers. The average thickness per bilayer of an LbL assembly is affected by nanoparticle size and zeta potential of solution. Due to the negligible thickness of the PAH polymer, it is not considered to add to each bilayer thickness. Therefore, the number of bilayers required to obtain desired thickness was experimentally determined. Layer-by-layer solutions using spherical nanoparticles pack loosely with porosity values generally between 50-60%

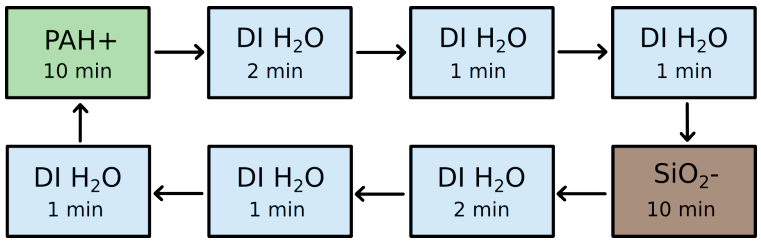

Figure 4-9: Layer-by-Layer Deposition Process.

Table 4.3: Anion Solution for Layer-by-Layer Assembly: 0.03wt% Fe_3O_4 nanoparticles at pH 4.0.

Component	*Quantity*	*Purpose*
DI H_20	1L	Dilution
Fe_3O_4 nanoparticles	Quantity required for 0.03wt%	Source of nanoparticles
1M HCl	Quantity required for pH of 4.0	pH adjustment

over a wide range of nanoparticles sizes. However, the pore size of the film is affected by and on the order of to the particle size. The porosity and pore size of this 100nm SiO_2/PAH LbL assembly was measured by *Tetreault-Friend (2014)* [6] and found to be 65% and 100nm, respectively. LbL deposition generally creates thin films with roughness on the order of the particle size. However, with the large nanoparticles used here in creating films several microns thick, the roughness can become up to an order of magnitude greater than the particle size.

The same procedure as above was conducted for 10nm Si_2 and Fe_3O_4 pool boiling comparison tests. The above PAH recipe was used for both 10nm LbL assemblies. The Si_2 recipe found in Table 4.1 was used with 10nm particles rather than 100nm particles. The 10nm Fe_3O_4 nanoparticles (Ferrotec Ferrofluid) used were purchased in 17wt% concentration. The recipe can be found in Table 4.3.

4.2.4 Post Removal

The posts are removed by acetone chemical dissolution. The heaters are first submerged in acetone between 50-55°C for 20 minutes. Next, they are sonicated in acetone for 90 second intervals until all posts are removed, as confirmed by a microscope.

4.2.5 Autoclaving

While the as made LbL coating is robust enough to survive boiling, high temperature baking of the surface can be done to further increase mechanical durability of the coating and remove some of the PAH polymer. Normally, this calcination would be done at 550°C for several hours. This causes minor sintering of the particles, increasing the strength of the matrix and also removing polymer that may increase the film contact angle. However, there are times when calcination is not possible

due to substrate limitations. In this case, the ITO undergoes a phase change around 200°C. Therefore, a lower temperature option must be considered.

Figure 4-10: Tuttnauer-Brinkmann 2340M Autoclave.

Professors Rubner and Cohen found that autoclaving LbL films at high pressure and low temperature was effective in increasing mechanical durability [69]. After the post removal process, the heaters are hydrothermally treated with saturated steam for one hour at 124°C in a Tuttnauer-Brinkmann 2340M autoclave, shown in Figure 4-10. The hydrothermal treatment enhances the durability without greatly increasing particle necking and decreasing the porosity, as shown in Figure 4-11

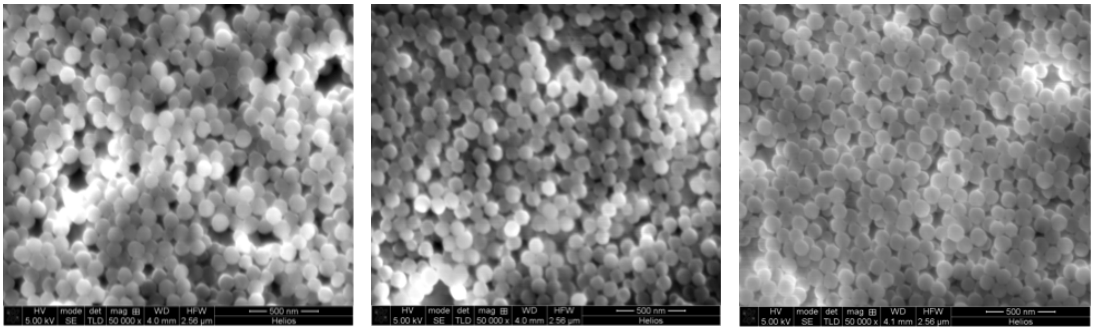

(a) Without treatment. (b) 30 min autoclaved. (c) 60 minutes autoclaved.

Figure 4-11: 100nm SiO_2 LbL Films Before and After Autoclaving.

This process results in a porous matrix of desired thickness, porosity, and pore size with hexagonally spaced chimneys of a specified diameter and pitch. By creating synthetic CRUD in this way, every aspect of the surface can be precisely controlled.

4.3 Feature Verification

Feature verification is an important part of the manufacturing process used to ensure synthetic CRUD is representative of reactor CRUD. Several techniques are used to

confirm surface parameters of interest, specifically thickness, roughness, wettability, porosity, pore size, and chimney pitch and diameter. These verification methods can be both destructive and non-destructive. Destructive methods are used on representative sample coatings to confirm parameters that are consistent across the manufacturing process. Non-destructive methods are used on each heater throughout synthetic CRUD fabrication to ensure coatings have the desired surface characteristics.

4.3.1 Stylus Contact Profilometer

The Dektak 150 Surface Profilometer in MIT's MTL:EML is used to measure the pitch and diameter of photolithography posts as well as thickness and roughness of LbL films. The contact profilometer moves a 12.5μm radius stylus across the surface with a force of 1 mg. The stylus follows the vertical topography, which is read by the Dektak software. It obtains a 2.5mm linear height profile of the surface with a vertical resolution of about 1 angstrom [70]. A representative data scan is shown in Figure 4-12. Using these scans, features heights as well as roughness values can be calculated. To obtain a level surface baseline for the post heights (the stylus radius is on the order of the post spacing) and LbL thickness, a small scratch in made in the coating off the active heater area. Thicknesses are recorded as the difference between this baseline and the feature heights. The surface roughness R_a, or the average of the absolute values of feature heights, of the LbL is also recorded. A minimum of four scans was conducted in different locations on each heater to accurately report height and roughness values.

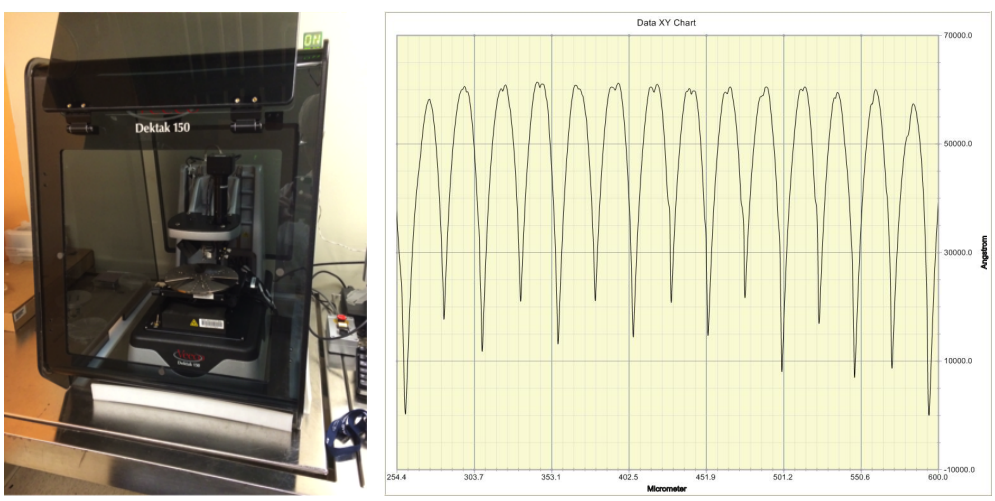

(a) Profilometer Image. (b) 10μm diameter on 25μm pitch posts data scan.

Figure 4-12: Dektak 150 Surface Profilometer.

4.3.2 Contact Angle Measurement

A KSV Instruments CAM 101 Goniometer in MIT's Reactor Thermal Hydraulics Laboratory quantifies the wettability of the surface by measuring the contact angle. The sample in placed on a stage and backlit while CCD camera video is collected by an imaging software. The camera records video as a single water droplet is put in contact with the surface using a syringe. The static contact angle of the surface is defined as the angle made by the water droplet 0.5 seconds after first touching the surface. The imaging software is used to measure the contact angle on the left and right side of the droplet. The average value is recorded as the static contact angle of the surface, as shown in Figure 4-13. Three static contact angle measurements were taken for each heater. Due to the high capillary wicking of the porous layer, advancing and receding contact angle measurements could not be made. The contact angle was measured directly before and after testing to confirm the wettability of the heater was unchanged.

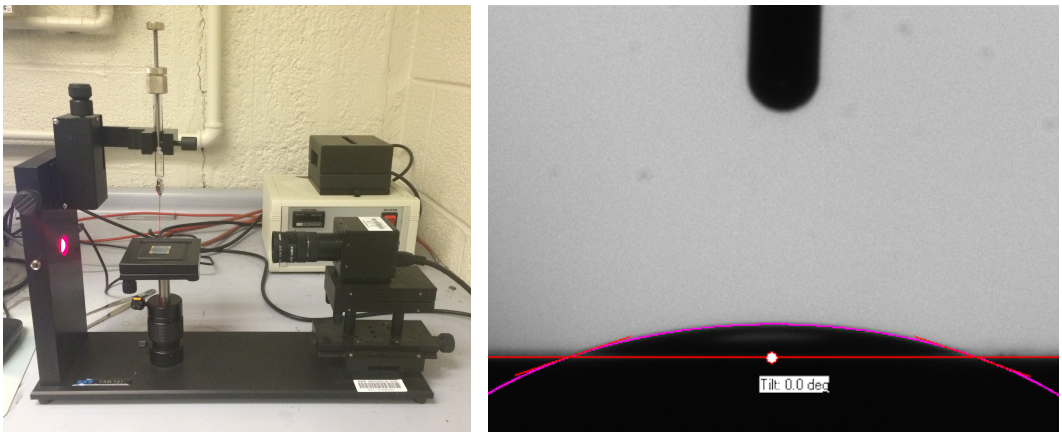

(a) Goniometer Image. (b) Contact angle measurement.

Figure 4-13: KSV Instruments CAM 101 Goniometer.

4.3.3 Duel Beam Focused Ion Beam/Scanning Electron Microscope (FIB/SEM)

The Helios Nanolab 600 Dual Beam Focused Ion Beam Milling System (Figure 4-14) in MIT's Center for Materials Science and Engineering (CMSE) Shared Experimental Facility is used to acquire high resolution images of nano-engineered surfaces. This machine consists of both a scanning electron microscope (SEM) and focused ion beam (FIB) with an optical resolution of <2.5nm at 1kV. The SEM function uses a beam of electrons which pass current through the coating to gather images of the surface topography. A thin (<10nm) carbon coating is applied to the layer before viewing to carry the current because the silica nanoparticles are non-conductive. The FIB function uses an ion beam to mill small cross sections into the coating. Cross sectional images are used to ensure uniformity through the layer and also quantify average

pore size. *Tetreault-Friend (2014)* used the FIB functionality to confirm 100nm silica particles create a pore size of roughly 100nm.

(a) Duel Beam FIB/SEM.

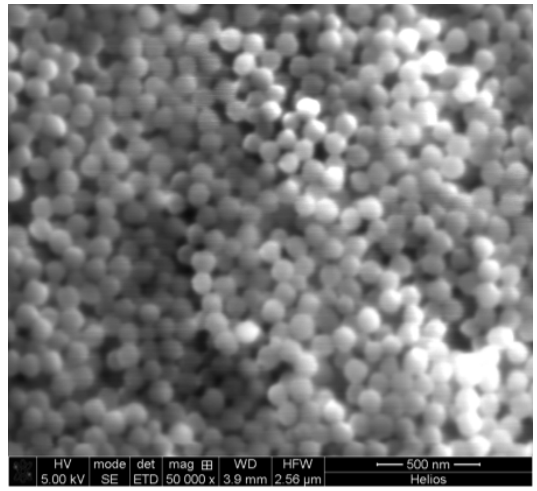

(b) SEM high resolution surface image.

Figure 4-14: Helios Nanolab 600 Dual Beam Focused Ion Beam Milling System.

4.3.4 Spectroscopic Ellipsometer

A J.A. Woollam Co., INC model XLS-100 Ellipsometer (Figure 4-15) in MIT's Institute for Soldier Nanotechnologies (ISN) is used to take porosity measurements of the LbL surfaces. Ellipsometry calculates the thickness of thin films using their index of refraction. Incident light with known properties interacts with the surface and, based on its change in polarization, information such as thickness and porosity can be measured. In this application, the coating is submerged in both air and DI water and, based on the change of the index of refraction, the volume of the pores can be calculated according to equation 4.1 [6].

$$p = \frac{n_2 - n_1}{n_{water} - n_{air}} \tag{4.1}$$

n_2 and n_1 are the measured refractive indices of the film submerged in water and air and n_{water} and n_{air} are the reactive indices of water and air. *Tetreault-Friend (2014)* measured the porosity of 100nm silica coatings deposited by LbL as 60-65%.

4.4 Heater Testing and Facilities

4.4.1 Heater Preparation

Prior to testing, the pool and flow boiling heaters must be prepared and installed in their respective testing cartridges. The back side of the heater is cleaned using isopropyl alcohol and DI water on a cotton swab. This creates an unobstructed surface

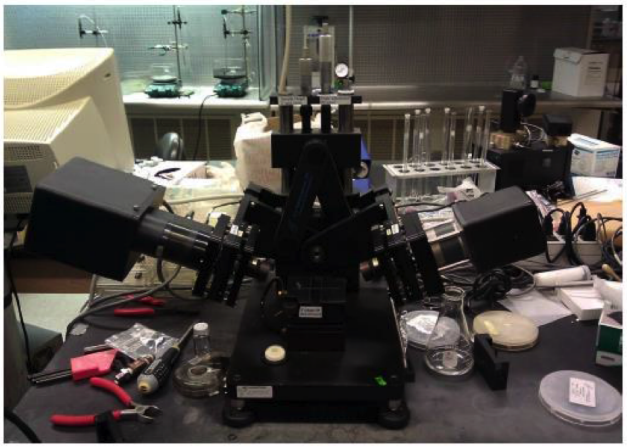

Figure 4-15: J.A. Woollam Co., INC model XLS-100 Spectroscopic Ellipsometer [6].

for IR imaging. Conductive silver epoxy is used to create an electrical connection to the heater gold pads. Leads are attached to the pool boiling heaters while the flow boiling heaters are epoxied into a cartridge that uses graphite pieces as the electrodes.

As discussed in Section 4.3.2, the contact angle of the surface is a parameter of interest. The surface is superhydrophilic directly after the LbL process. However, as the coating is exposed to air between the completion of the LbL and testing, organic materials can be absorbed into the porous coating and raise the contact angle. Therefore, the contact angle of the surface is measured the day of testing and, if it has increased, the surface is cleaned using ultraviolet ozone cleaning.

Similar to plasma cleaning, ultraviolet ozone cleaning is used to clean substrates. UVOzone cleaning is preferable after the heaters have been installed because this process takes place at atmospheric pressure and is not reactive withe the silver epoxy. In this process, 253.7nm wavelength UV light breaks down ozone by photodisassocaition while 184.9nm wavelength UV light is emitted to break down oxygen into atomic oxygen. This atomic oxygen then reacts with organic materials to remove them from the surface. Here, a UVOCS T10X10/OES ultraviolet cleaning system (Figure 4-16) is used to remove organic material and reduce the contact angle to 15-20° before testing.

4.4.2 Pool Boiling Facility

The pool boiling facility (PBF) in MIT's Reactor Thermal Hydraulics Laboratory has been used extensively to study the effects of surface coatings on boiling heat transfer [6, 7]. The pool boiling facility is composed of an aluminum outer isothermal water bath and an inner DI water bath where heater testing is conducted. A borosilicate tube creates the inner bath and attaches to the heater substrate using silicone sealant to form a water tight seal. This isolates the heater from the rest of the bath and keeps the boiling surface clear of contaminants. This tube is then placed in the outer bath over a square opening using a silicone gel gasket. Leads are fed through the opening and connected to a Electronic Measurements Inc. TCR DC Power Supply

Figure 4-16: UVOCS T10X10/OES.

and an Agilent Technologies 34980A Data Acquisition System (DAS). The power supply provides the power to the heater while the DAS reads the outputs of the power supply and calculates the heat flux, q'', provided to the heater according to equation 4.2,

$$q'' = \frac{P}{A_{active}} = \frac{V \times I}{A_{active}} \tag{4.2}$$

where P is power, V is voltage, I is current, and A_{active} is the active heater area. The DAS also reads the temperature output of a K-type thermocouple in the outer bath. A 1500W cartridge heater is used to bring the water to saturation temperature.

The opening in the bottom of the outer bath also allows the heater to be imaged from the bottom using a FLIR SC6000 IR camera with 100mm lens and 3/4" extension ring. A 45° angle gold mirror is placed directly beneath the heater while the IR camera captures video at 1000Hz for two seconds safety next to the pool boiling facility. Figure 4-17 shows the pool boiling facility layout. The IR camera records the temperature of the ITO surface because ITO is IR opaque. In order to calculate the temperature of the heater surface, heat conduction through the sapphire (flat plate model) must be accounted for, as shown in equation 4.3.

$$T_{surface} = T_{ITO} - q'' \times R_{sapphire} = T_{ITO} - q'' \times \frac{t_{sapphire}}{k_{sapphire}} \tag{4.3}$$

$T_{surface}$ is the heater surface temperature, T_{ITO} is the ITO temperature, $R_{sapphire}$ is the sapphire resistance, $t_{sapphire}$ is the sapphire thickness, and $k_{sapphire}$ is the sapphire thermal conductivity. IR video is taken at increasing heat flux until the heater reaches CHF and fails. Therefore, each heater can only be tested once. The camera calibration procedure is explained in Section 4.5.1.

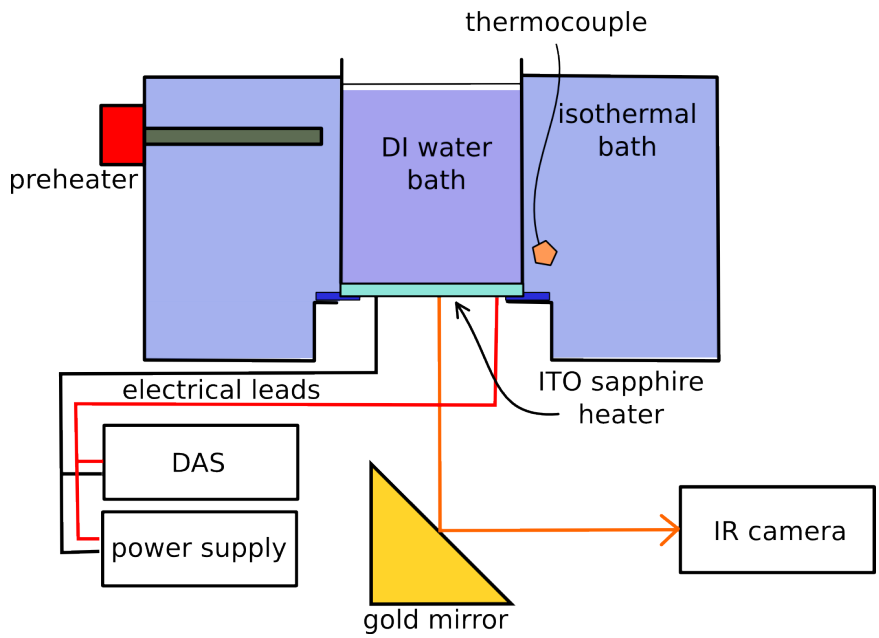

Figure 4-17: Pool Boiling Facility Schematic.

4.4.3 Flow Boiling Loop

The flow boiling loop (FBL) in MIT's Reactor Thermal Hydraulics Laboratory has also been used previously to study boiling parameters of ITO sapphire heaters [10]. The flow boiling loop is composed of 304 and 316 stainless steel and contains a variable speed pump, a turbine flow meter, a preheater, a heat exchanger, and resistance temperature detectors (RTD) and pressure transducers. Figure 4-18 shows a schematic of the flow boiling loop. Using these components, water subcooling and mass flux can be precisely controlled while monitoring temperatures and pressures at the inlet and outlet of the test section.

Phillips (2014) designed a custom test section and heater cartridge that placed the flow boiling heater heater flush with fully developed flow through the test section and allowed it to be imaged with both IR and HSV cameras. The test section is made of quartz and the heater cartridge is made of graphite electrodes with a Macor® insulator, as shown in Figure 4-19.

After the heater has been installed in the cartridge recess, the cartridge is inserted into the test section and sealed with a compressed O-ring. Wires are attached to the graphite electrodes and connected to a Agilent Technologies N5769A Power Supply and an Agilent Technologies 34980A Data Acquisition System (DAS). Similar to the pool boiling facility, the power supply provides power to the heater while the DAS measures the output from the power supply and calculates the heat flux as well as monitoring loop variables such as temperature, pressure, and mass flux. The loop was filled by first pulling a 20 psi vacuum and then opening it to the 5 psi pressured DI water fill tank. The pump was then started and then switch between high and low power to dislodge and vent any remaining non-condensable gases. The 2000W preheater was then started to raise the water temperature to the desired subcooling.

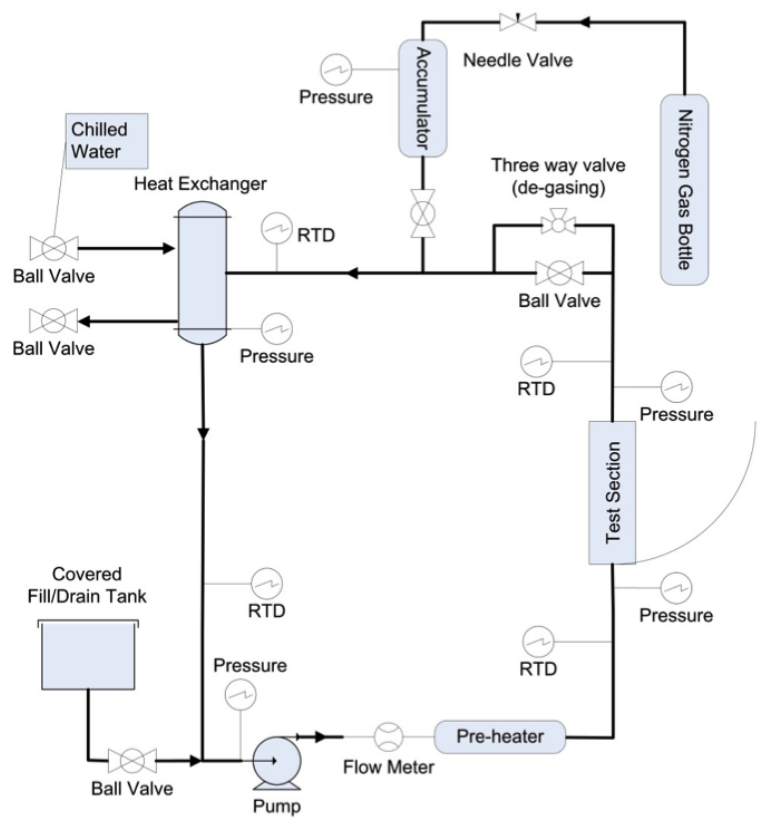

Figure 4-18: Flow Boiling Loop Schematic [10].

A FLIR SC6000 IR camera with 50mm lens and 3/4" extension ring is used to image the ITO 2D temperature profile from behind the heater at 1000Hz with a 0.25ms integration time. In this instance, because the ITO is the boiling surface, no temperature correction needs to be done. Simultaneous, a Phantom V12 HSV camera with Nikon 200mm lens with 68mm of extension rings was used to capture high speed video data at 4000Hz from the side of the heater (90° off from the IR camera). This setup is shown in Figure 4-20. The camera image collection was synced by using the "SYNC OUT" output from the IR camera to trigger the HSV camera. HSV was collected at a frequency that is a multiple of the IR frequency so they could be synchronized. The FLIR and HSV cameras have resolutions of 65μm per pixel and 16.5μm per pixel, respectively. A blackbody was used to perform a two point non-uniformity correction to account for non-uniform response of pixels in the IR camera. The mass flux was set by the pump power and both mass flux and subcooling were allowed to stabilize for five minutes before collecting data at the heat fluxes listed in Table 3.3.

More detailed information about the flow boiling loop and test section design and construction can be found in *Phillips (2014)* [10].

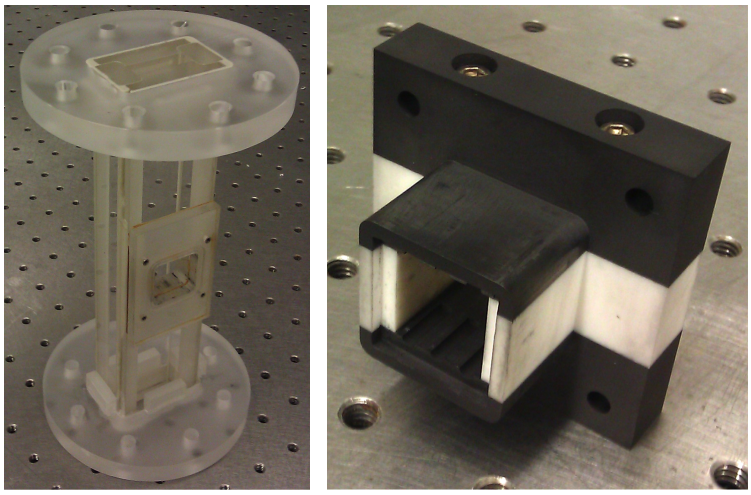

(a) Test Section. (b) Heater Cartridge.

Figure 4-19: Images of flow boiling loop test section components [10].

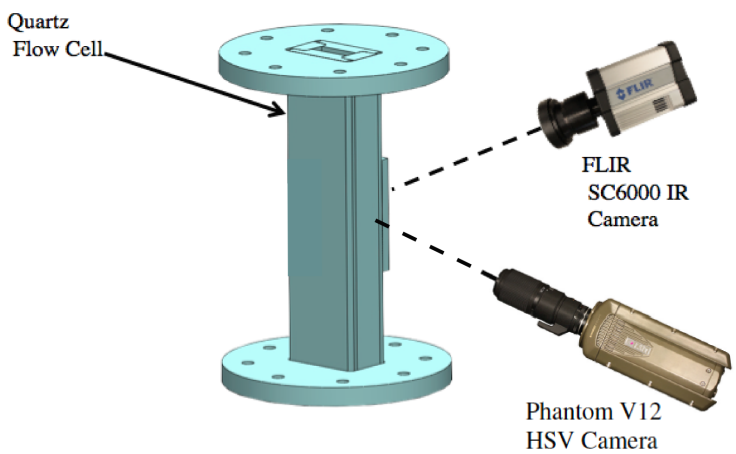

Figure 4-20: Test Section and Camera Setup Schematic [10].

4.5 Data Reduction

This section explains the data reduction process and measurement and value uncertainties. These methods have been used previously in MIT's Reactor Thermal Hydraulics Laboratory. More information about their development and rationale can be found in *Phillips (2014)* [10].

4.5.1 Calibration

Calibrations must be done to correctly convert counts data from the IR camera to temperature. First, a dry calibration is conducted. A thermocouple is placed on the ITO surface and IR video and temperature are measured and recorded simultaneously at increasing power. This data creates a counts to temperature conversion curve.

Then, each individual heater undergoes a wet calibration once it is installed where the temperature is measured every 2 degrees, either by a thermocouple for the PBF or by RTDs for the FBL, between 86 and 98°C. There is a slight shift in the dry and wet calibration curves due to do small variations in the experimental setup from day to day. Therefore, the dry calibration is shifted to match the wet calibration and the temperature data is calculated from the new curve, as shown in Figure 4-21.

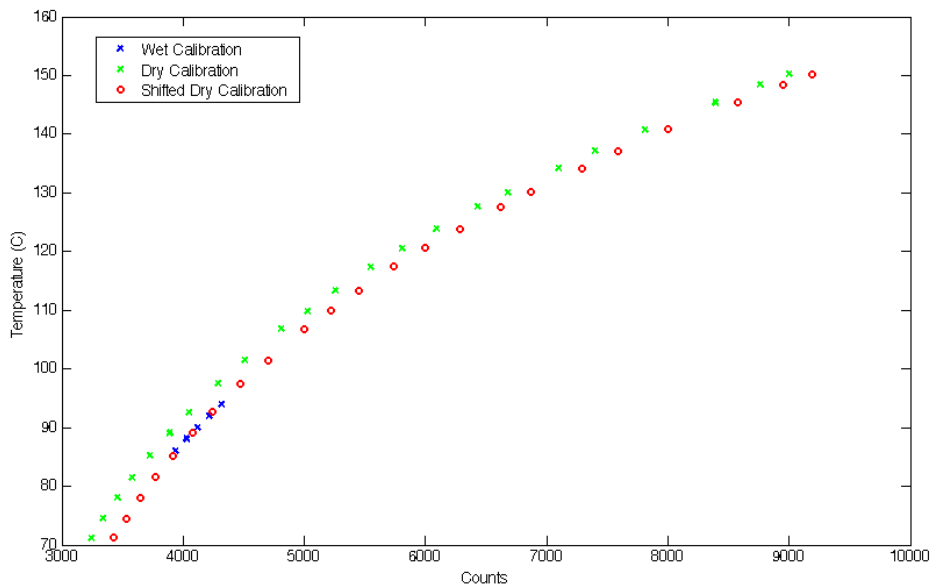

Figure 4-21: Wet and Dry Calibration Curves.

4.5.2 IR Imaging Analysis

A Matlab script developed by *Phillips (2014)* was used for IR imaging analysis. This script is used to gather average surface temperature information to calculate the HTC, as well as nucleation site density and bubble departure frequency. Only HTC is calculated for pool boiling heaters while flow boiling heaters quantify all three. The Matlab script imports the IR video as 2000 frames in Flexible Image Transport System (FITS) format and determine the average number of counts both spatially and temporally. This results in an average number of counts for the video. The shifted dry calibration then converts counts to temperature. The HTC is defined by heat flux and temperature different from the wall to the bulk fluid, as shown in equation 4.4.

$$h = \frac{q''}{T_{wall} - T_{bulk}} \tag{4.4}$$

Nucleation site density is calculated by finding the average value of each pixel over time and then looking for deviations from that average value. Deviations from the average value signal nucleation sites while a cutoff value is applied to ensure deviation

is representative of a true nucleation site. Exclusions zones around nucleation sites are also defined to ensure each site is unique to prevent double counting. Counting is cutoff at 2100 sites/cm^2 so the exclusion zone does not effect nucleation site density results.

Bubble departure frequency is calculated by tracking each nucleation site found using the previous algorithm and then tracking the variation of the nucleation site between a high and low number of counts. The number of variations per second is the bubble departure frequency. This value is averaged over all nucleation sites.

4.5.3 HSV Imaging Analysis

High speed video is used to determine the bubble departure diameter, defined as the vertical length of the bubble when it lifts off from the surface. Diameters were measured for heat fluxes in the nucleate boiling regime where individual bubbles could be identified. Only bubbles that were formed and nucleated from the surface without sliding or any other bubble interaction (i.e. no bubble coalescence or bubbles passing another bubble) were considered.

4.5.4 Uncertainty Analysis

Phillips (2014) characterized the uncertainty of the flow loop, IR and HSV cameras, and computed values. This section will briefly address that analysis. For further information about the derivation of the measurement uncertainties, refer to Phillips (2014) [10].

Surface Temperature

The surface temperature uncertainty is limited mainly by the insitu calibration. The IR camera has a temperature uncertainty of <0.1°C; however, the Omega K-type thermocouple has an accuracy of 1.1 °C. Combined with the error in the polynomial fit calibration curve, the surface temperature uncertainty is 2.0°C.

Heat Flux

The heat flux is calculated using the voltage and current values from the power supply and the heater area. The errors in these values are 0.005V, 0.005A and 2.7%, respectively. Propagating these three errors leads to a total uncertainty in the heat flux of 2.8%.

Heat Transfer Coefficient

The heat transfer coefficient uncertainty is derived from the heat flux, inlet temperature, and surface temperature uncertainties. Propagating the inlet and surface temperature uncertainties leads to an uncertainty in ΔT of 2.24%. Combining this

with the 2.8% heat flux uncertainty leads to an average heat transfer coefficient uncertainty of 11.5% (for $\Delta T = 20°C$). Specific uncertainty values for each data point are shown in the heat transfer coefficient plots.

Nucleation Site Density

Uncertainty in the nucleation site density comes for selection criteria in the automated Matlab algorithm, such as signal cutoff value, convergence criteria, and maximum site size. The IR camera resolution also determines the maximum number of sites that can be uniquely counted before sites begin to interact. The FLIR IR camera has a spatial resolution of roughly 60μm, which limits the nucleation site density to 1100 sites/cm^2. Phillips (2014) found the Matlab algorithm to be within 15% of hand counting values. A 15% error in nucleation site density is also used here.

Bubble Departure Frequency

Similar to the nucleation site density, uncertainty in the bubble departure frequency comes from the user input selection criteria. *Phillips (2014)* reports the uncertainty between the automated Matlab algorithm and hand counting of the bubble departure frequency as 17%. However, the bubble departure frequency standard deviation is larger than this error, so the standard deviation is given as the error bar values.

Bubble Departure Diameter

The bubble departure diameter uncertainty is a function of the spatial resolution of the HSV camera and the pixels used to define the bubbles edges. Based on the camera alignment and spatial resolution, the error in the camera is 0.1% where as the error in pixel selection can be as large as 7.5%. However, the distribution in bubble diameter is significantly larger than this uncertainty. Therefore, the standard deviation of the bubble diameters is used as the error bars in the bubble departure diameter plots.

4.5.5 Repeatability

The repeatability of tests was investigated to ensure the accuracy of the results. Two, different bare heaters and two, different 2μm thick, no chimneys heaters were tested in flow boiling. The results had very strong agreement between trials. As such, the remainder of the test matrix was run with one heater per case. The heater was tested through the entire conditions test matrix, at the end of which, a minimum of four points from the beginning of the test were retaken. The data was compared to the first data point to ensure the heater performance remained constant throughout the test. All tests showed good agreement between these beginning and end comparison data points.

5 Pool and Flow Boiling IR/HSV Results

In this chapter, the results of pool and flow boiling tests are presented. Surface feature values are reported for each coating. IR and HSV results are analyzed and used to determine the heat transfer coefficient, nucleation site density, bubble departure frequency, and bubble departure diameter of each surface. Data from an uncoated heater is also presented and used as a baseline. Uncertainty estimates were discussed in Section 4.5.4.

5.1 SEM/FIB Images

The nanoparticle coatings were examined in a SEM/FIB to confirm surface morphology, structure of the porous coating, and average pore size. Figure 5-1 shows images of the 10nm Fe_3O_4 coating with chimneys. Since the particle size is near the SEM resolution, it is not possible to obtain clear images of individual particles or measure pore sizes. The Fe_3O_4 nanoparticles are easier to visualize than the SiO_2 particles because they are inherently conductive. However, the carbon coating, because its thickness on the order of the pore size, gives the particles a textured appearance.

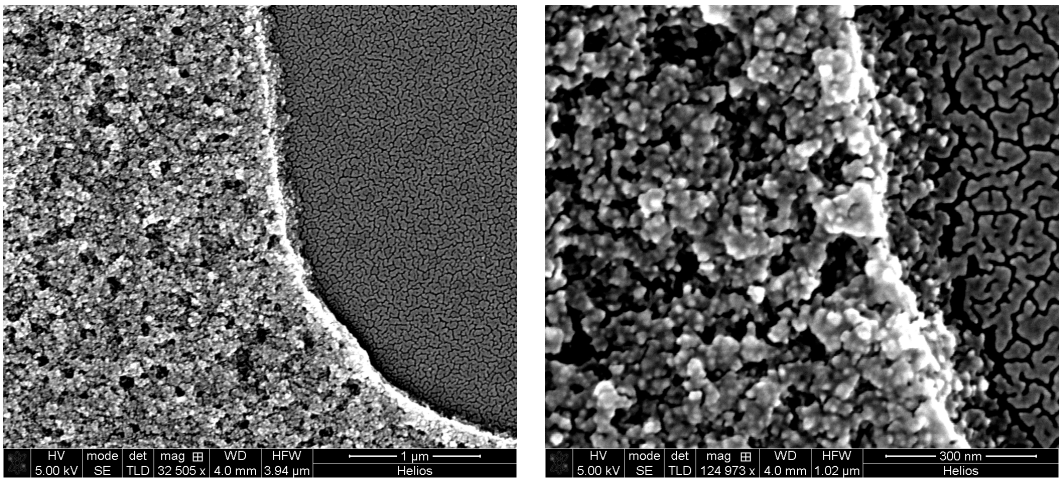

Figure 5-1: 10nm Fe_3O_4 coating with chimneys (low and high magnification).

Figure 5-2 shows images of the 100nm SiO_2 nanoparticle coatings created by

LbL deposition. Due to the larger particle size, individual particles can be seen. The voids are approximately the size of the nanoparticles with some larger voids approximately twice the particle diameter. The porosity of the 100nm particles (60-65%) is also greater than that of the 10nm particles (40-45%). LbL deposition porosity and roughness increase with larger particle sizes due to greater non-uniformity in the layer assembly.

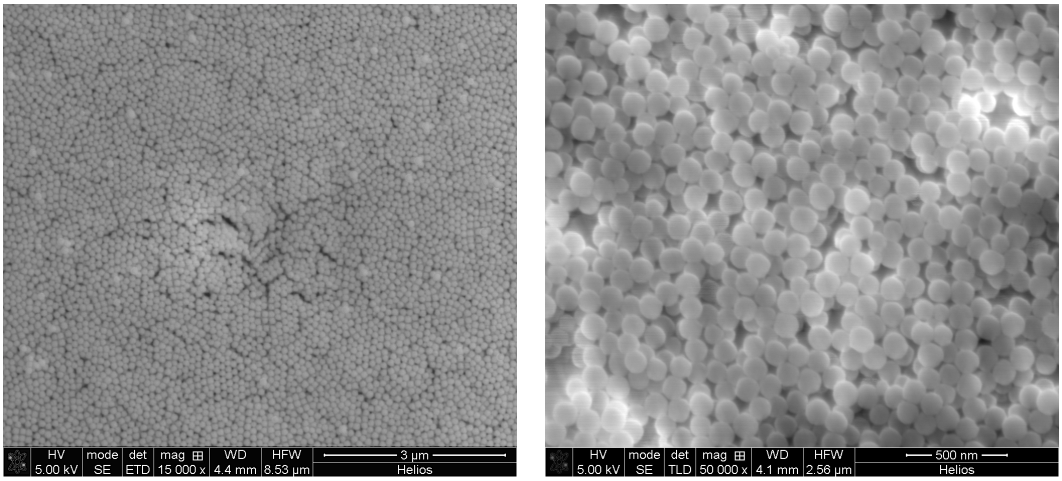

Figure 5-2: 100nm SiO_2 coating (low and high magnification).

Figure 5-3 shows the 100nm SiO_2 nanoparticle coating with interspersed chimneys. These images are of the base case surface coating. The porous matrix is the same as that in Figure 5-2. The ITO heater surface can be seen at the bottom of the chimneys.

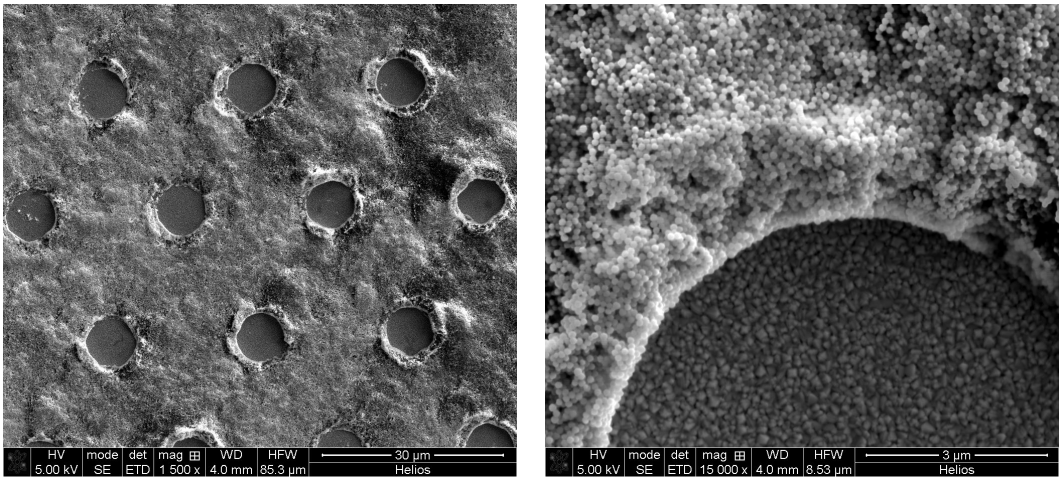

Figure 5-3: 100nm SiO_2 coating with 10μm chimneys on a 25μm pitch (low and high magnification).

5.2 Pool Boiling

5.2.1 Surface Analysis

Pool Boiling tests were run using SiO_2 and Fe_3O_4 nanoparticles to compare their performance, as discussed in Section 3.3.1. Heaters were fabricated with 2μm layers both with and without chimneys as defined in Table 3.5. The surface wettability was measured using a contact goniometer and the thickness and roughness were measured using a stylus contact profilometer. All surfaces tested in pool boiling were made with 10nm particles. Therefore, the average pore size and porosity of the layers are 10nm and 42%, respectively, as measured by *Tetreault-Friend (2014)*. The static contact angle, thickness, and roughness of the layers were measured and are shown in Table 5.1. For these and all following coatings, a minimum of four thickness and roughness measurements were taken as well as at least three contact angle measurements.

Table 5.1: Pool boiling heaters surface analysis data. Standard deviation values are in parentheses.

Case	*Sample Description*	*Number of Bilayers*	*Contact Angle(°)*	*Thickness (μm)*	*Roughness, R_a (nm)*
1	Fe_3O_4, no chimneys	35	21.2 (9.5%)	2.1(19.7%)	39(2.3%)
2	Fe_3O_4, 10_25		In progress		
3	SiO_2, no chimneys	85	17.1 (10.6%)	1.87(5.4%)	65.8(36.7%)
4	SiO_2, 10_25	85	15.4 (11.0%)	2.1 (5.0%)	74.5 (28.4%)

5.2.2 IR Results

Table 5.2 gives the CHF values of the SiO_2 and Fe_3O_4 nanoparticle coatings, both with and without chimneys. Figure 5-4 shows a representative boiling and heat transfer coefficient curve for one of those heater coatings.

5.2.3 Discussion

The boiling curves of the 10nm Fe_3O_4 and SiO_2 without chimneys are very similar, especially at low heat fluxes. This demonstrates that SiO_2 is an acceptable substitute for Fe_3O_4 and that the boiling behavior is affected more significantly by the surface morphology than surface composition. The addition of chimneys increases the HTC over a purely porous surface by roughly 25%. This enhancement is hypothesized to be a result of better vapor escape from the surface through the chimney. However, all coatings have a lower HTC than a bare heater where there is no added thermal resistance or barrier for vapor escape. The CHF of the coated surfaes is significantly higher than that of the bare heater.

Table 5.2: Pool boiling heaters CHF values. *Data from *O'Hanley et al.* [7].

Case	*Sample Description*	*Number*	*CHF* ($\frac{kW}{m^2}$)	*Average CHF* ($\frac{kW}{m^2}$)
0*	uncoated	1 2	920 986	953
1	Fe_3O_4, no chimneys	1 2	1630	1630
2	Fe_3O_4, 10_25	1 2	In progress	
3	SiO_2, no chimneys	1 2	1645 1790	1717
4	SiO_2, 10_25	1 2	1762 2000	1881

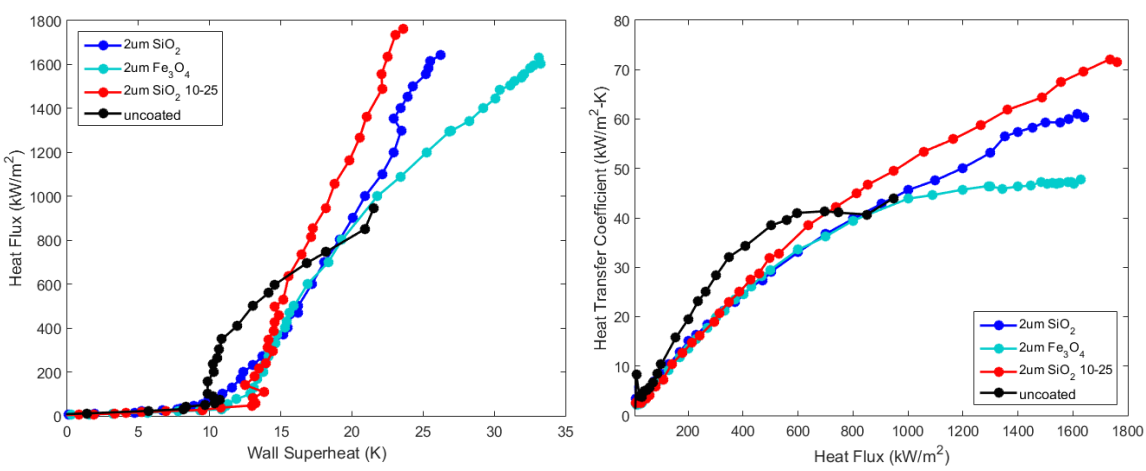

(a) Boiling Curve (b) Heat Transfer Coefficient Curve

Figure 5-4: Pool boiling for uncoated [7] and 10nm, 2μm Fe_3O_4 and SiO_2 coatings with 10μm chimneys on a 25μm pitch and without chimneys. Maximum uncertainties are T= 2°C, q" = 2% , and HTC = 11%.

5.3 Flow Boiling Test Matrix

Table 5.3 shows the full investigation test matrix and gives the progress of each case. The remainder of this chapter will present and discuss the flow boiling results for completed tests.

Table 5.3: Flow boiling synthetic CRUD test matrix.

	Case	*Thickness(μm)*	*Diameter(μm)*	*Pitch(μm)*	*Status*
Effect of chimneys	1	2	no chimneys	no chimneys	Complete
	2	2	10	25	Complete
Effect of thickness	2	2	10	25	Complete
	3	4	10	25	Complete
	4	6	10	25	In progress
Effect of pitch	2	2	10	25	Complete
	5	2	10	35	In progress
	6	2	10	45	Complete
Effect of diameter	2	2	10	25	Complete
	7	2	12.5	27.5	Complete
	8	2	15	30	In progress

5.4 Case 0: Uncoated Heater

5.4.1 Surface Analysis

An uncoated heater was tested and used as a baseline to determine the effects of surface coatings on boiling heat transfer properties. The uncoated heaters were used with the as received ITO as the boiling surface. The surface properties of the ITO are listed in Table 5.4.

Table 5.4: Uncoated heater surface analysis data.

Number of Bilayers	*Contact Angle(°)*	*St. Dev.*	*Thickness (μm)*	*St. Dev.*	*Roughness, R_a (nm)*	*St. Dev.*
0	95.0	5.2%	0	0%	2.25	13.8%

5.4.2 IR/HSV Results

This section shows the results for the uncoated heater flow boiling test and the data follow expected trends from developed models. Figure 5-5 shows the boiling and heat transfer coefficient curves for an uncoated heater. The boiling curves confirm the initial, linear single phase heat transfer region, following by the nucleate boiling

region. The wall superheat and HTC increase with increasing heat flux. As the mass flux increases, the wall superheat decreases for a give heat flux, especially at low heat fluxes. In the single phase region, the HTC is greater for higher mass fluxes where heat removal is dominated by forced convection. Eventually, when boiling becomes fully-developed, the HTC convergences to a single curve for all mass fluxes for a given heat flux.

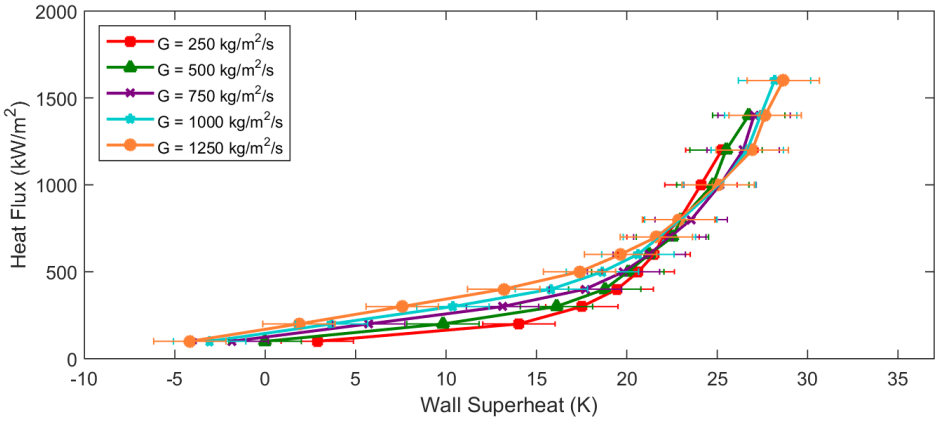

Boiling curves

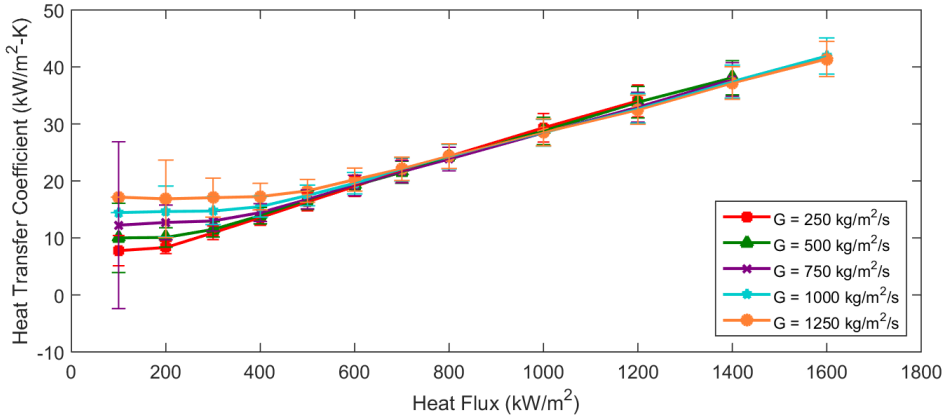

Heat transfer coefficient curves

Figure 5-5: Flow boiling data for uncoated heater at 10° subcooling.

Nucleation site density, bubble departure frequency, and bubble departure diameter data is shown in Figure 5-6. This data also follows expected trends. The nucleation site density increases with increasing wall superheat and decreasing mass flux. As discussed previously in *Phillips (2014)* [10], the nucleation site density counting algorithm saturates at 1100 sites/cm^2, so values above this threshold are not reported. The bubble departure frequency increases with increasing wall superheat and decreasing mass flux. Similarly, the bubble departure diameter data shows an increase in value with increasing heat flux and decreasing mass flux. These overall trends are observed in all the following cases.

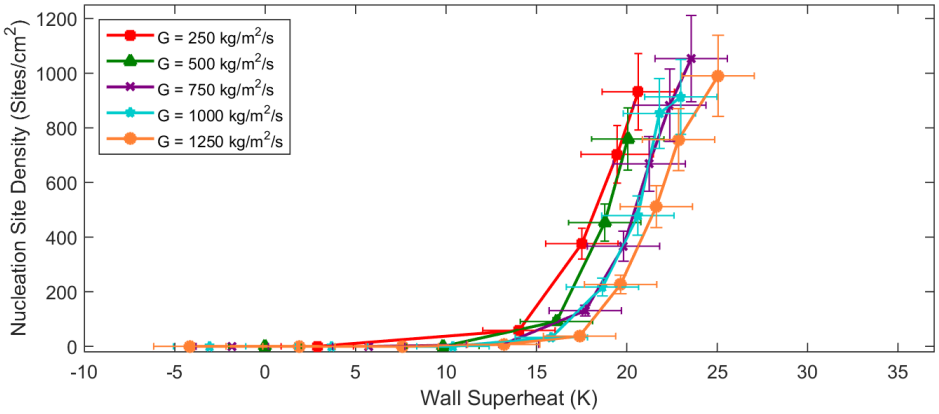

Nucleation site density curves

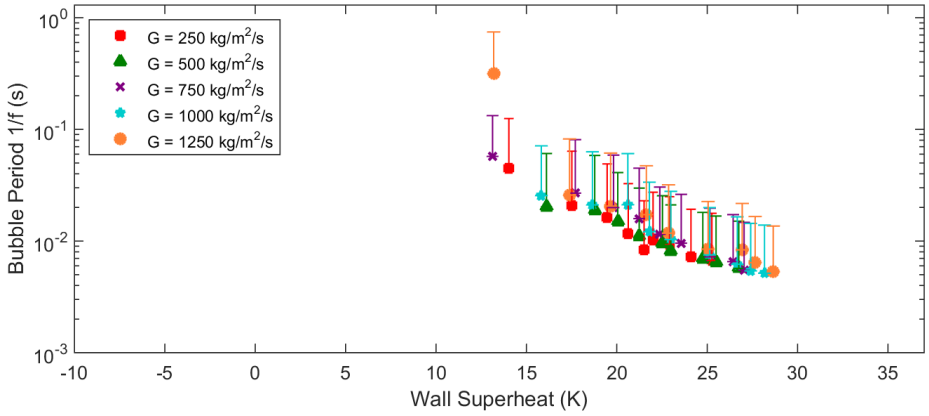

Bubble departure frequency data

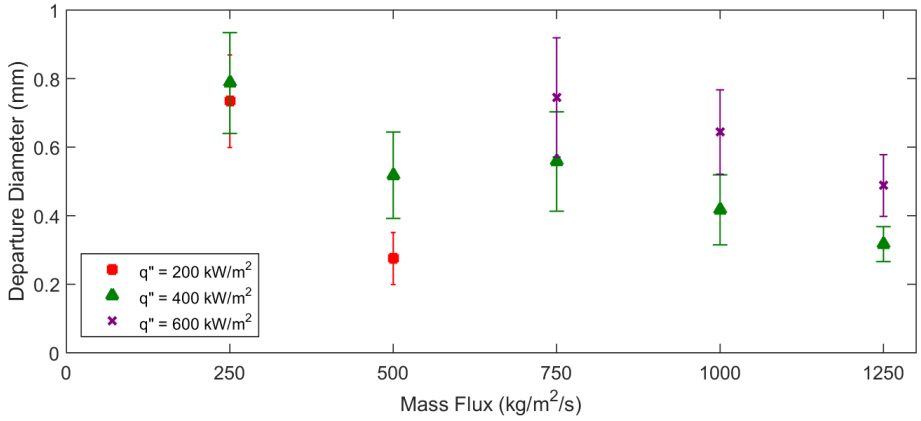

Bubble departure diameter data

Figure 5-6: Flow boiling data for uncoated heater at 10° subcooling.

5.5 Case 1: 2μm Thick, No Chimneys

5.5.1 Surface Analysis

A heater coating 2μm thick with no chimneys was tested to determine if the presence of chimneys improves HTC over a purely porous, hydrophilic surface. The ITO surface was coated directly with the LbL 100nm SiO_2 nanoparticles without any photolithography. The surface properties of this heater case are listed in Table 5.5.

Table 5.5: 2μm thick, no chimneys surface analysis data.

Number of Bilayers	*Contact Angle(°)*	*St. Dev.*	*Thickness (μm)*	*St. Dev.*	*Roughness, R_a (nm)*	*St. Dev.*
140	16.7	8.7%	1.94	1.5%	149.9	9.1%

5.5.2 IR/HSV Results

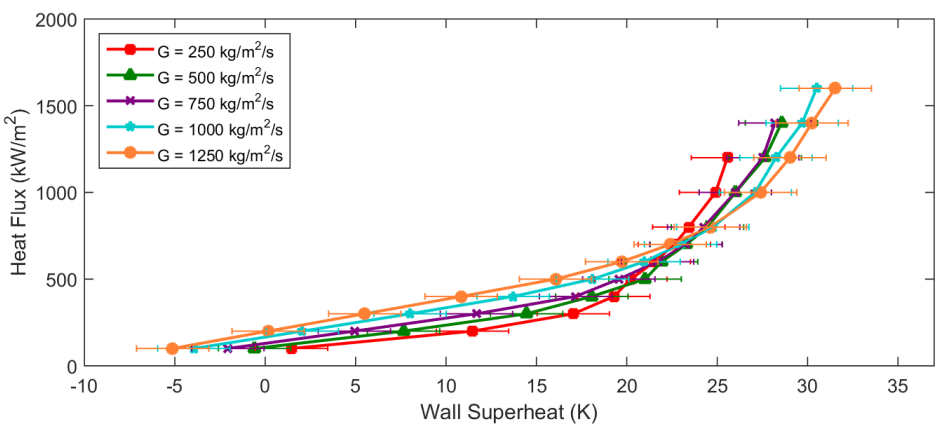

Boiling curves

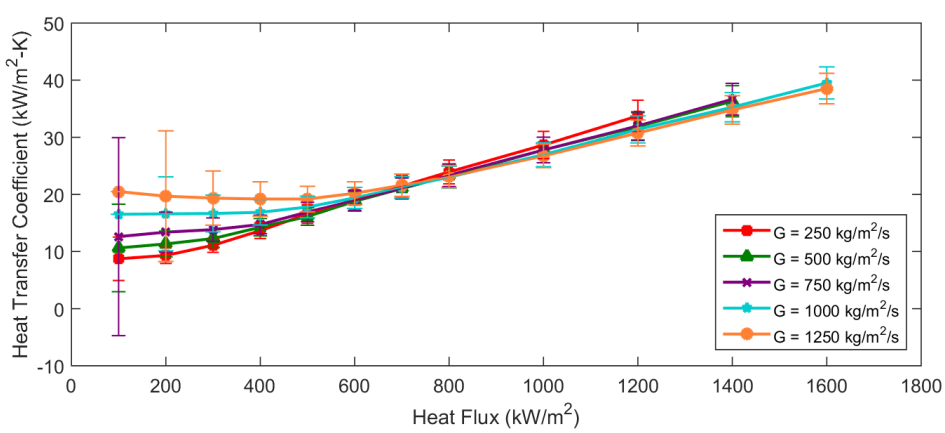

Heat transfer coefficient curves

Figure 5-7: Flow boiling data for 2μm thick, no chimneys heater at 10° subcooling.

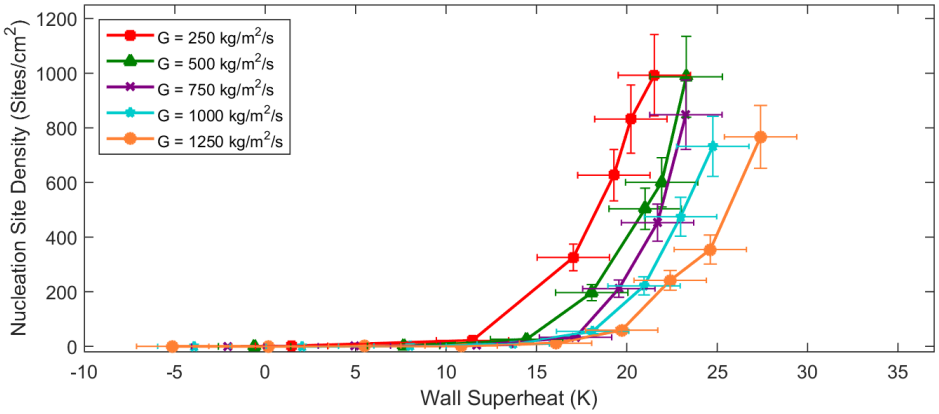

Nucleation site density curves

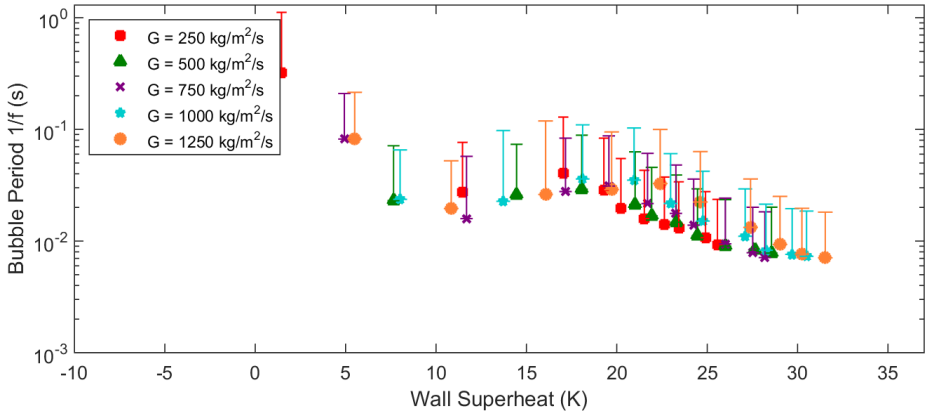

Bubble departure frequency data

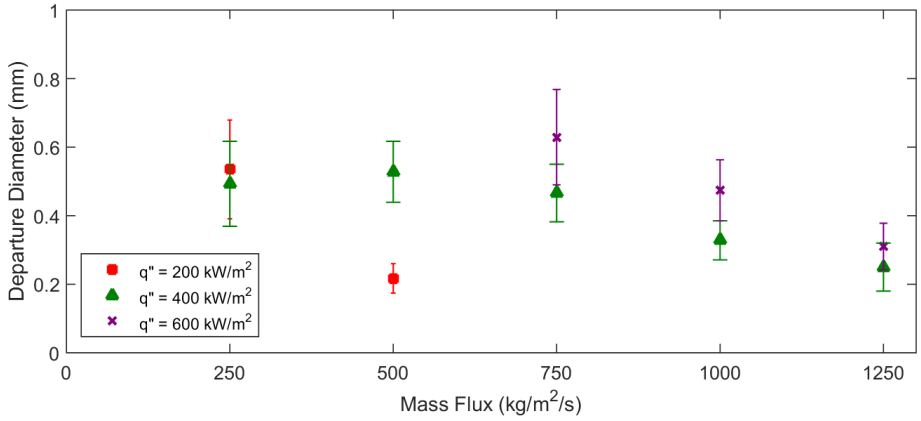

Bubble departure diameter data

Figure 5-8: Flow boiling data for 2μm thick, no chimneys heater at 10° subcooling.

5.6 Case 2: 2μm Thick, 10μm Diameter Chimneys on 25μm Pitch

5.6.1 Surface Analysis

A heater coating 2μm thick with 10μm diameter chimneys on 25μm pitch was tested as the base case of synthetic CRUD coatings for this investigation. The ITO surface was coated with the LbL 100nm SiO_2 nanoparticles with manufactured chimneys and tested in flow boiling. The surface properties of this heater case are listed in Table 5.6.

Table 5.6: 2μm thick, 10μm diameter chimneys on 25μm pitch surface analysis data.

Number of Bilayers	*Contact Angle(°)*	*St. Dev.*	*Thickness (μm)*	*St. Dev.*	*Roughness, R_a (nm)*	*St. Dev.*
140	15.7	9.7%	1.99	6.42%	229	22.6%

5.6.2 IR/HSV Results

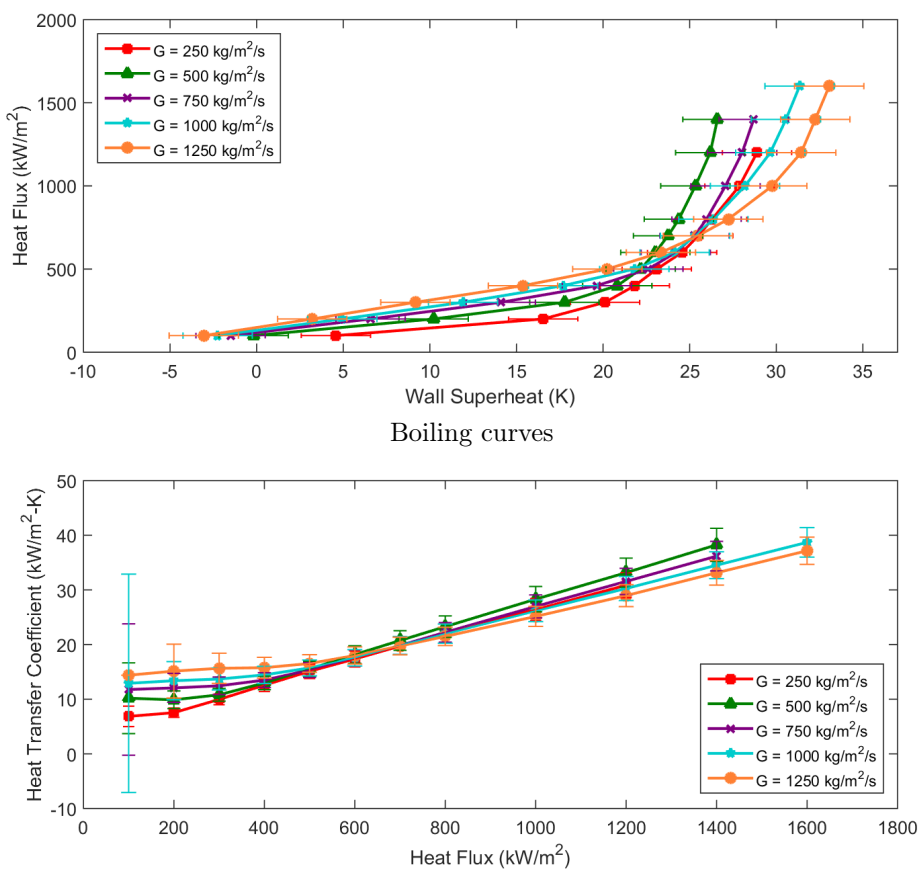

Figure 5-9: Flow boiling data for 2μm thick, 10μm diameter chimneys on 25μm pitch heater at 10° subcooling.

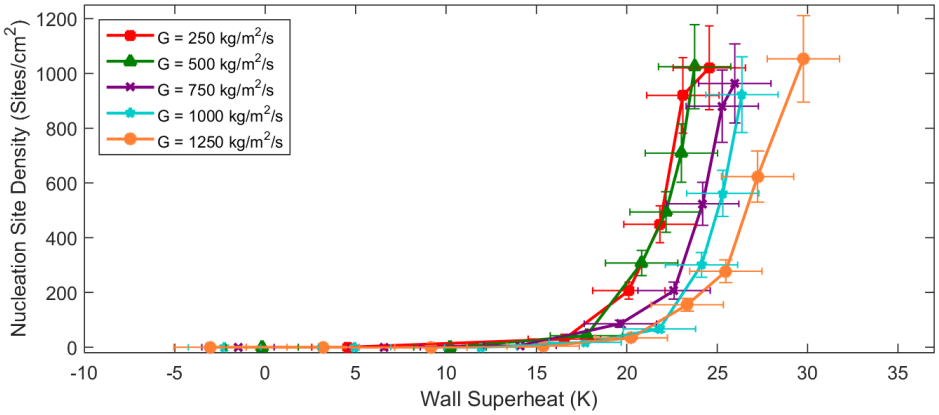

Nucleation site density curves

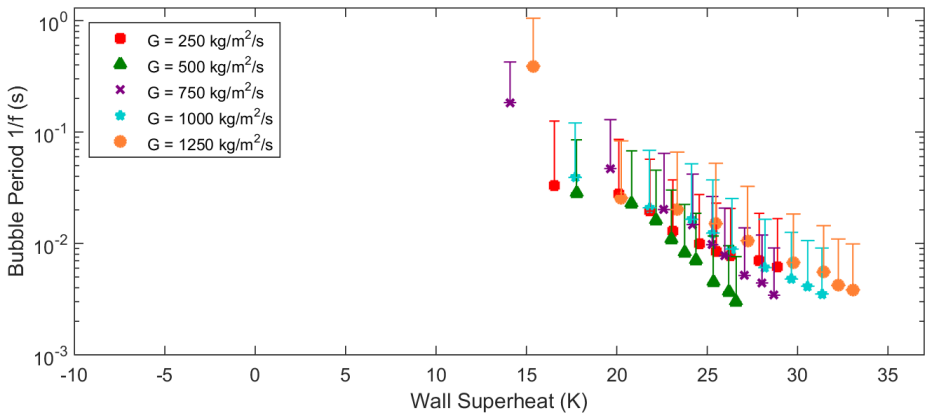

Bubble departure frequency data

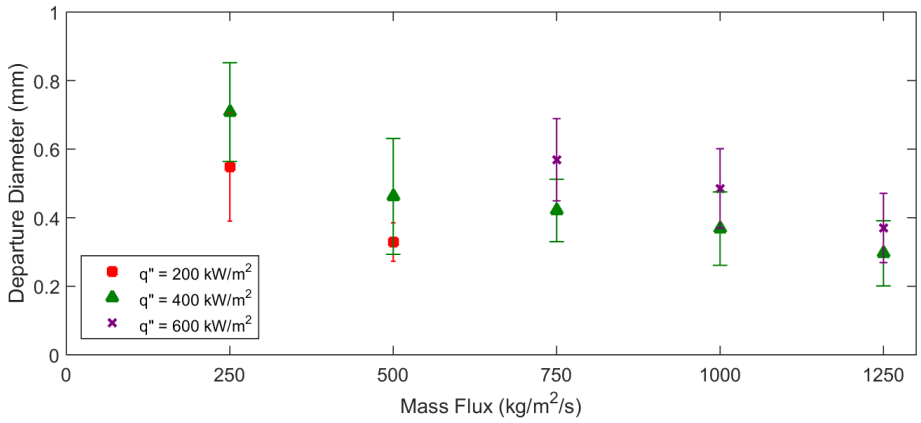

Bubble departure diameter data

Figure 5-10: Flow boiling data for 2μm thick, 10μm diameter chimneys on 25μm pitch heater at 10° subcooling.

5.7 Case 3: 4μm Thick, 10μm Diameter Chimneys on 25μm Pitch

5.7.1 Surface Analysis

A heater coating 4μm thick with 10μm diameter chimneys on 25μm pitch was tested to investigate the effect of CRUD thickness on boiling parameters of interest. By increasing the number of bilayers during the LbL process, a thicker coating was created. The surface properties of this heater case are listed in Table 5.7.

Table 5.7: 4μm thick, 10μm diameter chimneys on 25μm pitch surface analysis data.

Number of Bilayers	*Contact Angle(°)*	*St. Dev.*	*Thickness (μm)*	*St. Dev.*	*Roughness, R_a (nm)*	*St. Dev.*
255	19.0	9.1%	3.92	4.55%	427	11.6%

5.7.2 IR/HSV Results

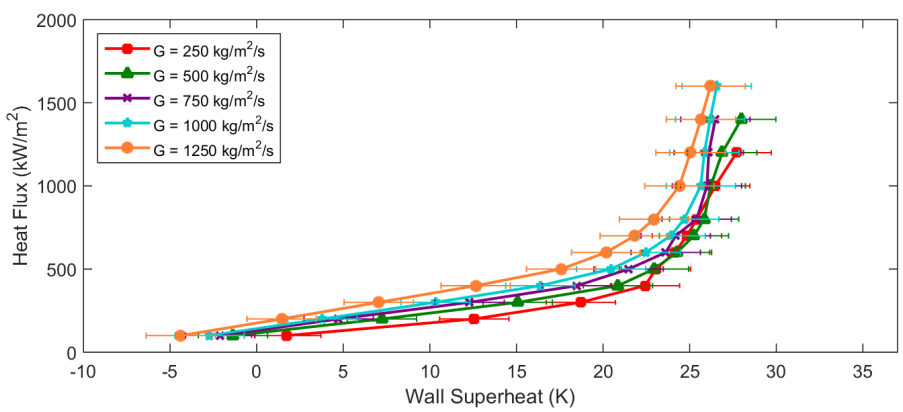

Boiling curves

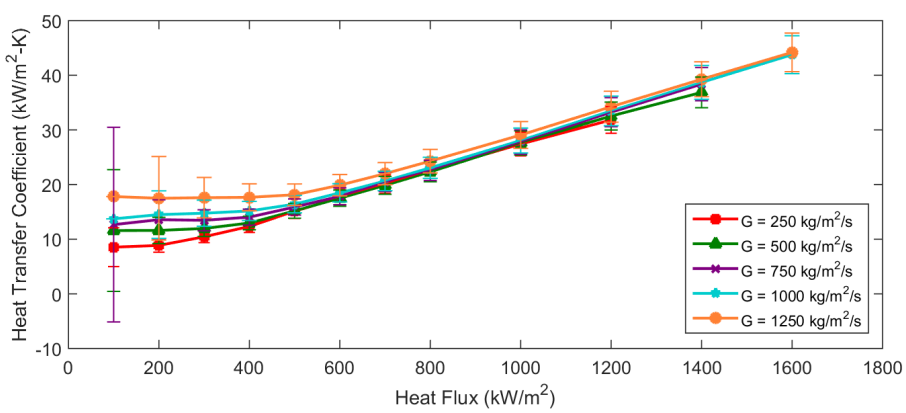

Heat transfer coefficient curves

Figure 5-11: Flow boiling data for 4μm thick, 10μm diameter chimneys on 25μm pitch heater at 10° subcooling.

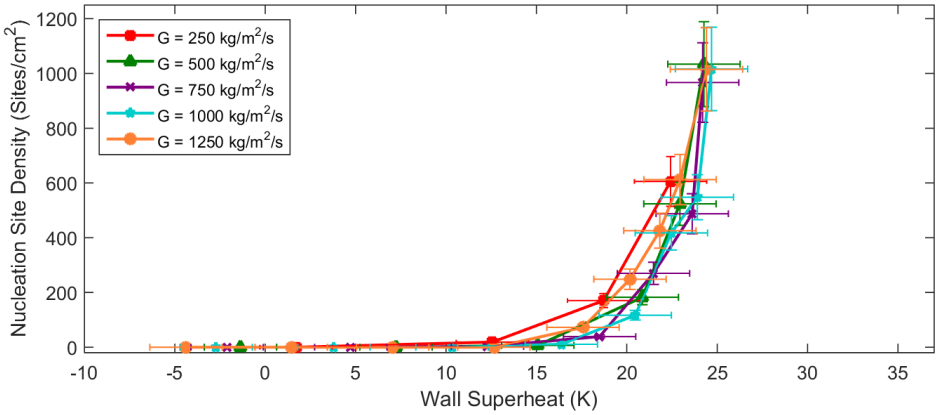

Nucleation site density curves

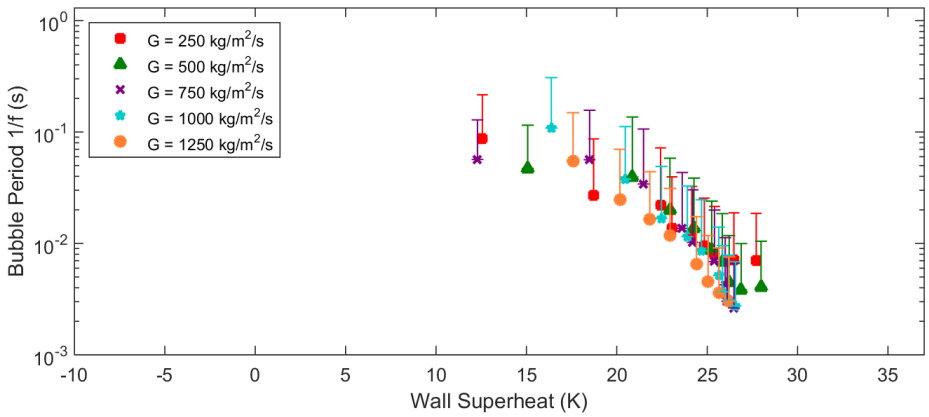

Bubble departure frequency data

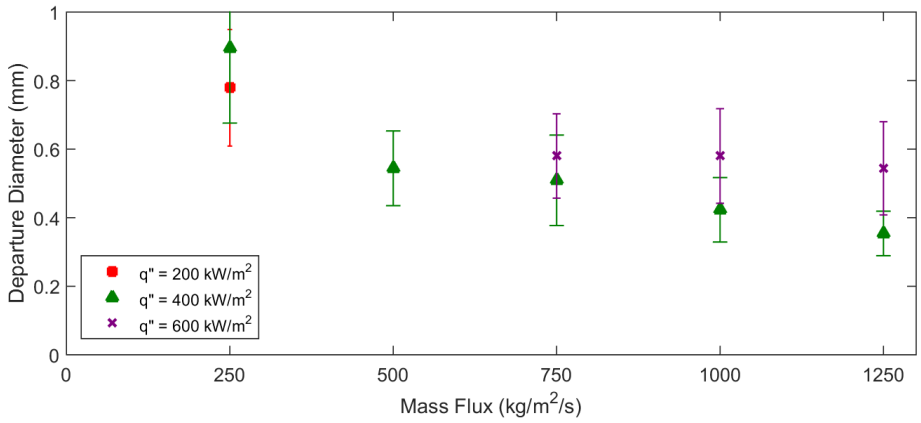

Bubble departure diameter data

Figure 5-12: Flow boiling data for 4μm thick, 10μm diameter chimneys on 25μm pitch heater at 10° subcooling.

5.8 Case 6: 2μm Thick, 10μm Diameter Chimneys on 45μm Pitch

5.8.1 Surface Analysis

A heater coating 2μm thick with 10μm diameter chimneys on 45μm pitch was tested to investigate the effect of chimney pitch on boiling parameters of interest. By changing the mask pattern used during the photolithography process, photoresist posts were created at varying pitches. The surface properties of this heater case are listed in Table 5.8.

Table 5.8: 2μm thick, 10μm diameter chimneys on 45μm pitch surface analysis data.

Number of Bilayers	*Contact Angle(°)*	*St. Dev.*	*Thickness (μm)*	*St. Dev.*	*Roughness, R_a (nm)*	*St. Dev.*
140	17.2	5.4%	2.05	3.6%	295.5	14.5%

5.8.2 IR/HSV Results

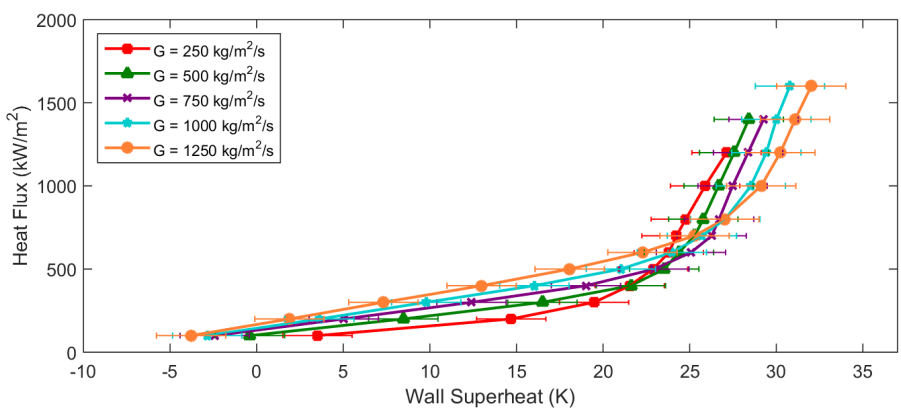

Boiling curves

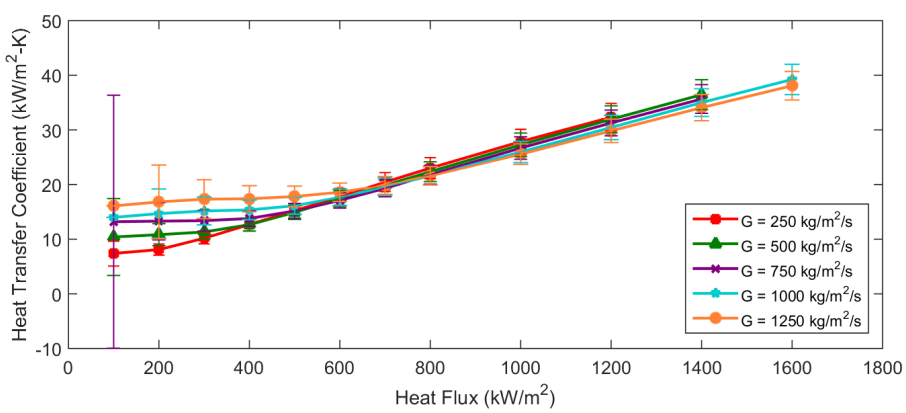

Heat transfer coefficient curves

Figure 5-13: Flow boiling data for 2μm thick, 10μm diameter chimneys on 45μm pitch heater at 10° subcooling.

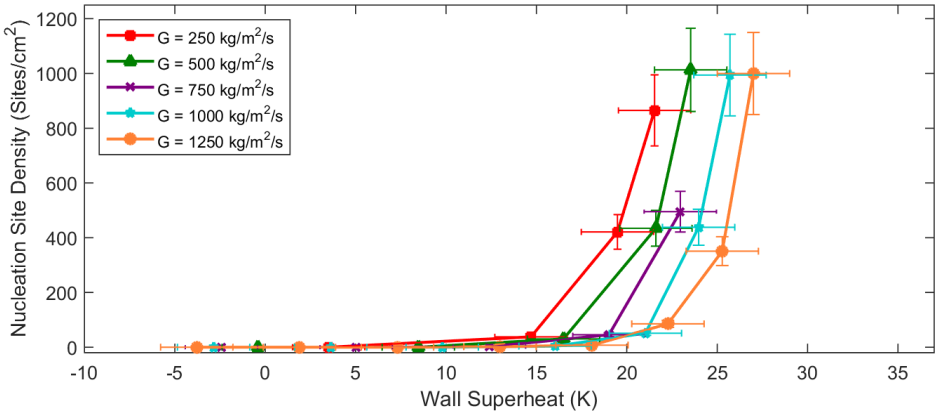

Nucleation site density curves

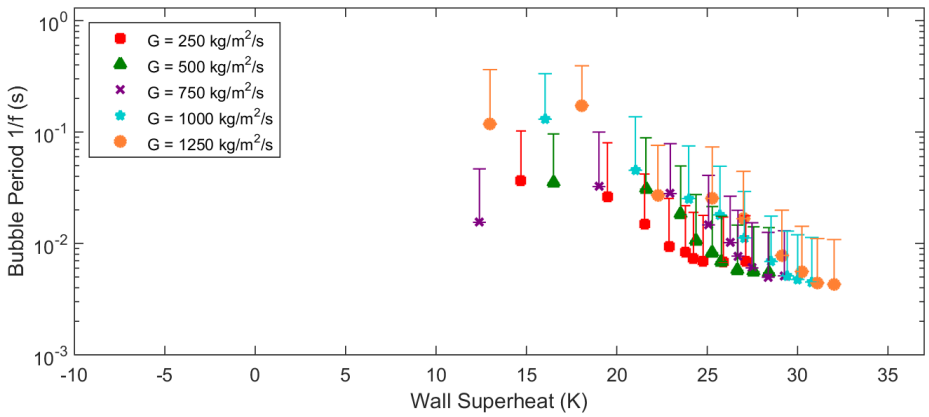

Bubble departure frequency data

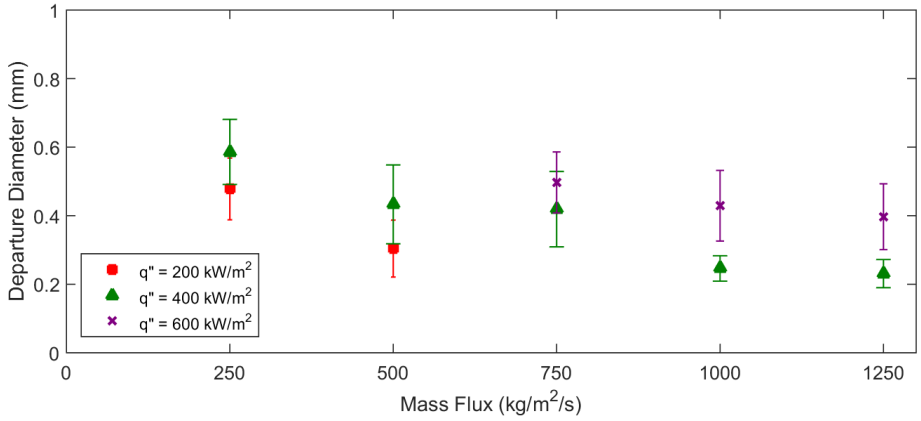

Bubble departure diameter data

Figure 5-14: Flow boiling data for 2μm thick, 10μm diameter chimneys on 45μm pitch heater at 10° subcooling.

5.9 Case 7: 2μm Thick, 12.5μm Diameter Chimneys on 27.5μm Pitch

5.9.1 Surface Analysis

A heater coating 2μm thick with 12.5μm diameter chimneys on 27.5μm pitch was tested to investigate the effect of chimney diameter on boiling parameters of interest. Similarly to altering the chimney pitch, a different mask pattern is used during the photolithography process to create larger post diameters.The surface properties of this heater case are listed in Table 5.9.

Table 5.9: 2μm thick, 12.5μm diameter chimneys on 27.5μm pitch surface data.

Number of Bilayers	*Contact Angle(°)*	*St. Dev.*	*Thickness (μm)*	*St. Dev.*	*Roughness, R_a (nm)*	*St. Dev.*
140	19.2	7.9%	2.1	6.4%	261.2	16.5%

5.9.2 IR/HSV Results

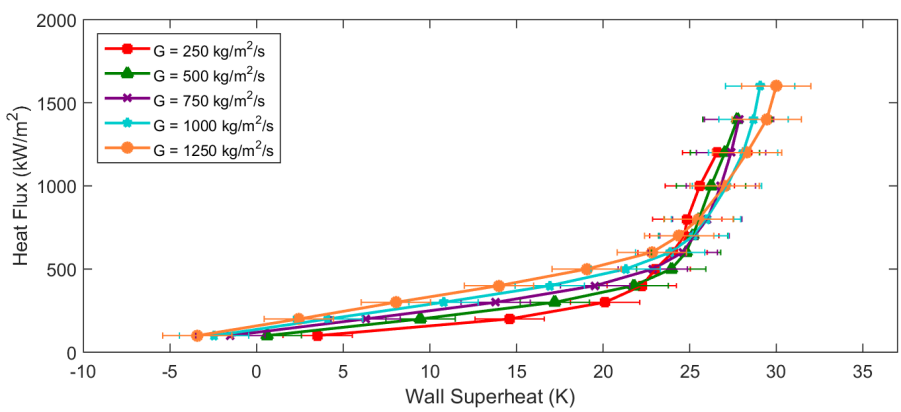

Boiling curves

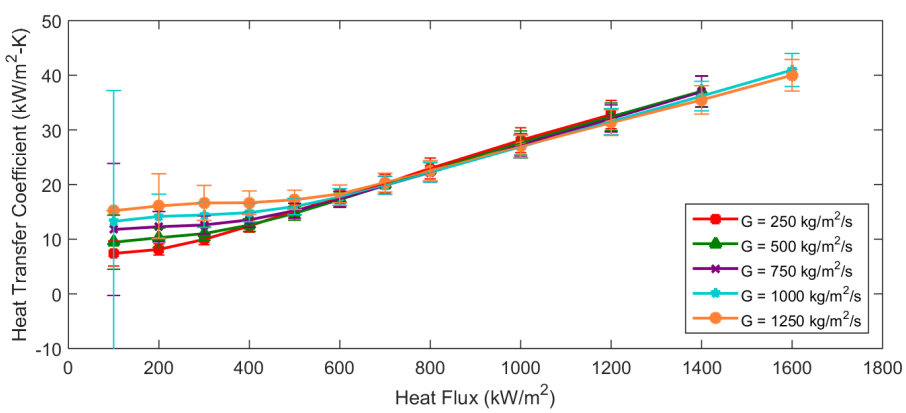

Heat transfer coefficient curves

Figure 5-15: Flow boiling data for 2μm thick, 12.5μm diameter chimneys on 27.5μm pitch heater at 10° subcooling.

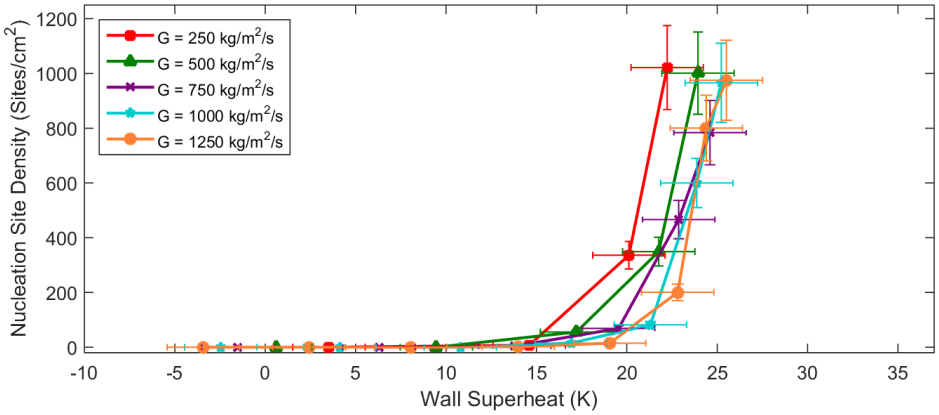

Nucleation site density curves

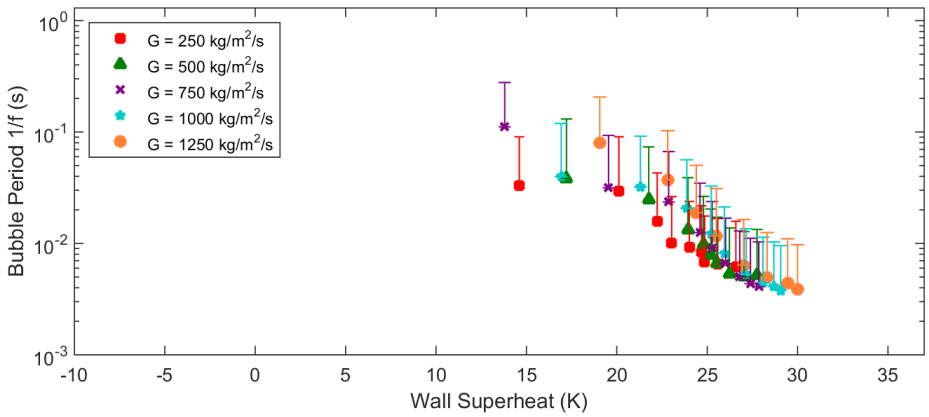

Bubble departure frequency data

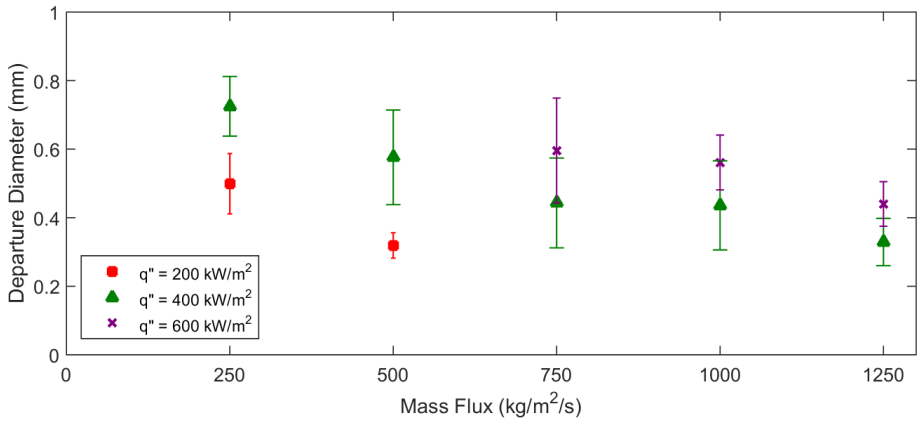

Bubble departure diameter data

Figure 5-16: Flow boiling data for 2μm thick, 12.5μm diameter chimneys on 27.5μm pitch heater at 10° subcooling.

6 Discussion: Effects of Layer Thickness and Chimney Pitch and Diameter

In this chapter, the results of pool and flow boiling tests are compared between different coatings to determine the effects of layer thickness and chimney pitch and diameter. The nucleation site density, bubble departure frequency, and bubble departure diameter are discussed in terms of their contributions to the heat transfer coefficient.

6.1 Effect of Synthetic CRUD

This section discusses the effects of synthetic CRUD on heat transfer coefficient and bubble parameters. Figures 6-1 and 6-2 show these parameters at three mass fluxes compared for Cases 0 (uncoated) and 2 (2,10-25).

It can be observed that the HTC of the uncoated heater higher than that of the heater with synthetic CRUD. This is explained by the higher nucleation site density for a given wall superheat and a larger bubble departure diameter for a given mass flux for the uncoated heater. The bubble departure frequency is relatively unaffected.

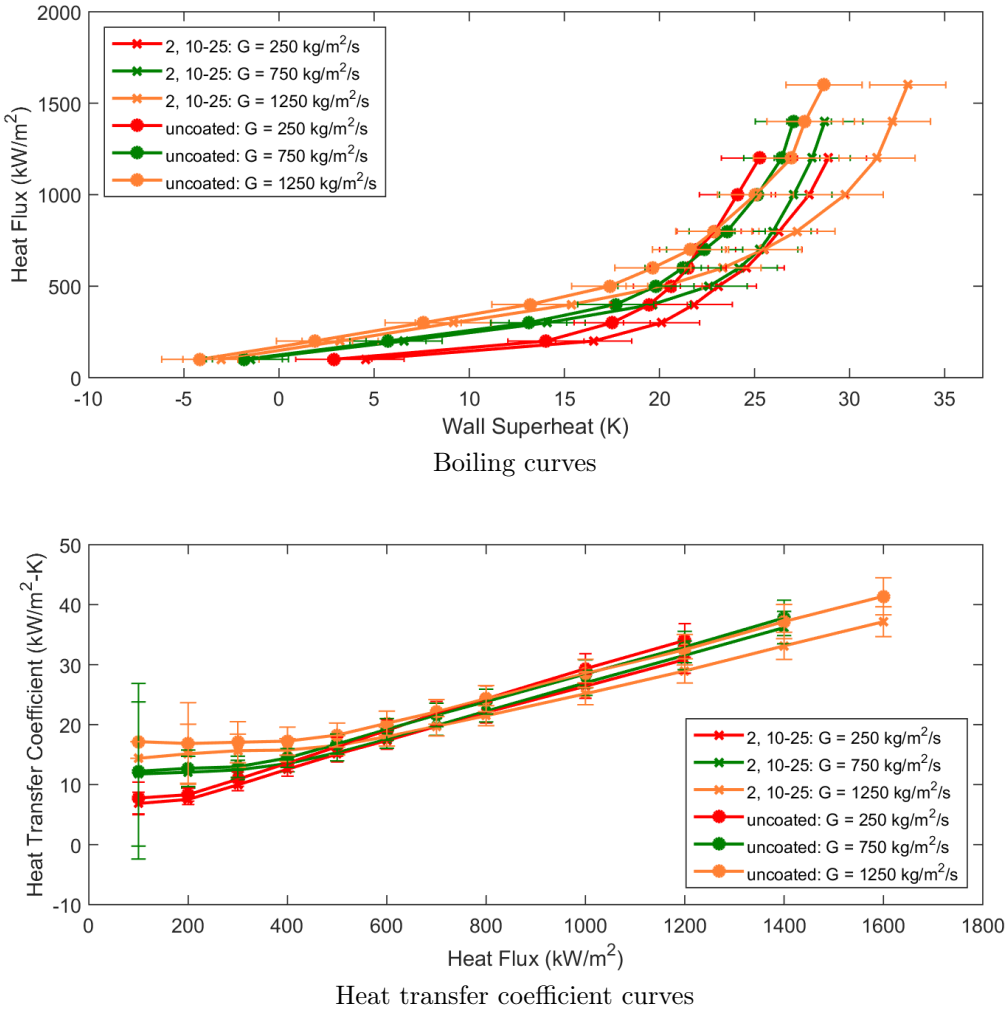

Figure 6-1: Flow boiling data for CRUD presence comparison.

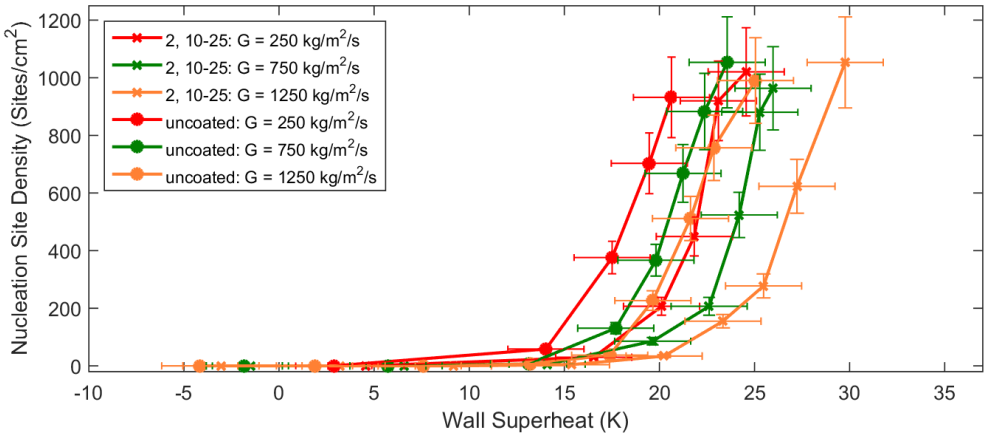

Nucleation site density curves

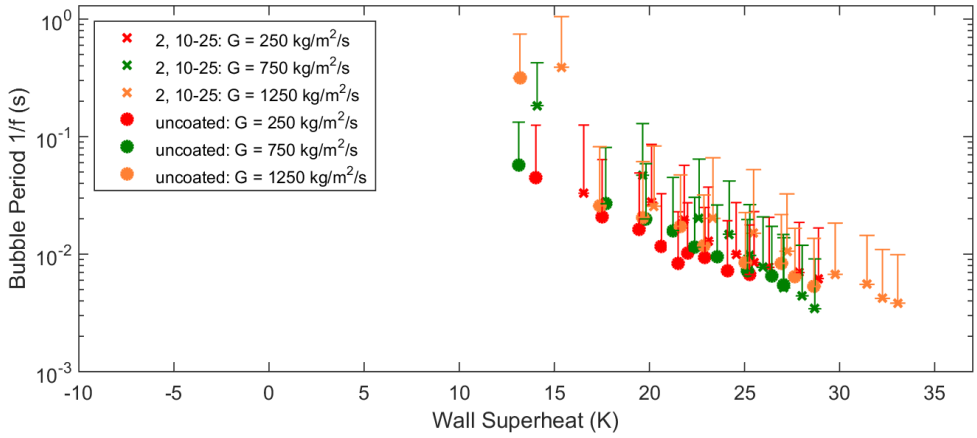

Bubble departure frequency data

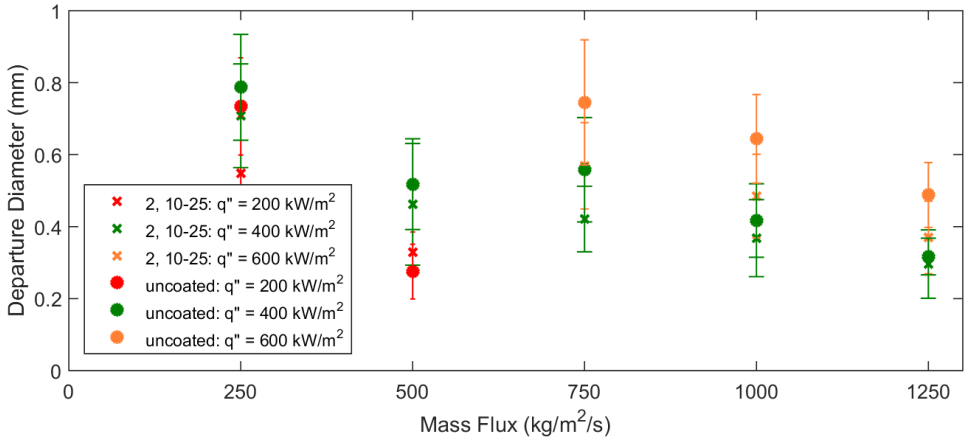

Bubble departure diameter data

Figure 6-2: Flow boiling data for CRUD presence comparison.

6.2 Effect of Chimneys

This section discusses the effects of chimneys on heat transfer coefficient and bubble parameters. Figures 6-3 and 6-4 show these parameters at three mass fluxes compared for Cases 1 (2,no chimney) and 2 (2,10-25) which are 2μm thick coatings without and with chimneys, respectively.

It can be observed that the HTC of the heater without chimneys is very slightly higher than that of the heater with chimneys, although the the overlap in uncertainty makes it more difficult to draw a conclusion. This is explained by the higher nucleation site density for a given wall superheat for the Case 1 heater. The bubble departure frequency and bubble departure diameter are relatively unaffected.

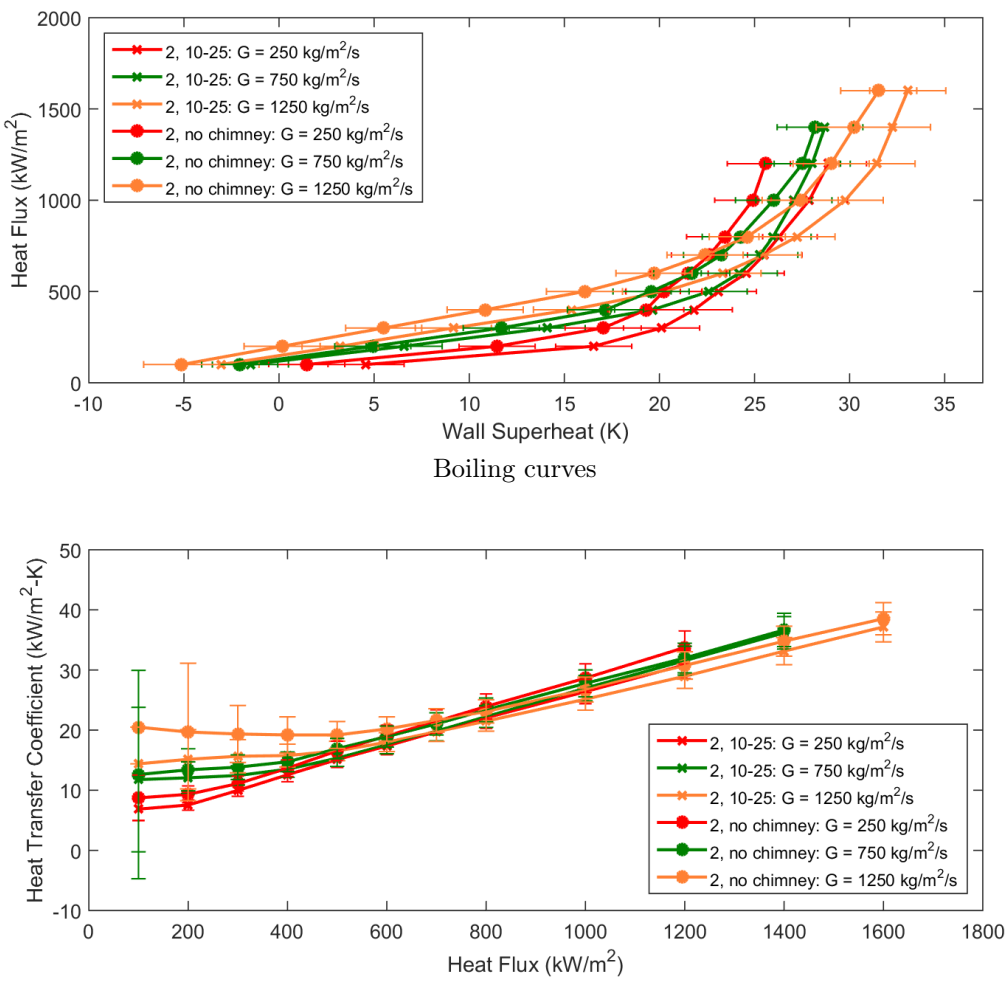

Figure 6-3: Flow boiling data for chimney presence comparison.

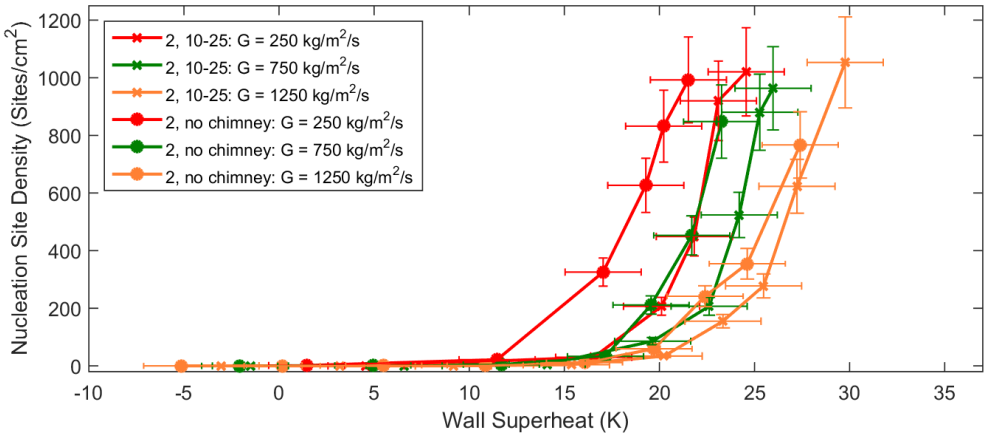

Nucleation site density curves

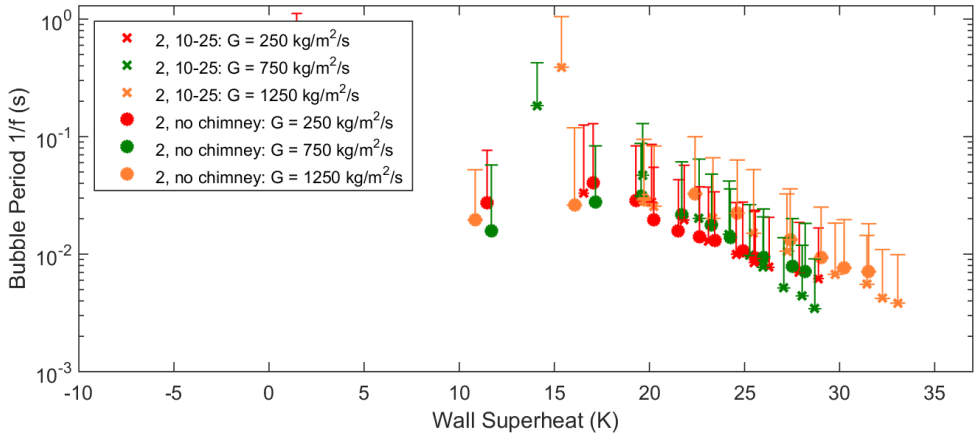

Bubble departure frequency data

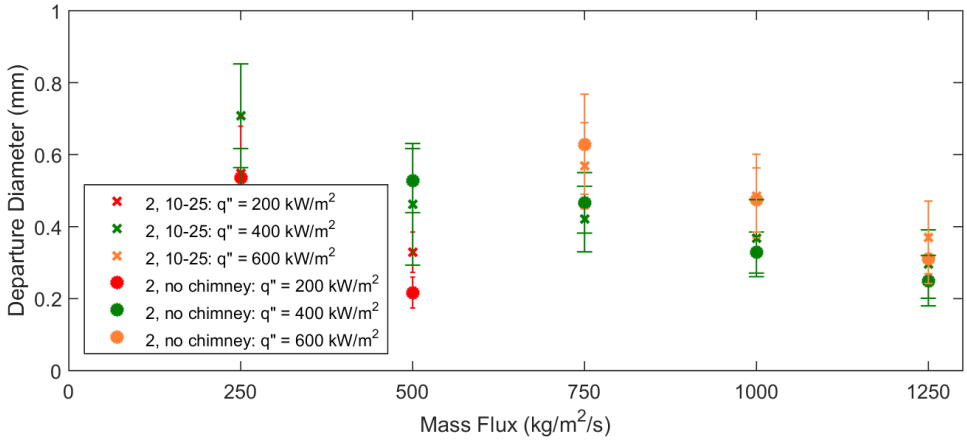

Bubble departure diameter data

Figure 6-4: Flow boiling data for chimney presence comparison.

6.3 Effect of Layer Thickness

This section discusses the effects of layer thickness on heat transfer coefficient and bubble parameters. Figures 6-5 and 6-6 show these parameters at three mass fluxes compared for Cases 2 (2,10-25) and 3 (4,10-25) which are 2μm thick and 4μm thick, respectively, with 10μm diameter chimneys on 25μm pitch.

It can be observed that the HTC of the 4μm thick coating is larger than that of the 2μm thick coating. This is explained by the higher nucleation site density, smaller bubble departure period (larger bubble departure frequency), and larger bubble departure diameter for a given wall superheat and mass flux for the Case 3 heater.

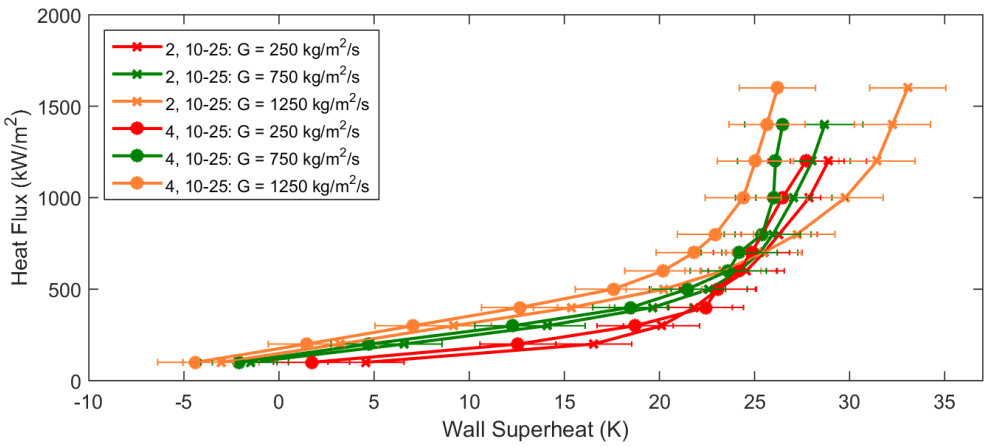

Boiling curves

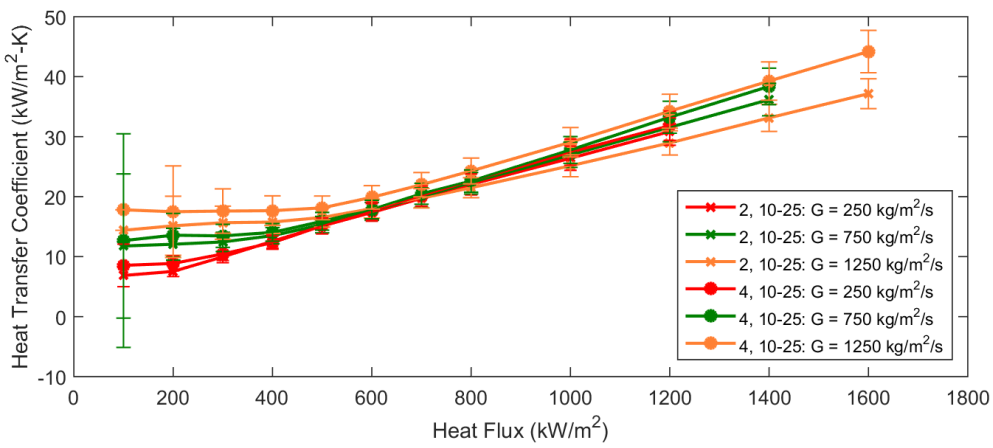

Heat transfer coefficient curves

Figure 6-5: Flow boiling data for thickness comparison.

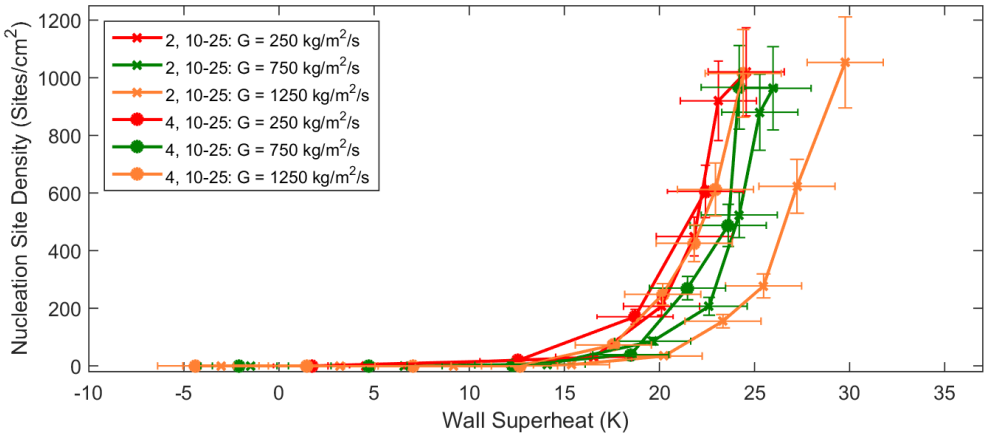

Nucleation site density curves

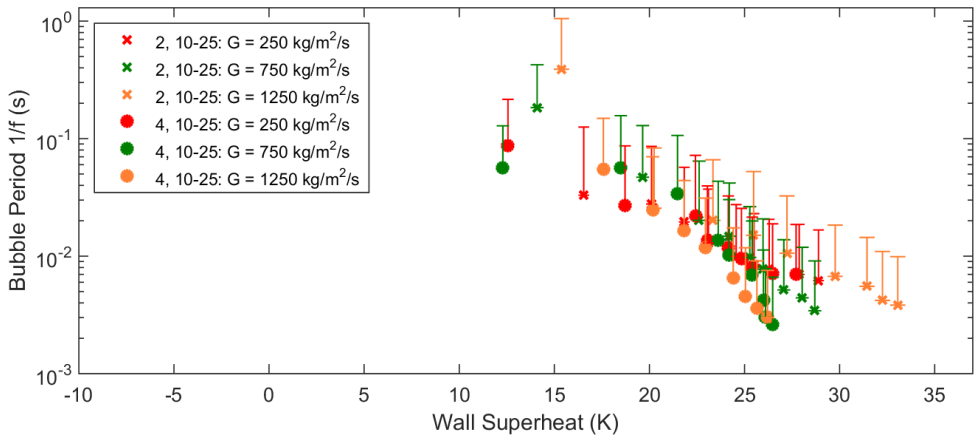

Bubble departure frequency data

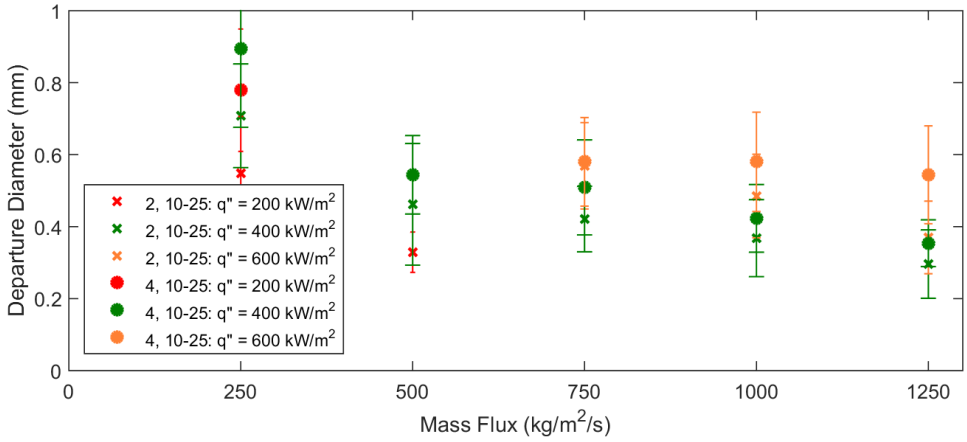

Bubble departure diameter data

Figure 6-6: Flow boiling data for thickness comparison.

6.4 Effect of Chimney Pitch

This section discusses the effects of chimney pitch on heat transfer coefficient and bubble parameters. Figures 6-7 and 6-8 show these parameters at three mass fluxes compared for Cases 2 (2,10-25) and 6 (2,10-45) which are 2μm thick with 10μm diameter chimneys on 25μm and 45μm pitches, respectively.

It can be observed that the HTCs of the 25μm pitch and 45μm pitch coatings are roughly the same and are within the uncertainty of each other. The bubble departure frequency and bubble departure diameter are comparable. However, the nucleation site density of the 45μm pitch heater is slightly higher.

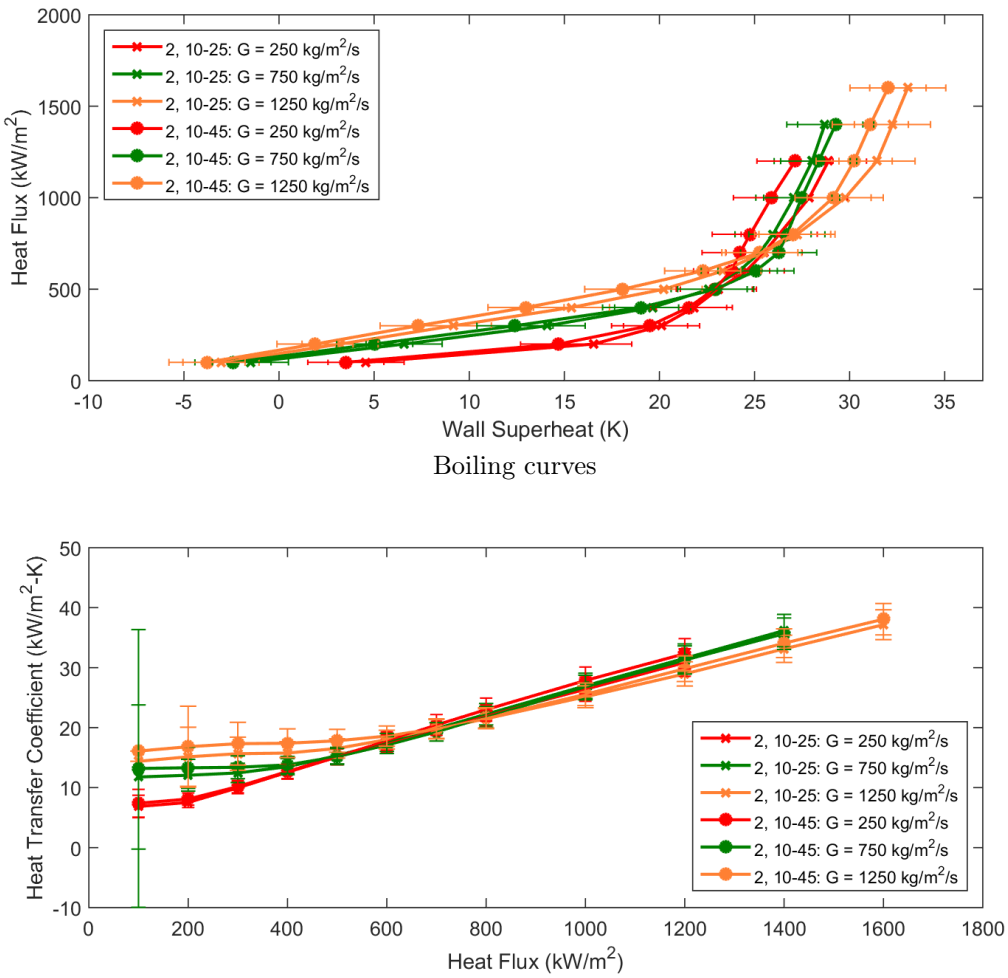

Figure 6-7: Flow boiling data for chimney pitch comparison.

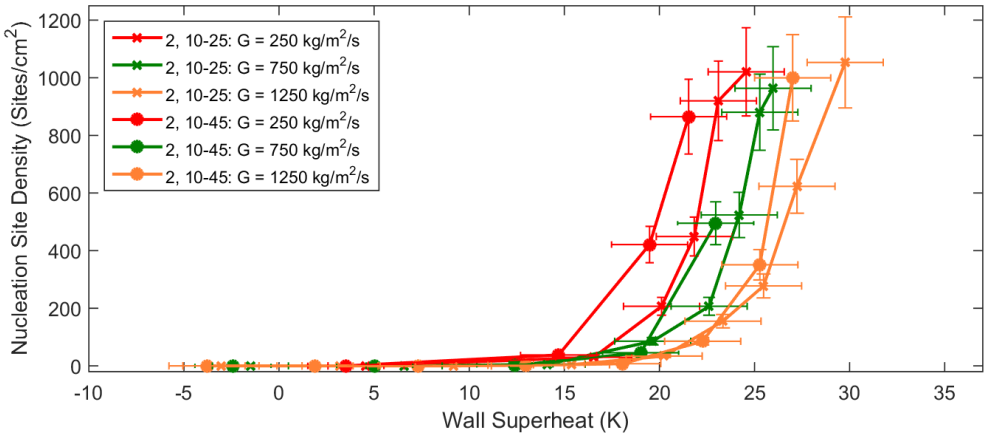

Nucleation site density curves

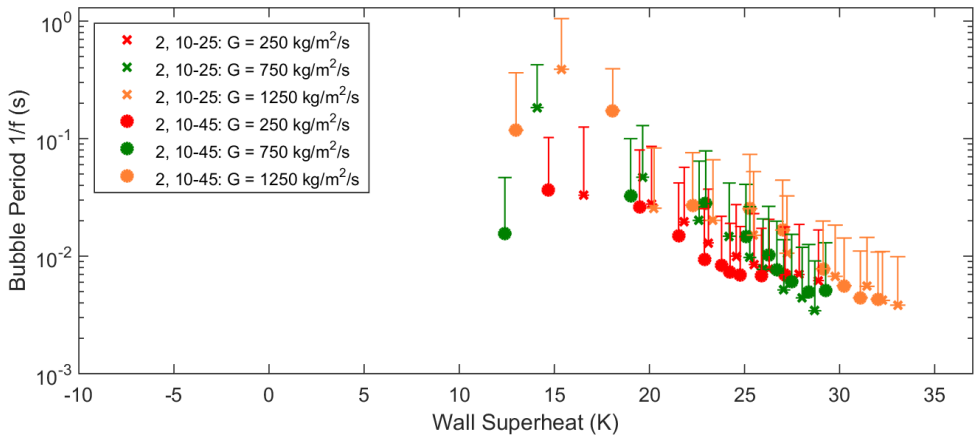

Bubble departure frequency data

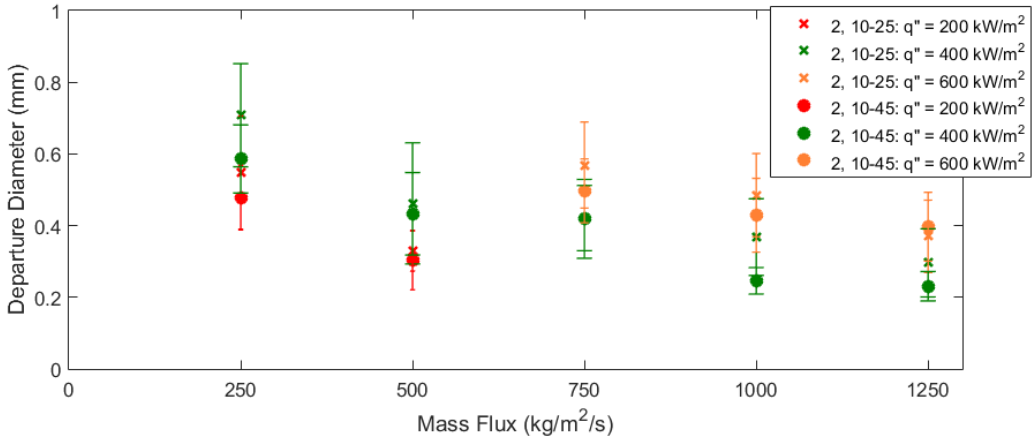

Bubble departure diameter data

Figure 6-8: Flow boiling data for chimney pitch comparison.

6.5 Effect of Chimney Diameter

This section discusses the effects of chimney diameter on heat transfer coefficient and bubble parameters. Figures 6-9 and 6-10 show these parameters at three mass fluxes compared for Cases 2 (2,10-25) and 7 (2,12.5-27.5) which are 2μm thick with 10μm and 12.5μm diameter chimneys on 25μm and 27.5μm pitches, respectively.

It can be observed that the HTC of the 12.5μm diameter chimneys is slightly larger than that of the 10μm diameter chimney coating, especially at high mass fluxes. This consistent with the larger nucleation site density of the 12.5μm diameter heater. The bubble departure diameter and bubble departure frequency are roughly the same.

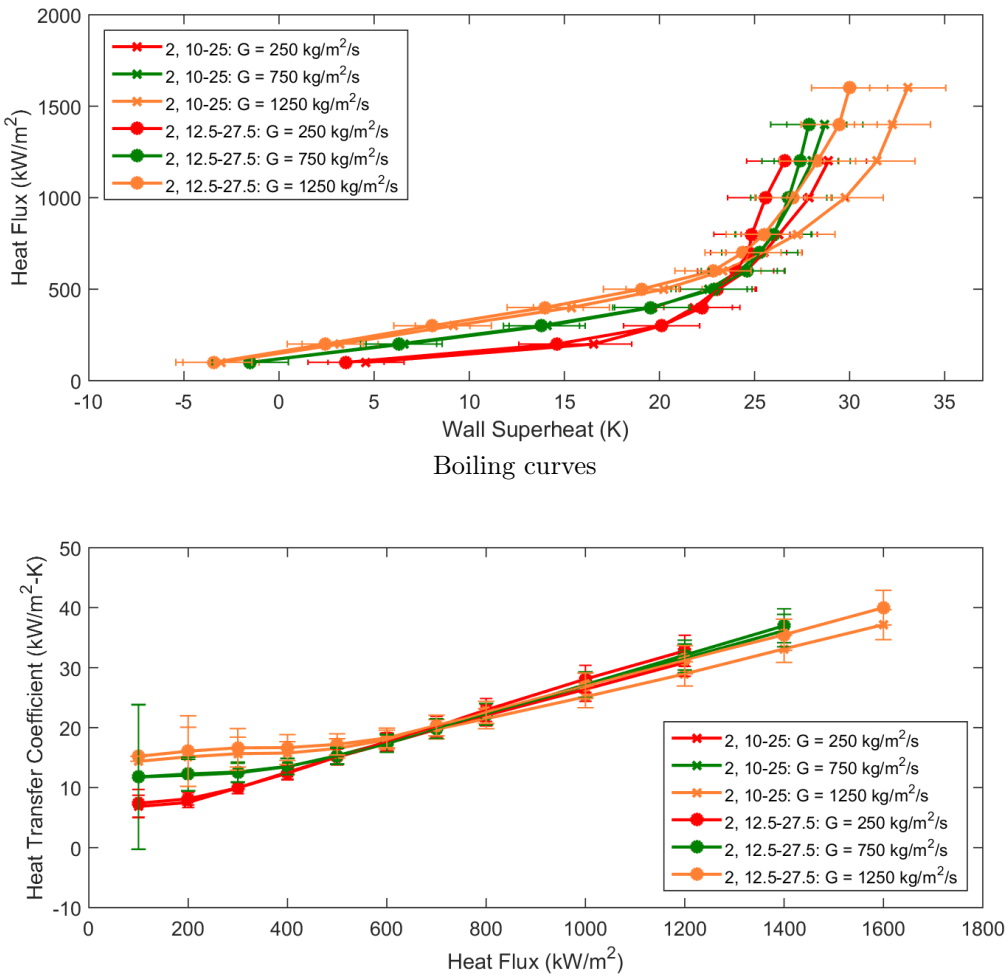

Figure 6-9: Flow boiling data for chimney diameter comparison.

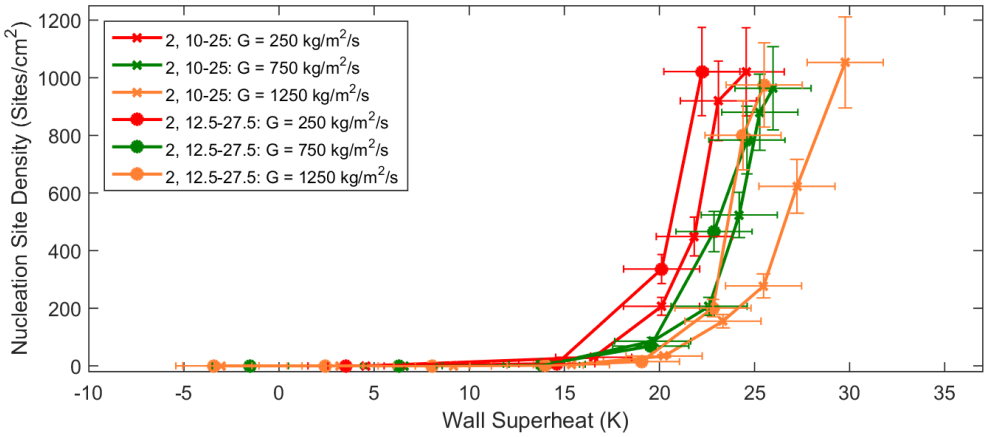

Nucleation site density curves

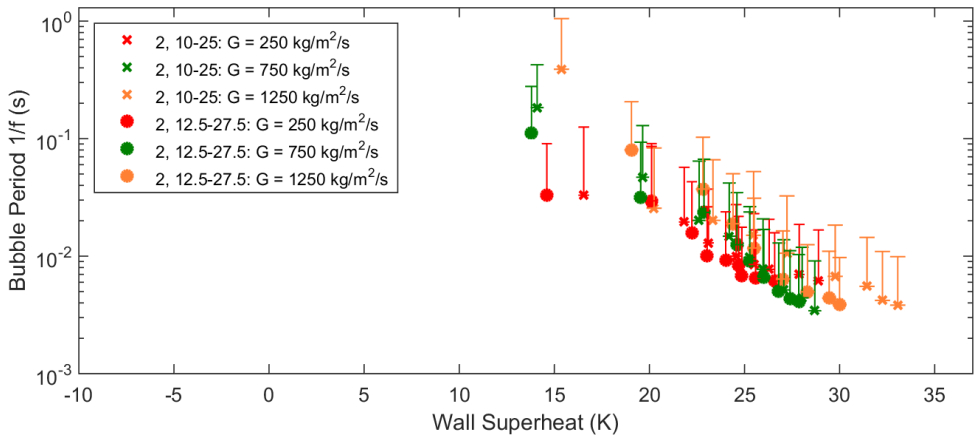

Bubble departure frequency data

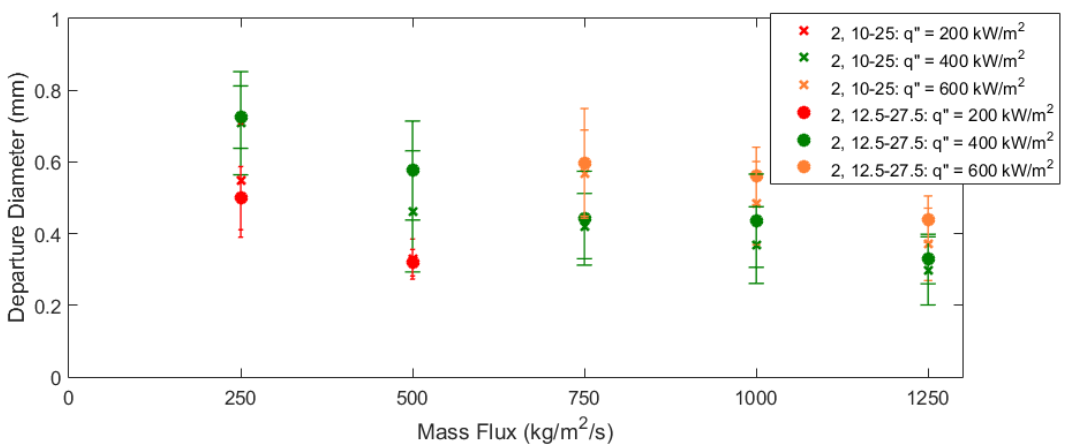

Bubble departure diameter data

Figure 6-10: Flow boiling data for chimney diameter comparison.

6.6 Future Work

Future work would include data for the remainder of the test matrix. Additionally, further study of the physical mechanisms causing the observed trends would be conducted.

7 Conclusions

Synthetic CRUD has been successfully manufactured and tested using advanced IR/HSV analysis techniques. Pool boiling data has shown that silica nanoparticles are an acceptable substitute for iron oxide particles. Flow boiling tests were conducted to test the effects of synthetic CRUD on heat transfer coefficient and bubble parameters such as nucleation site density, bubble departure frequency, and bubble departure diameter. Different synthetic CRUD patterns were tested to determine the effects of layer thickness and chimney pitch and diameter on bubble properties. From the completed cases, the IR/HSV data as shown that the HTC increases with increasing thickness and increasing chimney diameter, while the presence of chimneys and chimney pitch did not appear to affect the results. The statistical significance of the observed changes varied with mass flux.

Bibliography

[1] Kim, S. J., I. C. Bang, J. Buongiorno, and L. W. Hu. "Effects of Nanoparticle Deposition on Surface Wettability Influencing Boiling Heat Transfer in Nanofluids." Applied Physics Letters 89.15 (2006): 153107.

[2] Forrest, E., et al., "Augmentation of Nucleate Boiling Heat Transfer and Critical Heat Flux Using Nanoparticle Thin-film Coatings." International Journal of Heat and Mass Transfer 53.1-3 (2010): 58-67.

[3] O'Hanley, H., Coyle, C., Cohen, R., et al. "Separate effects of surface roughness, wettability, and porosity on the boiling critical heat flux." Applied Physics Letters. 103.2 (2013): 024102.

[4] H. Kim, B. Truong, J. Buongiorno, L. W. Hu, "On the Effect of Surface Roughness, Wettability and Nano-Porosity on Leidenfrost Phenomena." Applied Physics Letters, 98 (2011): 083121.

[5] Buongiorno, Jacopo. "Can Corrosion and CRUD Actually Improve Safety Margins in LWRs?" Annals of Nuclear Energy 63 (2014): 9-21.

[6] Tetreault-Friend, Melanie. "Systematic Investigation of the Effects of Hydrophilic Porosity on Boiling Heat Transfer and Critical Heat Flux." Thesis. Massachusetts Institute of Technology, 2014.

[7] O'Hanley, Harry. "Seperate Effects of Surface Roughness, Wettability, and Porosity on Boiling Heat Transfer and Critical Heat Flux and Optimization of Boiling Surfaces." Thesis. Massachusetts Institute of Technology, 2012.

[8] N.E. Todreas, Mujid S. Kazimi, Nuclear Systems I: Thermal Hydraulic Fundamentals, Taylor & Francis 1993.

[9] Yan, Jin, et al. "Multi-Physics Computational Models Development for Westinghouse PWRs." Transactions of the American Nuclear Society 109 (2013): 1643-45.

[10] Phillips, Bren, "Experimental Investigation of Subcooled Flow Boiling Using Synchronized High Speed Video, Infrared Thermography, and Particle Image Velocimetry." Thesis. Massachusetts Institute of Technology, 2014.

[11] Carey, V.P., *Liquid-Vapor Phase-Change Phenomena.* Taylor & Francis, 2nd ed., 2008.

[12] Lemmert, M., J. M. Chawla, “Influence of flow velocity on surface boiling heat transfer coefficient," in Heat Transfer in Boiling (E. Hahne and U. Grigull, eds.), Academic Press, 1977.

[13] Hibiki, Takashi, Mamoru Ishii. “Active Nucleation Site Density In Boiling Systems." International Journal Of Heat And Mass Transfer 46(2003): 2587-2601.

[14] Basu, N., G.R. Warrier, V.K. Dhir., “Onset of Nucleate Boiling and Active Nucleation Site Density During Subcooled Flow Boiling", J. Heat Transfer 124 (2002) 717-728.

[15] Han, Y.Y., and Griffith, P., “The Mechanism of Heat Transfer in Nucleate Pool Boiling. 1: Bubble Initiation, Growth and Departure," International Journal of Heat Mass Transfer, Vol. 8 (1965) 887-904.

[16] Yeoh, G.H., et al. “Modeling Subcooled Flow Boiling In Vertical Channels At Low Pressures - Part 2: Evaluation Of Mechanistic Approach." International Journal Of Heat And Mass Transfer 75 (2014): 754-768.

[17] Situ, R., et al. “Bubble Departure Frequency In Forced Convective Subcooled Boiling Flow." International Journal Of Heat And Mass Transfer 51.(2008): 6268-6282.

[18] Basu, N., G.R. Warrier, V.K. Dhir, “Wall heat flux partitioning during subcooled flow boiling: Part 1: Model Development", J. Heat Transfer 127 (2005) 131-139.

[19] Klausner, J., R. Mei, D. Bernhard, and L. Zeng, “Vapor bubble departure in forced convection boiling," International Journal of Heat and Mass Transfer, (1993) 36:3 651?662.

[20] Sugrue, R., and J. Buongiorno, “A modified force-balance model for predicting bubble departure diameter in subcooled flow boiling," Proceedings of The 15th International Topical Meeting on Nuclear Reactor Thermal-Hydraulics, NURETH-15, 2013.

[21] Collier, J.G., J.R. Thome, Convective Boiling and Condensation, 3rd Ed. Oxford University Press, Oxford, UK, 1994.

[22] Rohsenow, W.M., A method of correlating heat transfer dta for surface boiling of liquids. Trans. ASME, 74 (1952) 969-976.

[23] Jens, W.H. and Lottes, P.A., “Analysis of Heat Transfer, Burnout, Pressure Drop and Density Data for High Pressure Water. Report ANL-4627, Argonne, IL, (1951).

[24] Chen, J.C., “A Correlation for Boiling Heat Transfer to Saturated Fluids in Convective Flow. ASME (1963) 63-HT-34.

[25] Forster, K. and Zuber, N., “Dynamics of vapor bubbles and boiling heat transfer," AIChE J. (1955) 1:531.

[26] Klimenko, V.V. “A Generalized Correlation For Two-Phase Forced Flow Heat Transfer-Second Assessment." International Journal Of Heat And Mass Transfer 33.10 (1990): 2073-2088.

[27] Kurul, N., and M.Z. Podowski, “Multidimensional effects in forced convection subcooled boiling," Heat Transfer, Vols. 1?7 (1990) 21?26.

[28] Gilman, L.A., “Development of a General Purpose Subgrid Wall Boiling Model from Improved Physical Understanding for Use in Computational Fluid Dynamics." Thesis. Massachusetts Institute of Technology, 2014.

[29] Rohsenow, W.M, J.P. Hartnett, and Y.I. Cho. Handbook of heat transfer. McGraw-Hill handbooks. McGraw-Hill, 1998.

[30] Kandlikar, Satish G. “A Theoretical Model to Predict Pool Boiling CHF Incorporating Effects of Contact Angle and Orientation." Journal of Heat Transfer 123.6 (2001): 1071.

[31] Polezhaev, Y. V., and Kovalev, S. A., 1990, “Modeling Heat Transfer With Boiling in Porous Structures," Therm. Eng., 37 (12), pp. 617-620.

[32] Ramilison, J. M., P. Sadasivan, and J. H. Lienhard. "Surface Factors Influencing Burnout on Flat Heaters." Journal of Heat Transfer 114.1 (1992): 287.

[33] Berenson, P.J., “Experiments on pool-boiling heat transfer," International Journal of Heat and Mass Transfer, 5 (1962) 985-999.

[34] Liter, S. and M. Kaviany, “Pool-boiling CHF enhancement by modulated porous-layer coating: theory and experiment," International Journal of Heat and Mass Transfer, 44 (2001): 4287-4311.

[35] Sarwar, Mohammad Sohail, Yong Hoon Jeong, and Soon Heung Chang. “Subcooled Flow Boiling CHF Enhancement With Porous Surface Coatings." International Journal Of Heat And Mass Transfer 50 (2007): 3649-3657

[36] Wang, C.H., Dhir V.K. “Effect of Surface Wettability on Active Nucleation Site Density During Pool Boiling of Water on a Vertical Surface." ASME. J. Heat Transfer. 115 (1993): 659-669.

[37] Betz, D., Xu J, Qiu H., and Attinger, D., “Do surfaces with mixed hydrophilic and hydrophobic areas enhance pool boiling?" Applied Physics Letters, 27(141909), 2010.

[38] Chu, Kuang-Han, Ryan Enright, and Evelyn N. Wang. “Structured Surfaces For Enhanced Pool Boiling Heat Transfer." Applied Physics Letters 100.24 (2012): 241603.

[39] Dhillon, Navdeep Singh, Jacopo Buongiorno, and Kripa K Varanasi. “Critical Heat Flux Maxima During Boiling Crisis On Textured Surfaces." Nature Communications 6.(2015): 8247.

[40] Rahman, M.M., E. Ölçero?lu, M. McCarthy “Role of Wickability on the Critical Heat Flux of Structured Superhydrophilic Surfaces." Langmuir (2014) 30 (37): 11225-11234.

[41] Mori, Shoji, Suazlan Mt Aznam, and Kunito Okuyama. “Enhancement Of The Critical Heat Flux In Saturated Pool Boiling Of Water By Nanoparticle-Coating And A Honeycomb Porous Plate." International Journal Of Heat and Mass Transfer 80.(2015): 1-6.

[42] LaFleur, Brandon, Daniel Walter, and Annalisa Manera. "Neutronic Effects of Nickel Ferrite CRUD without Boron Hideout." Transactions of the American Nuclear Society 109 (2013): 1295-298.

[43] Byers, W.A., 2010. "Pressurized Water Reactor Core Crud Mapping." 18th International Conference on Nuclear Engineering (ICONE 18), Xian China.

[44] Electric Power Research Institute (EPRI), 2003. PWR axial offset anomaly (AOA) guidelines, revision 1. Technical, Report 1003213.

[45] Deshon, Jeff, Dennis Hussey, Brian Kendrick, John Mcgurk, Jeff Secker, and Michael Short. "Pressurized Water Reactor Fuel Crud and Corrosion Modeling." Jom 63.8 (2011): 64-72.

[46] Short, M.p., D. Hussey, B.k. Kendrick, T.m. Besmann, C.r. Stanek, and S. Yip. "Multiphysics Modeling of Porous CRUD Deposits in Nuclear Reactors." Journal of Nuclear Materials 443.1-3 (2013): 579-87.

[47] Jakob, M. Heat Transfer, John WIley and Sons, 1949.

[48] Pan, C., Jones, B.G., “Wick Boiling Performance in Porous Deposits with Chimneys," AICHE/ANS National Heat Transfer Conference Symposium on Multiphase and Heat Transfer. 1985.

[49] Macbeth, R.V., “Boiling on surfaces overlayed with a porous deposit: heat transfer rates obtained by capillary action," Atomic Energy Establishment Winfrith AEEW-R-711, 1971.

[50] Cinosi, N., I. Haq, M. Bluck, and S.p. Walker. "The Effective Thermal Conductivity of Crud and Heat Transfer from Crud-coated PWR Fuel." Nuclear Engineering and Design 241.3 (2011): 792-98.

[51] Macbeth, R.V., “An investigation into the effects of ’crud’ deposits on surface temperature, dry-out, and pressure drop with forced convection boiling of water at 69 bar in an annular test section," Atomic Energy Establishment Winfrith AEEW-R-705, 1971.

[52] Cohen, P., “Heat and Mass Transfer for Boiling in Porous Deposits with Chimneys," AICHE Symposium Series, 70, 71-80. 1974.

[53] Henshaw, J., et al. “A Model of Chemistry and Thermal Hydraulics in PWR Fuel Crud Deposits." Journal of Nuclear Materials 353.1-2 (2006): 1-11.

[54] Haq, I., Nicolas Cinosi, Michael Bluck, Geoff Hewitt, and Simon Walker. “Modelling Heat Transfer and Dissolved Species Concentrations within PWR Crud." Nuclear Engineering and Design 241.1 (2011): 155-62.

[55] CRC Handbook of Chemistry and Physics, 95th Ed. 2014-2015

[56] Beck, Michael. “Thermal Conductivity of Metal Oxide Nanofluids," Thesis. Georgia Institute of Technology, 2008.

[57] Keem, J.E, and Honig, J.M., “Selected Electrical and Thermal Properties of Undoped Nickel Oxide". CINDAS Report 52, August 1978.

[58] Leitner, Jindrich et al., “Estimation of Heat Capacities of Solid Mixed Oxides." Thermochimica Acta, 395. 1-2 (2002): 27-46.

[59] Navrotsky, Alexandra. “Nanoscale Effects on Thermodynamics and Phase Equilibria in Oxide Systems." ChemPhysChem, 12.12 (2011):2207-215.

[60] Su, Guanyu. “Experimental Study of Transient Pool Boiling Heat Transfer under Exponential Power Excursion on Plate-Type Heater." Thesis. Massachusetts Institute of Technology, 2015.

[61] Huang, Zhouchun, et al. “Microfabrication Of Cylindrical Microfluidic Channel Networks For Microvascular Research." Biomedical Microdevices 14.5 (2012): 873-883.

[62] Kia Hian, Lau, et al. “Releasing High Aspect Ratio SU-8 Microstructures Using AZ Photoresist As A Sacrificial Layer On Metallized Si Substrates." Microsystem Technologies 19.11 (2013): 1863-1871.

[63] AZ Electronic Materials. “AZ 4000 Series Photoresists for Thick Film Applications." 70 Meister Avenue, Sommerville, NJ 08876.

[64] AZ Electronic Materials. “Photoresist Adhesion and HMDS (hexamethyldisilazane) Processing." 70 Meister Avenue, Sommerville, NJ 08876.

[65] Lee, Daeyeon, Michael F. Rubner, and Robert E. Cohen. "All-Nanoparticle Thin-Film Coatings." Nano Letters, American Chemical Society 6.10 (2006): 2305-2312.

[66] Lee, Daeyeon, et al. "Ph-Dependent Structure And Properties Of Tio2/Sio2 Nanoparticle Multilayer Thin Films." Chemistry Of Materials 19.6 (2007): 1427-1433.

[67] Bravo, J. et al. “Transparent Superhydrophobic Films based on Silica Nanoparticles". Langmuir 2007 23 (13), 7293-7298.

[68] Cebeci, F.C., et al. “Nanoporosity-Driven Superhydrophilicity: A Means to Create Multifunctional Antigoffing Coatings". Langmuir 2006 22, 2856-2862.

[69] Gemici, Z., et al. “Hydrothermal Treatment of Nanoparticle Thin Films for Enhanced Mechanical Durability". Langmuir 2008 24, 2168-2177.

[70] Dektak 150 Surface Profiler User’s Manual. P/N 980-294. Revision B. Veeco Instruments Inc. 2009.